Preliminary Conceptual Design of SIRIUS, A Symmetric Illumination, Direct Drive Laser Fusion Reactor

B. Badger, H.M. Attaya, T.J. Bartel, M.L. Corradini, R.L. Engelstad, G.L. Kulcinski, E.G. Lovell, G.A. Moses, R.R. Peterson, M.E. Sawan, I.N. Sviatoslavsky, L.M. Goldman, L.D. Lund, R.L. McCrory, S. Skupsky, R.E. Hopkins, K. Walsh

March 1984

UWFDM-568

FUSION TECHNOLOGY INSTITUTE

UNIVERSITY OF WISCONSIN

MADISON WISCONSIN

Preliminary Conceptual Design of SIRIUS, A Symmetric Illumination, Direct Drive Laser Fusion Reactor

B. Badger, H.M. Attaya, T.J. Bartel, M.L. Corradini, R.L. Engelstad, G.L. Kulcinski, E.G. Lovell, G.A. Moses, R.R. Peterson, M.E. Sawan, I.N. Sviatoslavsky (University of Wisconsin); L.M. Goldman, L.D. Lund, R.L. McCrory, S. Skupsky (University of Rochester); R.E. Hopkins, K. Walsh (Optizon Corporation)

Fusion Technology Institute
University of Wisconsin
1500 Engineering Drive
Madison, WI 53706

http://fti.neep.wisc.edu

March 1984

UWFDM-568

DOE/DP/40185-1

PRELIMINARY CONCEPTUAL DESIGN OF SIRIUS, A SYMMETRIC ILLUMINATION, DIRECT DRIVE LASER FUSION REACTOR

Final Report for the Period

August 8, 1983 to June 1, 1984

B. Badger, H.A. Attaya, T.J. Bartel, M.L. Corradini,

R.L. Engelstad, G.L. Kulcinski, E.G. Lovell, G.A. Moses,

R.R. Peterson, M.E. Sawan, I.N. Sviatoslavsky

Fusion Engineering Program, Nuclear Engineering Department
University of Wisconsin-Madison, Madison, Wisconsin 53706

and

L.M. Goldman, R.E. Hopkins[1], L.D. Lund, R.L. McCrory, S. Skupsky, K. Walsh[1]

Laboratory for Laser Energetics
University of Rochester, Rochester, New York, 14623

[1]Optizon Corporation, Rochester, New York

March 1984

UWFDM-568

Work Performed under Contracts DE-AS08-83DP40185 (University of Wisconsin)
and DE-AS08-83DP40186 (University of Rochester).

TABLE OF CONTENTS

ABSTRACT

A critical issues study of a symmetric illumination, direct drive laser fusion reactor called SIRIUS has been conducted. In particular, the uniformity requirements for direct drive targets have been assessed and it is shown that respectable gains (more than 60) could be obtained at modest (2 MJ) KrF laser energies. Previous ICF cavity designs have been examined for use in a symmetric illumination geometry and features from several designs have been combined into a dry wall cavity design with a radius of 8 meters. Neutronic and photonic analysis shows that the present SIRIUS cavity design can breed sufficient tritium (breeding ratio = 1.17) even with 32 laser ports penetrating the cavity. However, it was found that there are a few critical issues that remain to be solved before a self-consistent reactor design could be initiated. Radiation damage to final optics, thermal performance of SiC tiles on the SIRIUS cavity wall, and performance of direct drive targets to non-uniformities in the beam are a few of the critical issues identified for future work.

1. INTRODUCTION

The U.S. Department of Energy's (DOE) program plan for the development of inertial fusion has adopted symmetrically-illuminated, direct-drive as a back-up approach for the first-line, indirect-illumination schemes being developed by the National Laboratories. As a natural extension of this program plan, the Nuclear Engineering Department of the University of Wisconsin (UW) and the University of Rochester's Laboratory for Laser Energetics (LLE), have considered a critical-issues study of a symmetrically-illuminated, direct-drive, inertial-fusion reactor, concentrating on those engineering aspects of such a reactor which are unique to this approach and have not attempted a more general point-design study.

Almost all previous inertial confinement reactor studies, using a variety of driver options, have assumed an asymmetric illumination geometry.[1] Only the Los Alamos National Laboratory study of 1972 addressed a symmetric-illumination geometry, but it used a CO_2 laser driver operating at 10.6 microns.[2] A more detailed review of past designs and an assessment of their suitability to uniform illumination is given in Chapter 3. For this study, we assumed a short wavelength laser driver (KrF at 238 nm); recent experiments have shown that short wavelengths will couple more efficiently to a pellet and generate lower pellet preheat from fast electrons.[3] The lack of fast electrons affects the target size and composition and consequently the first wall loading in the reactor.

A critical issue for direct-drive reactors is the number of laser beams and the total solid angle they subtend. Recent work at LLE has shown that a 32-beam system with slow final optics (f/20) occupying only 0.5% of the cavity solid angle could provide illumination uniformity with an rms variation of

less than 1% at the critical surface.[4] This should provide adequate drive uniformity for laser driven inertial fusion.[5] Based on that work, the present study considers a uniform-irradiation 32-beam reactor with f/10 final optics which occupy 2% of the total solid angle. The total solid angle is comparable to the proposed value for indirect-drive targets in previous studies.[6] The effect on uniformity of using a larger number of beams (but keeping beam total solid angle constant) is discussed in Chapter 2. However, the economic and technological implications of increased beam number have not yet been considered for the driver. The reactor design is determined by the flux of particles and radiation emitted from the target. One characterstic of directly driven targets is that they can be composed entirely of low-Z materials. The low-Z composition was considered in determining wall loading and conversion of fusion energy to x-rays. Typically, for direct-drive targets (with a compressed ρR of ~ 2 g/cm^2) the partitioning of energy is about 70% to neutrons, 20% to charged particles and 10% to x-rays. These general characteristics are relatively insensitive to details of the particular target. The target used (Chapter 4.2) was chosen to be consistent with constraints imposed by drive uniformity and hydrodynamic stability, but a complete target design optimization was beyond the scope of this work.

As a first step in designing an ICF reactor with final optics placed uniformly around the fusion chamber, we have identified the key difficulties from a reactor technology point of view, and have proposed a viable concept for a direct-drive reactor configuration. The specific tasks considered for this work are:

1. Evaluate the suitability of previously proposed reactor cavity and blanket designs (e.g., HYLIFE,[7] HIBALL,[8], SOLASE,[9] etc.) to uniform illumination of the target.
2. Propose, if necessary, new cavity/blanket designs that are more suitable for uniform illumination ICF. Identify and propose solutions to mechanical design difficulties of the cavity/blanket system that result from the uniform positioning of final mirrors.
3. Perform simple calculations of fusion energy recovery and tritium breeding from blankets and penetrations consistent with uniform illumination ICF.
4. Review the issue of radiation damage to the final focusing optics for short wavelength optics consistent with the positioning of final mirrors for uniform illumination.

The results of this initial study are reported in the remainder of this document. Chapter 4 gives the details of a new reactor concept that specifically accommodates uniform illumination. Several features of the design have been studied in some detail including: first wall protection; blanket performance; mechanical design; target performance; radiation damage to both the structure and the final optics. Finally, Chapter 5 enumerates the critical issues needing further study before this design can be placed on a comparative basis with the other complete conceptual designs such as HYLIFE. Additional areas such as driver design, balance of plant, and the fuel-pellet factory and pellet costs may be affected by the direct-drive option, but they have not been examined. The general conclusions of this study are made in Chapter 6.

References for Chapter 1

1. M.J. Monsler, J. Hovingh, D.L. Cook, T.G. Frank, G.A. Moses, "An Overview of Inertial Fusion Reactor Design," Nuclear Technology/Fusion 1, 302 (1981).

2. L.A. Booth (compiler), "Central Station Power Generation by Laser Driven Fusion," Los Alamos National Laboratory Publication LA-4858-MS (Feb. 1972).

3. C.E. Max, "Theory of the Coronal Plasma in Laser Fusion Targets," Physics of Laser Fusion 1, UCRL-53107 (Dec. 1981).

4. S. Skupsky, R.L. McCrory, R.S. Craxton, J. Delettrez, R. Epstein, K. Lee, C. Verdon, "Uniformity of Energy Deposition for Laser Drive Fusion," Laser Interaction and Related Plasma Phenomena, H. Hora and G. Miley, Eds., Vol. 6, p. 751 (1984); S. Skupsky and K. Lee, J. Appl. Phys. 54, 3662 (1983).

5. S.E. Bodner, "Critical Elements of High Gain Laser Fusion," J. Fusion Energy 1, 221 (1981).

6. J. Hovingh, "Design Considerations for Direct-Illumination-Driven Inertial Fusion Reactors," 5th Topical Meeting on the Technology of Fusion Energy, Knoxville, TN, UCRL-88215 (April 1983).

7. "Laser Program Annual Report - 1978," Lawrence Livermore Laboratory Report UCRL-50021-78 (March 1978).

8. B. Badger et al., "HIBALL, A Joint Federal Republic of Germany-University of Wisconsin Conceptual Heavy Ion Beam Fusion Reactor Design Study," University of Wisconsin Fusion Engineering Program Report UWFDM-450 (Sept. 1981).

9. R.W. Conn et al., "SOLASE - A Laser Fusion Reactor Study," University of Wisconsin Fusion Engineering Program Report UWFDM-220 (1978).

2. UNIFORMITY STUDIES

2.1 Introduction

Several authors have studied the uniformity produced by overlapping multiple laser beams on a spherical target.[1-4] Skupsky and Lee[5] decomposed the illumination pattern on a sphere in terms of spherical harmonics, to obtain nonuniformity amplitude and wavelength information. The wavelength is important because a short wavelength nonuniformity can be smoothed by thermal conduction within the pellet. Reference 5 (Appendix I) includes a nonuniformity analysis for the existing 24-beam OMEGA facility at the Laboratory for Laser Energetics (LLE), University of Rochester (UR) and a 32-beam, f/20 system. It was shown that the 32-beam system could achieve the required uniformity of less than 1% rms in a limited focal region. Modest thermal smoothing extended the useful region of the 32-beam geometry to include the region of interest for direct-drive laser fusion. This study extends the work in Ref. 5 to include 20, 32, 60 and 96 beams evaluated for 2% and 8% solid angle fractions in the reactor. The coordinates used for these geometries were calculated using a code REPEL and they are included in Appendix II.[6]

2.2 Laser Beam Geometry

The geometry of the laser beams is determined by three related variables which are the laser aperture, the final optic spacing from the pellet and the solid angle fraction the laser beams occupy in the reactor. The laser aperture is a function of the total laser energy and the laser induced damage threshold of the last focusing optic. The final optic spacing from the pellet determines the reaction product loading on the optic and the solid angle fraction has an impact on the performance of the reactor blanket as discussed in Section 4.3. Assuming values for two of these variables dictates the value

of the third parameter. We have chosen to estimate the laser aperture and an acceptable total solid angle, thereby fixing the final optic spacing and the reaction product loading. Section 4.6 discusses the radiation environment of the final optic in the SIRIUS preconceptual design. It should be noted that holding the solid angle fraction constant as the number of beams is varied does not change the spacing of the final optic from the pellet. This allows us to study the illumination uniformity effects of N beams without changing this basic design parameter.

The total aperture of the laser driver is determined by the laser energy and the optical damage threshold of the reflective coating on the last focusing optic. For this study we have used values of 2 MJ for the driver energy and a damage threshold of 5.0 J/cm^2. When the damage threshold value is combined with the assumed geometrical fill factor (0.7) and a safety factor for ripples on the beam (0.5) the overall threshold is 1.75 J/cm^2. This dictates a total laser aperture of 144 m^2. This aperture is independent of the system configuration whether direct or indirect-drive. The corresponding single beam apertures for 20, 32, 60 and 96 beams are given in Table 2.2-1.

The second variable in the system configuration is the solid angle fraction the driver occupies in the reactor. This is related to the number of beams and the f-number of the beams by the following expression:

$$\frac{\Delta\Omega}{4\pi} = \frac{N}{2}\left(1 - \frac{2f}{(4f^2 + 1)^{1/2}}\right) \qquad \text{where: } N \text{ - number of beams, and } f \text{ is the beam f-number.} \qquad (2\text{-}1)$$

For the SIRIUS study we are evaluating 2% and 8% solid angle fractions for the laser beams and the appropriate f-numbers for each of the beam configurations have been calculated using Eq. (2-1), and are given in Table 2.2-1.

SIRIUS PARAMETERS

UR LLE

NUMBER OF BEAMS	20	32	60	96
Beam Aperature (m)	2.7	2.1	1.6	1.2
f-Number for 2% Solid Angle Fraction	7.9	10.0	13.7	17.3
f-Number for 8% Solid Angle Fraction	3.9	5.0	6.8	8.6

Table 2.2-1

- Final optic spacing from pellet

  2% solid angle fraction - 21.3 m
  8% solid angle fraction - 10.6 m

A105

This f-number and the individual beam aperture give the spacing of the final optic from the pellet. The 2% solid angle fraction places the final optic 21.3 m from the pellet and the 8% solid angle fraction has a 10.6 m spacing. This approach allows an evaluation of the effect of dividing the total laser aperture into N beams while maintaining a constant solid angle fraction in the reactor. The cost scaling of the driver with N is beyond the scope of this work. This report attempts to elucidate uniformity scaling with N, so that future work can balance the cost scaling of a driver against the uniformity scaling with N.

2.3 Formalism

The formalism used in this work has been described in Appendix I, but it is reviewed here. The irradiation pattern on the sphere is decomposed into spherical harmonics where the standard deviation of a Legendre-mode amplitude is given by:

$$\sigma_\ell = \left|\frac{E_\ell}{E_0}\right| \left[(2\ell + 1) \sum_{kk'} P\ell(\hat{\Omega}_k \cdot \hat{\Omega}_{k'}) \frac{W_k W_{k'}}{W_T^2}\right] . \qquad (2\text{-}2)$$

The single beam factor $|E_\ell/E_0|$ is determined by the focus position, f-number, beam profile and assumed target conditions. This single beam factor is evaluated by tracing rays through the pellet plasma shown in Fig. 2.3-1. (Calculations were also performed using longer plasma scale lengths more characteristic of the SIRIUS target and little difference was found in the nonuniformity of irradiation. The general features of nonuniformity are predominately determined by the geometrical disposition of the laser beams and are relatively insensitive to the plasma profile.) As discussed in Appendix I, the energy absorbed beyond 1/3 critical density is not used in the calculation of uni-

TARGET CONDITIONS FOR SINGLE-BEAM FACTOR CALCULATIONS

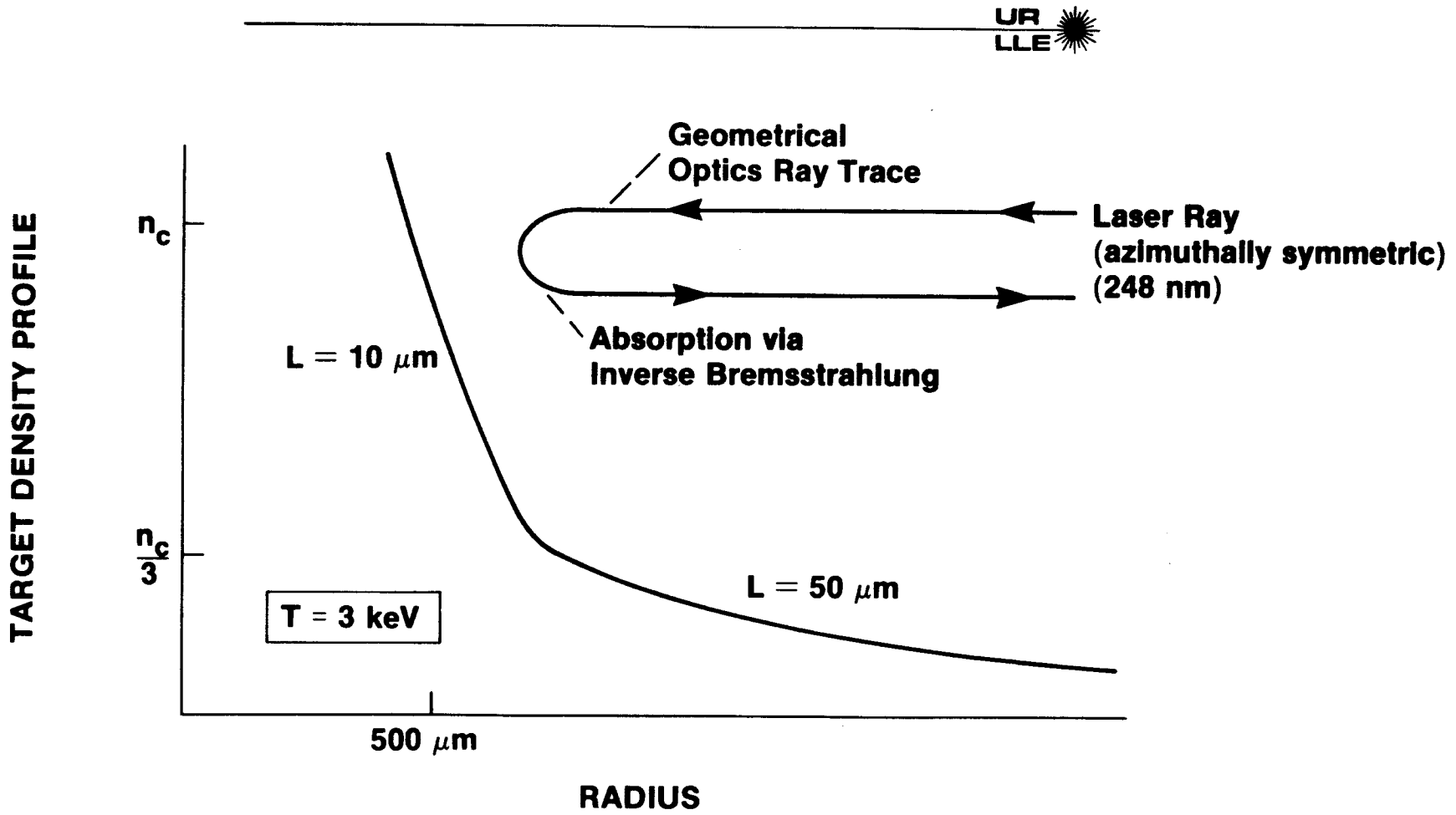

A116

Figure 2.3-1

formity as it probably is not important for driving the target; including it would only decrease the estimated nonuniformity. The second factor on the right hand side of Eq. (2-2) is the geometrical factor which is determined by the number and orientation of the beams ($\hat{\Omega}_k$) and the beam energies (W_k). The sum is over all beams, $W_T = \Sigma W_k$, and P_ℓ is a Legendre polynomial. The rms standard deviation of all modes is defined as:

$$\sigma_{rms} = \left(\sum_{\ell \neq 0} \sigma_\ell^2 \right)^{1/2} . \tag{2-3}$$

2.4 Uniformity Calculations

We have calculated the nonuniformity, in terms of σ_{rms}, for a variety of conditions. Our early work, Appendix I, indicated a quadratic beam intensity profile of the following form produced adequate uniformity:

$$I = I_0 \left(1 - \frac{r^2}{r_0^2}\right) \tag{2-4}$$

where r_0 is the radius of the pellet. See Appendix III for the relationship of r_0 to the aperture ($2R_0$) which defines the f-number of the system. This profile has been used in the following calculations. See Section 2.5 for comparisons of the uniformity achieved with a quadratic profile to the uniformity achieved with other beam profiles.

The σ_{rms} for a 2% solid angle fraction geometry is plotted in Fig. 2.4-1 for 20, 32, 60 and 96 beams as a function of a focus ratio. The focus ratio is defined as:

$$\text{focus ratio} = \frac{F}{2fr_0} . \tag{2-5}$$

Fig. 2.4-1

NONUNIFORMITY OF LASER ENERGY DEPOSITION FOR 2% SOLID ANGLE FRACTION

UR LLE

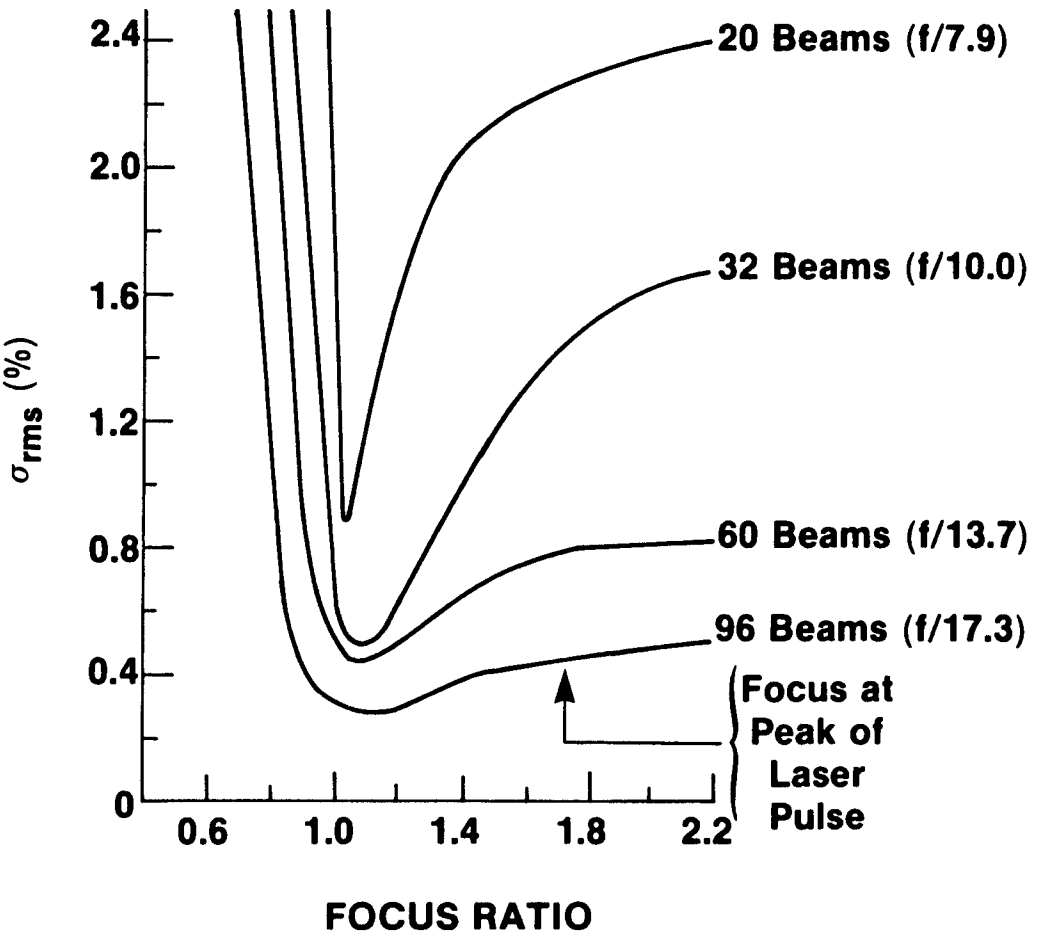

A97

F is the position (in mm) of the geometrical best focus beyond the pellet center, r_o is the pellet radius (in mm) and f is the beam f-number. A focus ratio of 1 corresponds to tangential focus where the beam aperture ($2R_o$) illuminates a hemisphere of the pellet ($2r_o$).

The maximum tolerable nonuniformity is generally assumed to be around 1% rms, which would provide a variation in implosion velocity of 3-4%.[5,7] (The results in Fig. 2.4-1 do not include any effects of thermal smoothing.) An important conclusion drawn from Fig. 2.4-1 is that 60 and 96-beam systems maintain nonuniformity below the 1% rms level for a large focal region. Calculations indicate the target is generally driven to 60% of the original diameter where the peak of the laser pulse is incident on the target. If the implosion starts at tangential focus (focus ratio = 1) then the peak of the laser pulse will be at a focus ratio of 1.67 as shown in Fig. 2.4-1. Further experimental understanding of thermal smoothing may allow fewer beams to maintain this low nonuniformity over the required focal region. This is illustrated in Fig. 2.4-2 (from Appendix I). The σ_{rms} for a 32 beam system at f/20 is shown. The dotted curve represents the attenuation of nonuniformities due to thermal smoothing. This calculation assumes the ratio of spacing from critical density to ablation surface (ΔR) to pellet radius (R) is 0.1.

As the solid angle fraction is increased the uniformity improves as shown in Fig. 2.4-3. As the number of beams is increased the change in uniformity with solid angle fraction decreases to a negligible amount for 96 beams.

To see more clearly the effects of numbers of beams and solid angle fractions on the uniformity we defined an average σ_{rms} in the focus ratio interval from 1.0 to 2.0. This is plotted in Fig. 2.4-4. These calculations

Fig. 2.4-2

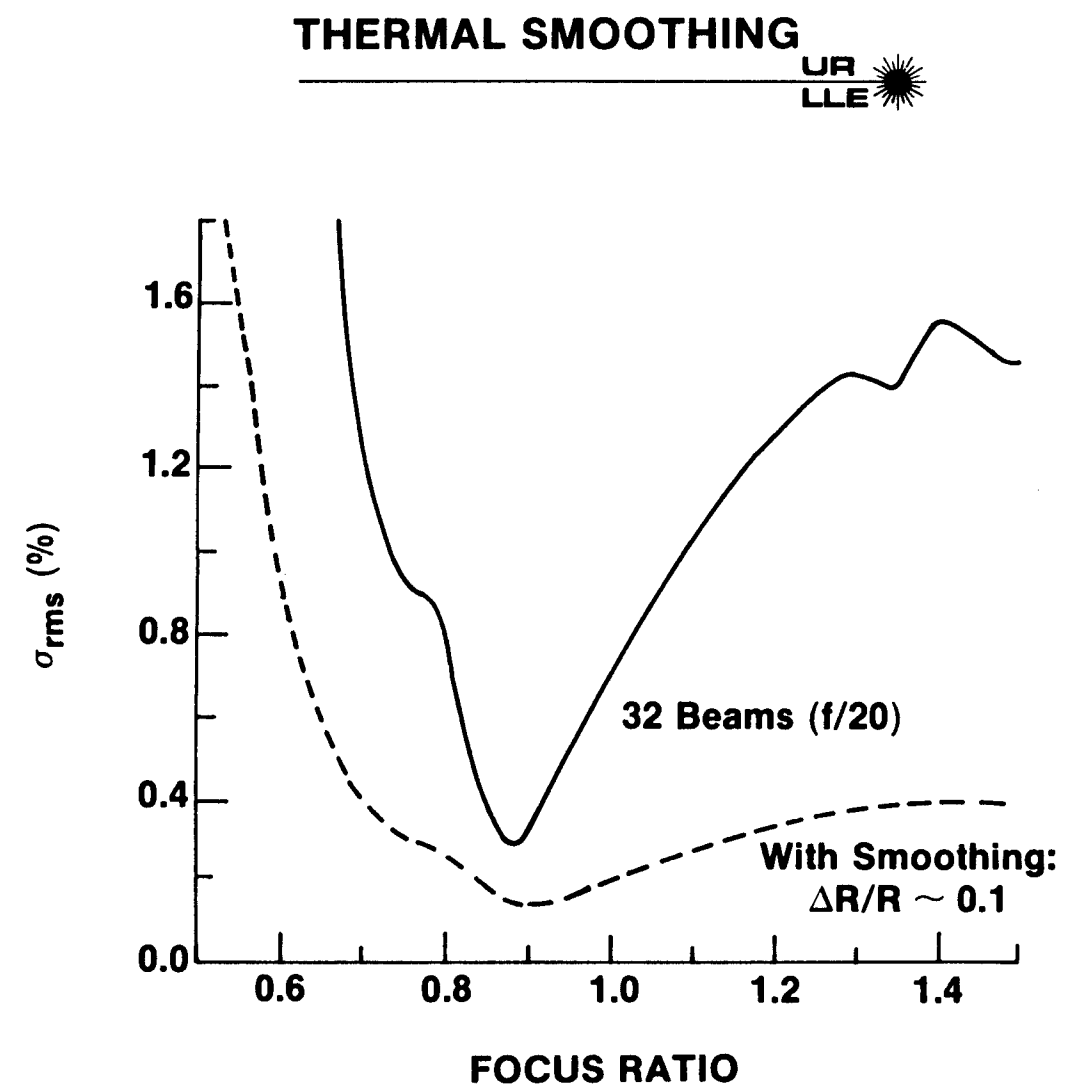
THERMAL SMOOTHING
UR
LLE
1.6
1.2
0.8
0.4
0.0
σ_{rms} (%)
32 Beams (f/20)
With Smoothing:
ΔR/R ~ 0.1
0.6
0.8
1.0
1.2
1.4
FOCUS RATIO

A96

Fig. 2.4-3

UNIFORMITY FOR INCREASED SOLID ANGLE FRACTION

UR LLE

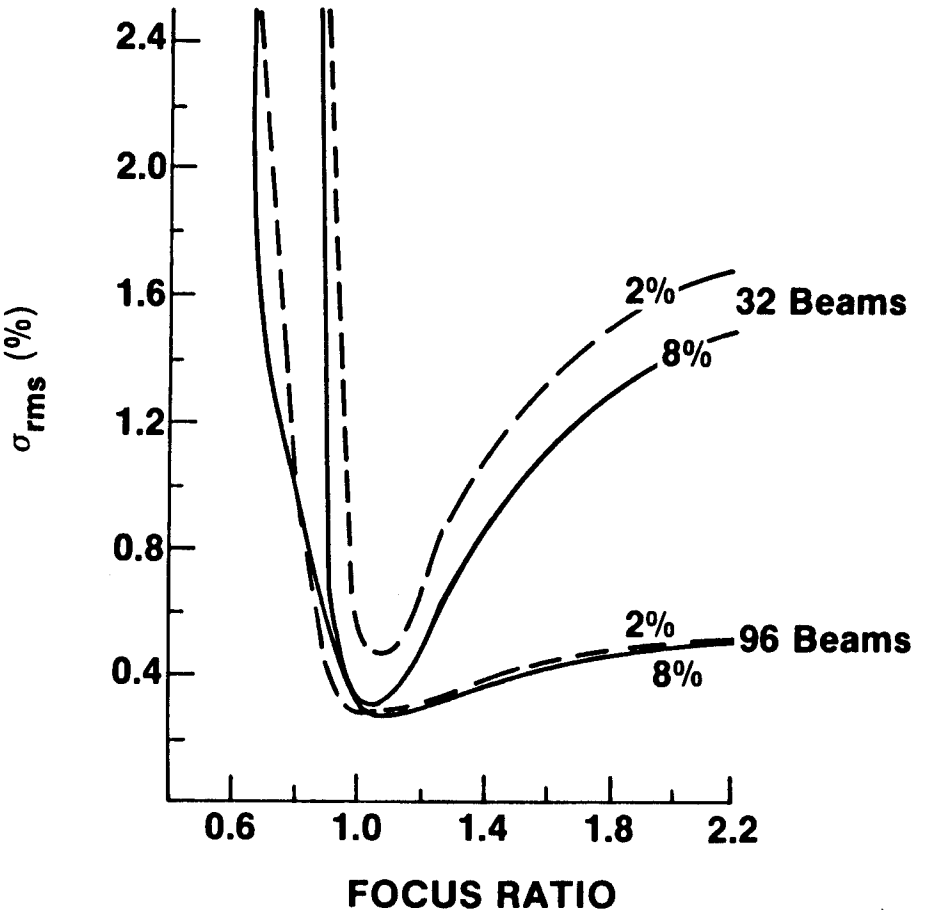

A100

Fig. 2.4-4

AVERAGE NONUNIFORMITY VARIES WITH THE NUMBER OF BEAMS

UR LLE

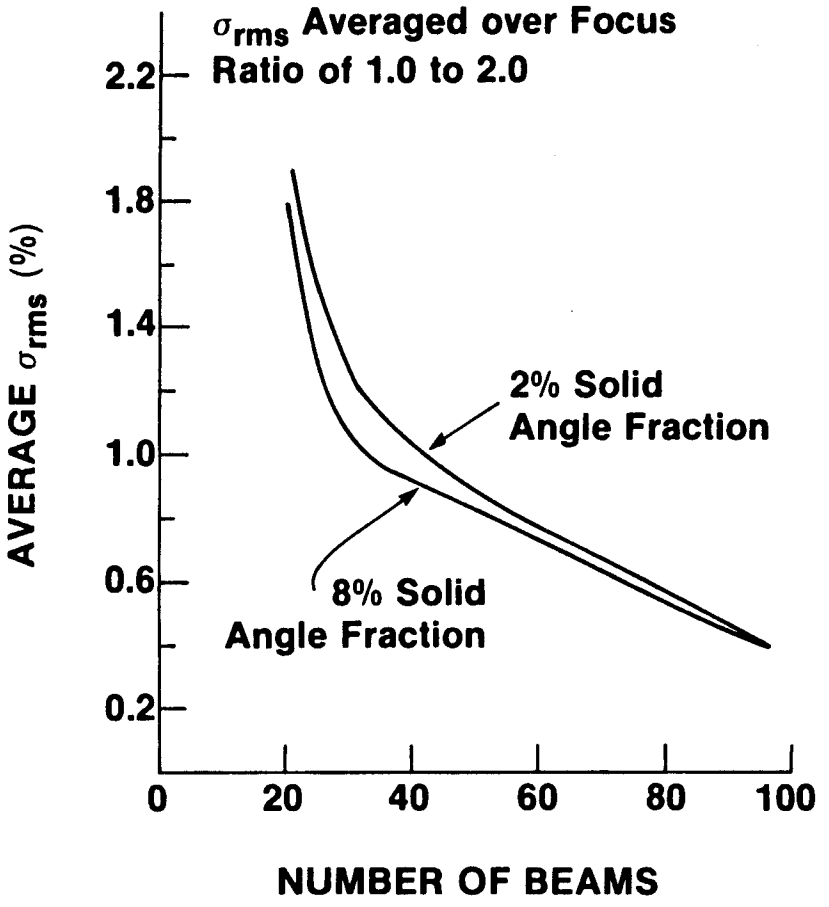

A99

do not use thermal smoothing. In general, the solid angle fraction does not affect uniformity when the individual beam f/number is greater than 10.

The amplitudes of low order modes are strongly affected by the energy balance between beams. This effect is shown in Fig. 2.4-5, where the effect of 2.8% rms variation (random imbalance up to 5%) for the 60 and 96 beam geometries is shown. This beam imbalance is close to the current ±5% on the 24 beams of the OMEGA system.

Realistic radial beam profiles might not be as smooth as the quadratic form used here due to, for example, diffraction effects. The effect of small-scale variations on the radial beam shape has been examined using a modulated quadratic profile of the form:

$$I = I_o \{(1 - \frac{r^2}{r_o^2})\}\{1 + \varepsilon \cos(\pi M r/r_o)\} \qquad (6)$$

where ε and M are parameters controlling the magnitude and wavelength of the modulations. Physically, M/2 corresponds to the number of diffraction rings. For the 32-beam system at a focus ratio of 0.9 (which is near the optimum in Fig. 2.4-2), Fig. 2.4-6 shows σ_{rms} as a function of M for ε = 0.1 (i.e., $\Delta I/I$ = 20%). Note the resonance effect when the profile modulations enhance the normal modes of nonuniformity from the overlapping beams. The dominant mode of nonuniformity is indicated on the graph. (Part of the drop in nonuniformity for large M occurs because only the first 40 modes are included in σ_{rms}.) Beams with more than ~ 4 rings (M > 8) create relatively short wavelength nonuniformities, ℓ > 20, which can be smoothed over small separation distances between the critical and ablation surfaces. To demonstrate the effect of only a small amount of smoothing, we multiply each σ_ℓ by the factor $\exp(-\ell/20)$,

Fig. 2.4-5

UNIFORMITY WITH ENERGY IMBALANCE

UR LLE

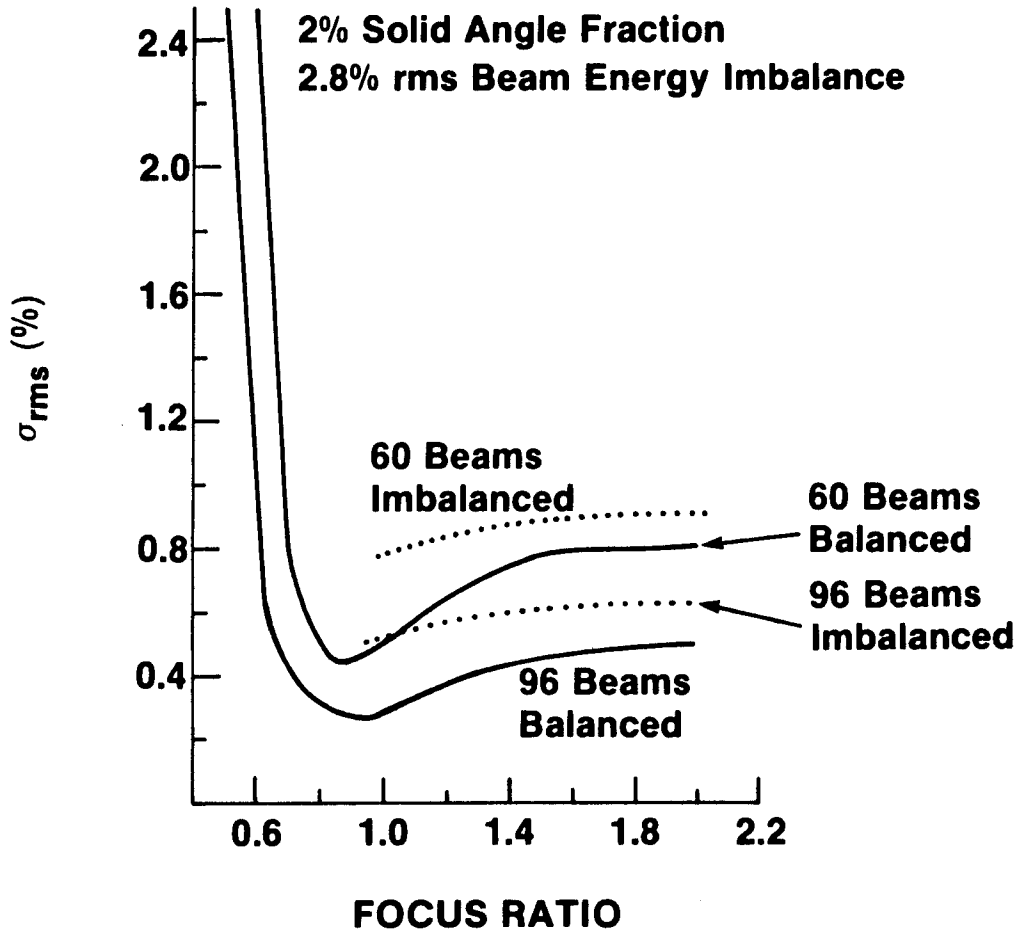

A101

Fig. 2.4-6

NONUNIFORMITY WITH INTENSITY MODULATION

UR LLE

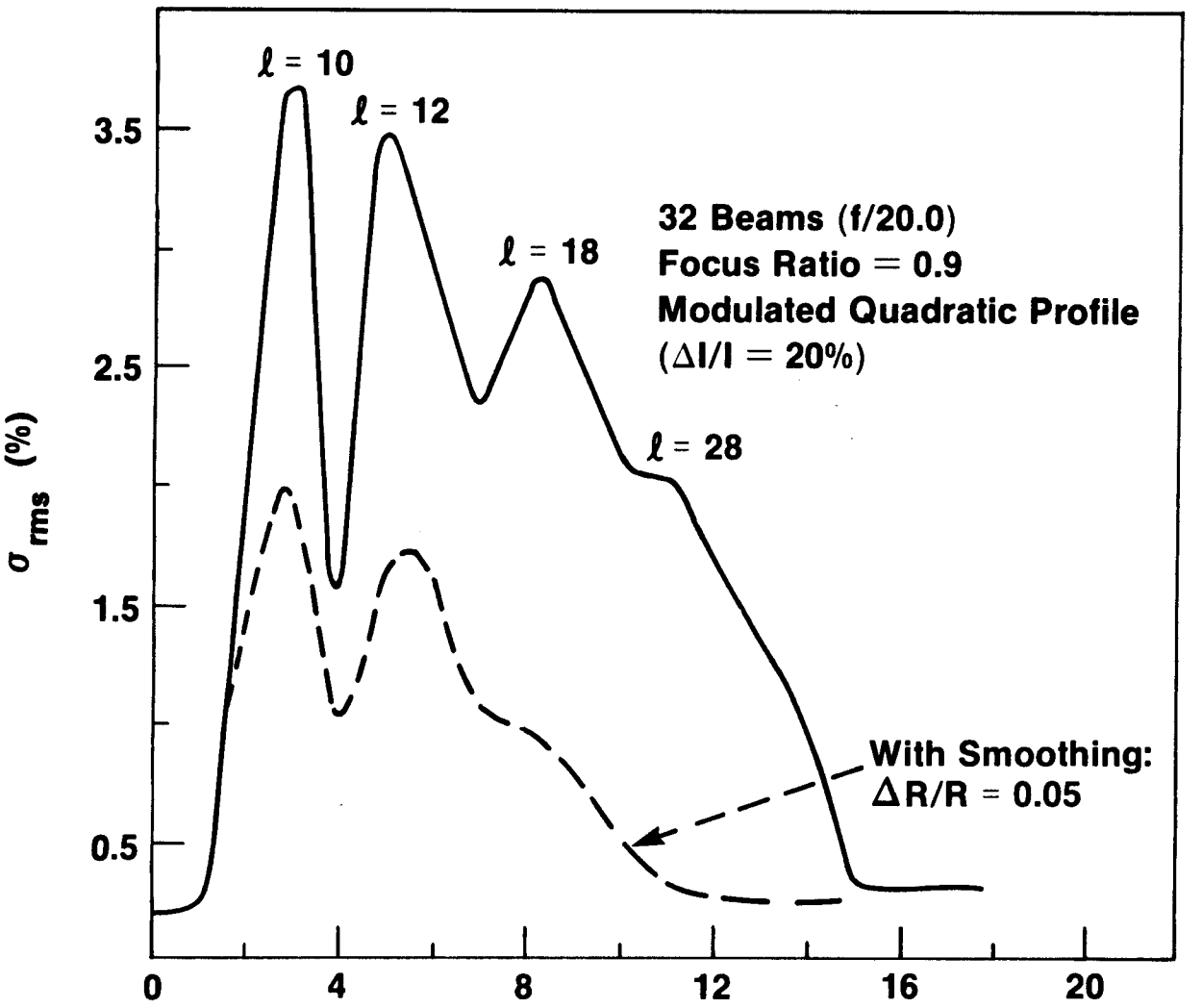

TC1408

60-BEAM MODULATED PROFILE

UR LLE

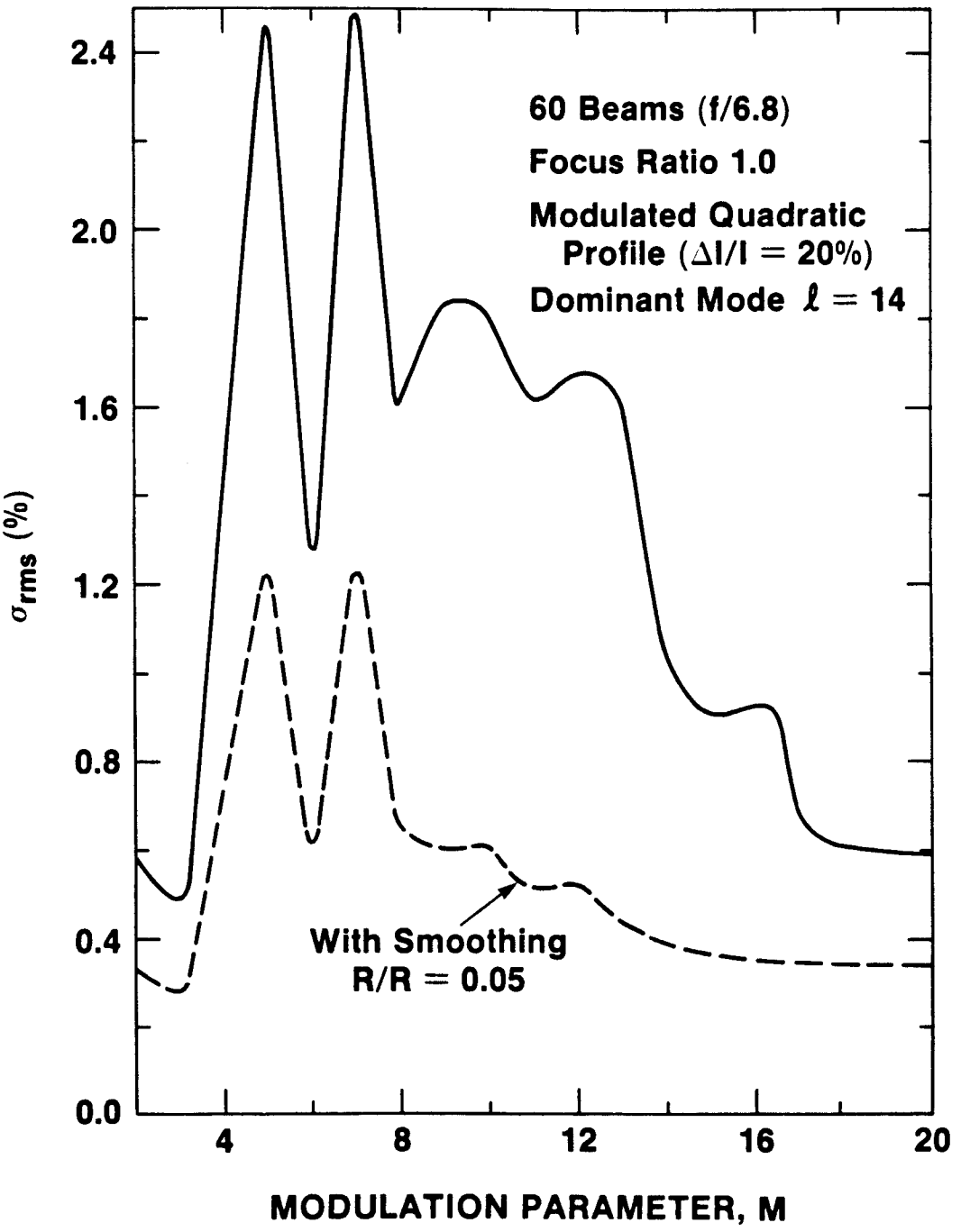

A106

Figure 2.4-7

96-BEAM MODULATED PROFILE

UR
LLE

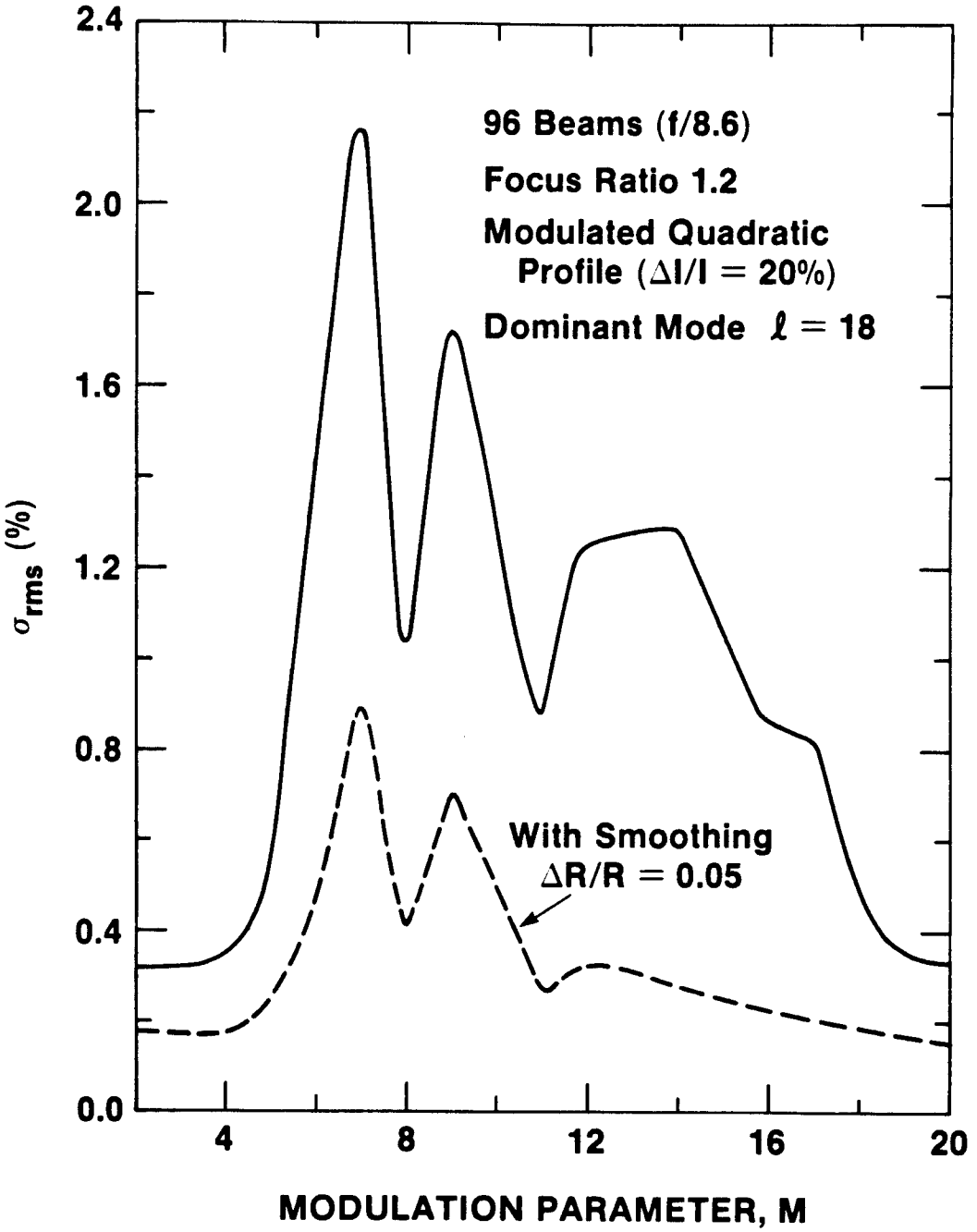

A107

Figure 2.4-8

corresponding to $\Delta R/R = 0.05$. Note the rapid drop in nonuniformity in Fig. 8, for $M > 8$. Additional simulations have shown the magnitude of the nonuniformities scale linearly with ε. Figures 2.4-7 and 2.4-8 are similar calculations for 60 and 96 beams with a 2% solid angle fraction. These results suggest that laser systems for future fusion reactors should be designed with not less than ~ 4 diffraction rings and/or an intensity variation $\Delta I/I$ considerably less than the 20% used here, both of which are within the limits of present-day technology. In addition, the effect of the intensity modulation is greatly reduced as the number of beams is increased to 96.

2.5 Single Beam Profile

The calculations in Section 2.4 used an idealized beam profile, the quadratic, because it provided better uniformity than other profiles. A flat-top profile has also been considered (it yields less uniformity than the quadratic) because it is a useful shape for relating various beam profiles in terms of laser driver efficiency. If a parameter, the fill factor, is defined as the ratio of the energy in an arbitrary beam profile to the energy in a flat-top profile over the same aperture then the laser efficiency is directly proportional to the fill factor of a beam profile. The flat-top has a unity fill factor, thus it serves as a measure of the uniformity achievable with the most efficient laser output. The ideal focusing system would take a flat-top input and generate a quadratic profile at the target. The effort to design this ideal focusing system is discussed below.

We routinely measure the intensity distribution of LLE lasers at the plane of the target. These photographs are referred to as equivalent target plane (ETP) photos. Generally these are digitized and an azimuthally averaged plot is generated. One such plot is shown in Fig. 2.5-1. This profile was

CURRENT BEAM PROFILE FROM LLE LASER SYSTEM

UR LLE

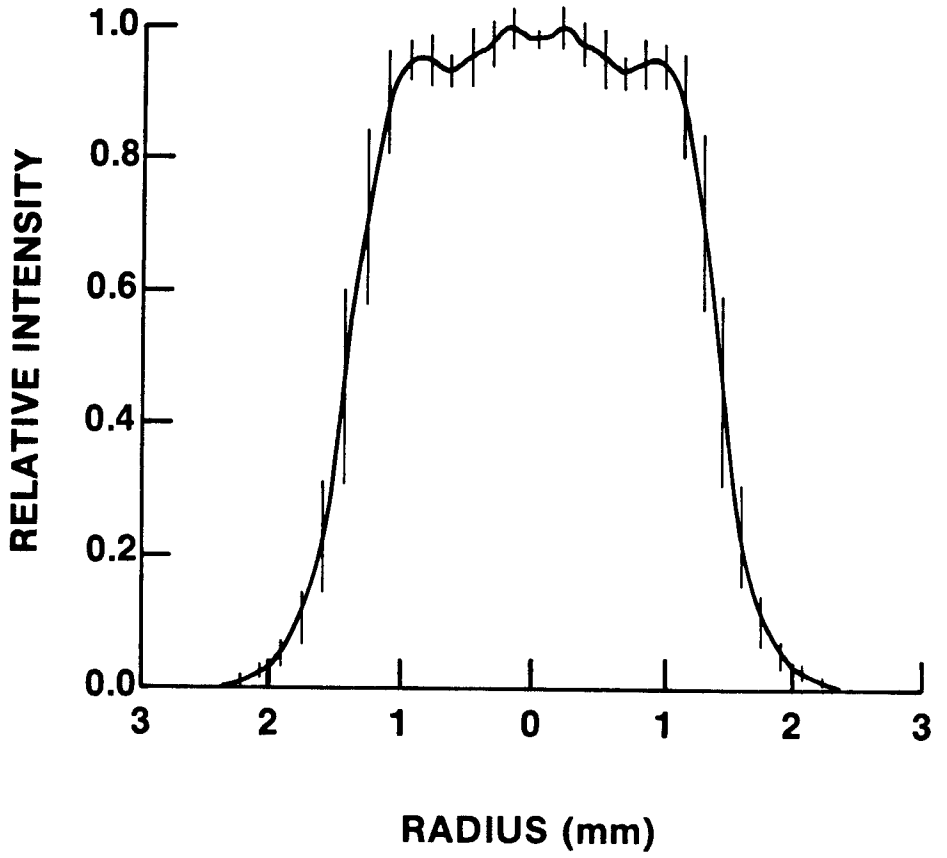

TC1409

Figure 2.5-1

compared with the quadratic and flat-top profiles for the LLE OMEGA system (f/4.0) as shown in Fig. 2.5-2 (from Appendix I). This current profile approaches both idealized profiles if the focus ratio is around 2.0. This implies that the central portion of all three profiles are similar. When these profiles are compared for a 96 beam geometry (Fig. 2.5-3) the same feature is evident at a focus ratio of 2. The difference between the profiles is smaller with the increase to 96 beams.

This improvement in uniformity of illumination with a quadratic profile prompted an effort to design an ideal focusing system for SIRIUS. The input profile was assumed to be a flat-top and the focusing optics were optimized toward generating a quadratic profile at the target as shown in Fig. 2.5-4. Diffraction was ignored because the order of magnitude of diffraction effects is 6 microns for a f/10.0 system at 248 nm, which is small compared with the several millimeter dimension of the target. The desired modification of the intensity profile in the image cannot be achieved by defocusing a perfect lens. A lens which satisfied the Abbe Sine Condition when focusing collimated light has an effective refracting surface which is a sphere centered on the image.[8] The effective refracting surface is the locus of the intersections of the incident rays extended forward, with the exiting rays extended backward. The significance of this condition is that the near field intensity distribution will be reproduced, in reduced size, in any plane perpendicular to the optic axis.

The initial configuration evaluated was a two element system as shown in Fig. 2.5-4, where the first element was a plane mirror and the second element was a sphere. Both elements were tilted at 45° to the beam. In addition, two configurations using three elements were evaluated. The geometry of these

UNIFORMITY DEPENDS ON LASER BEAM PROFILE

UR LLE

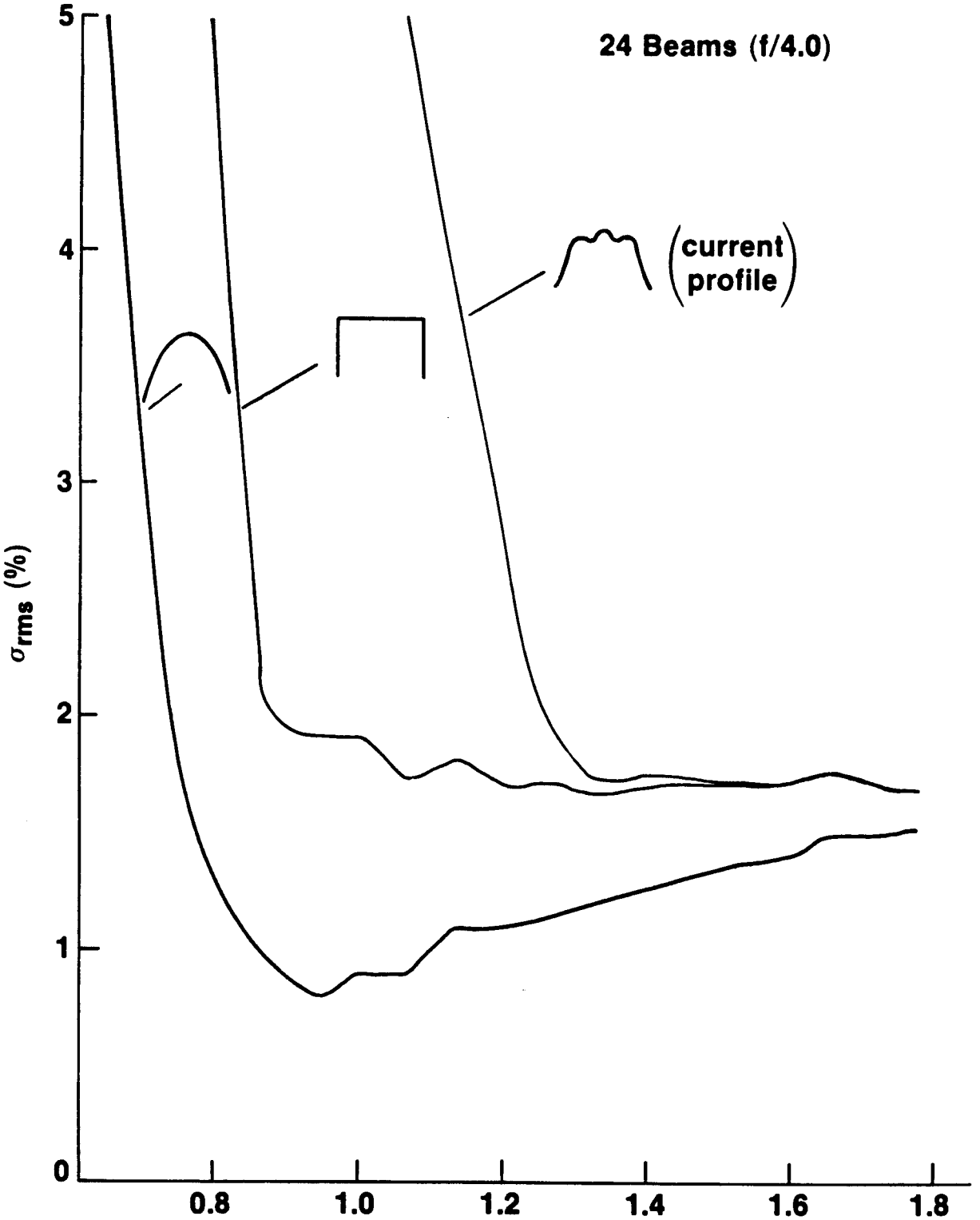

A93

Figure 2.5-2

Fig. 2.5-3

UNIFORMITY DEPENDS ON LASER BEAM PROFILE

UR LLE

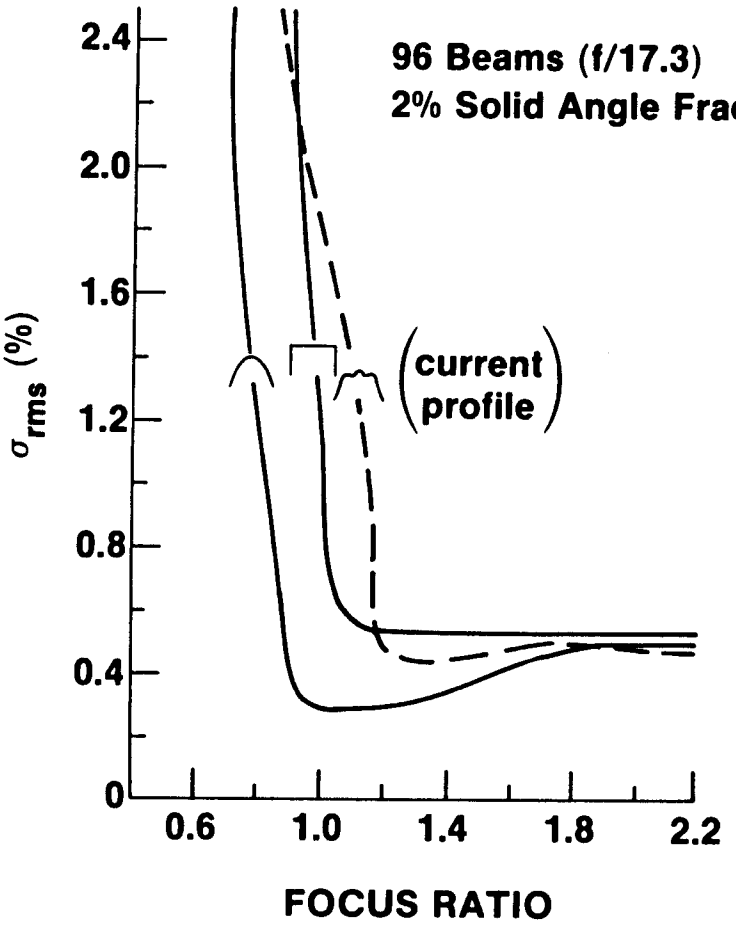

A98

Fig. 2.5-4

SIRIUS FOCUSING GEOMETRY

UR
LLE

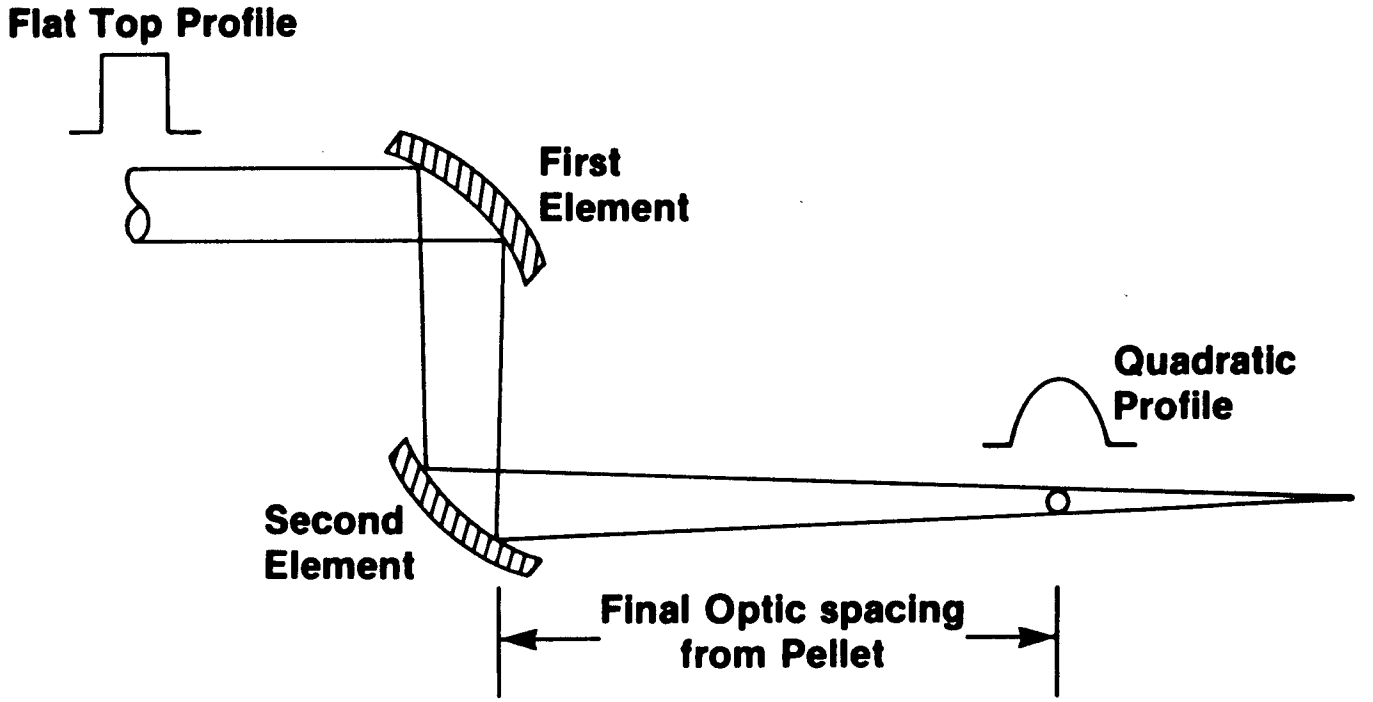

- Final focusing is a two element 90° off axis reflective optic

A104

systems is given in Fig. 2.5-5 where the first two elements were plano mirrors and the third element was either a sphere or off-axis parabola. The plano mirrors and the sphere were tilted at 45° to the beam and all the elements were in a plane.

Optimization was done using the COOL/GENII[9] lens design program with a ray based merit function (see Appendix III). Twenty rays were traced in half the entrance aperture because the symmetry of the problem was such that it was not necessary to trace any rays through the other half of the entrance aperture. The variables were the curvatures and aspheric coefficients, to 10th order, in both the meridional and saggital planes of all mirrors whose initial form was plano or spherical, the separations between the mirrors and the distance from the last mirror to the focal plane. During optimization, plane mirrors and the tilted sphere were allowed to become toroids which were aspheric in both meridians but the parabola was not allowed to vary in shape. The strategy was to use the first elements to redistribute the intensity on the final focusing surface, in such a way that the desired intensity distribution on the image plane was satisfied. The elements were allowed to become doubly aspheric toroids in order to combat the asymmetry effects due to the tilted elements.

The normalized target plane intensity profiles for the three configurations are shown in Fig. 2.5-6. The curves are the results of azimuthally averaging the ray-trace results over the hemisphere. These results were sufficiently remote from the desired quadratic, that further optimization was not attempted. Clearly, the design of the ideal focusing system for SIRIUS is difficult to achieve. Further uniformity analysis of realistic beam profiles

Fig. 2.5-5

THREE ELEMENT FINAL FOCUSING OPTICS FOR SIRIUS

UR LLE

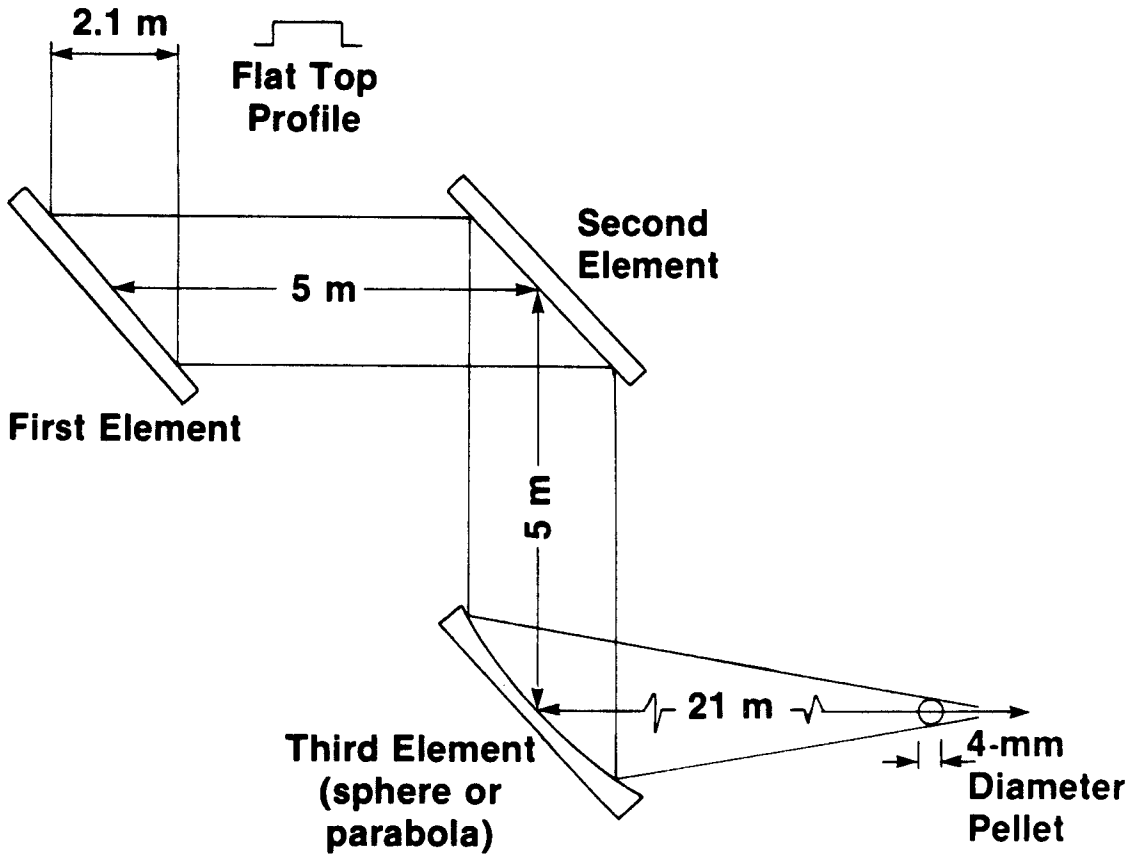

A115

Fig. 2.5-6

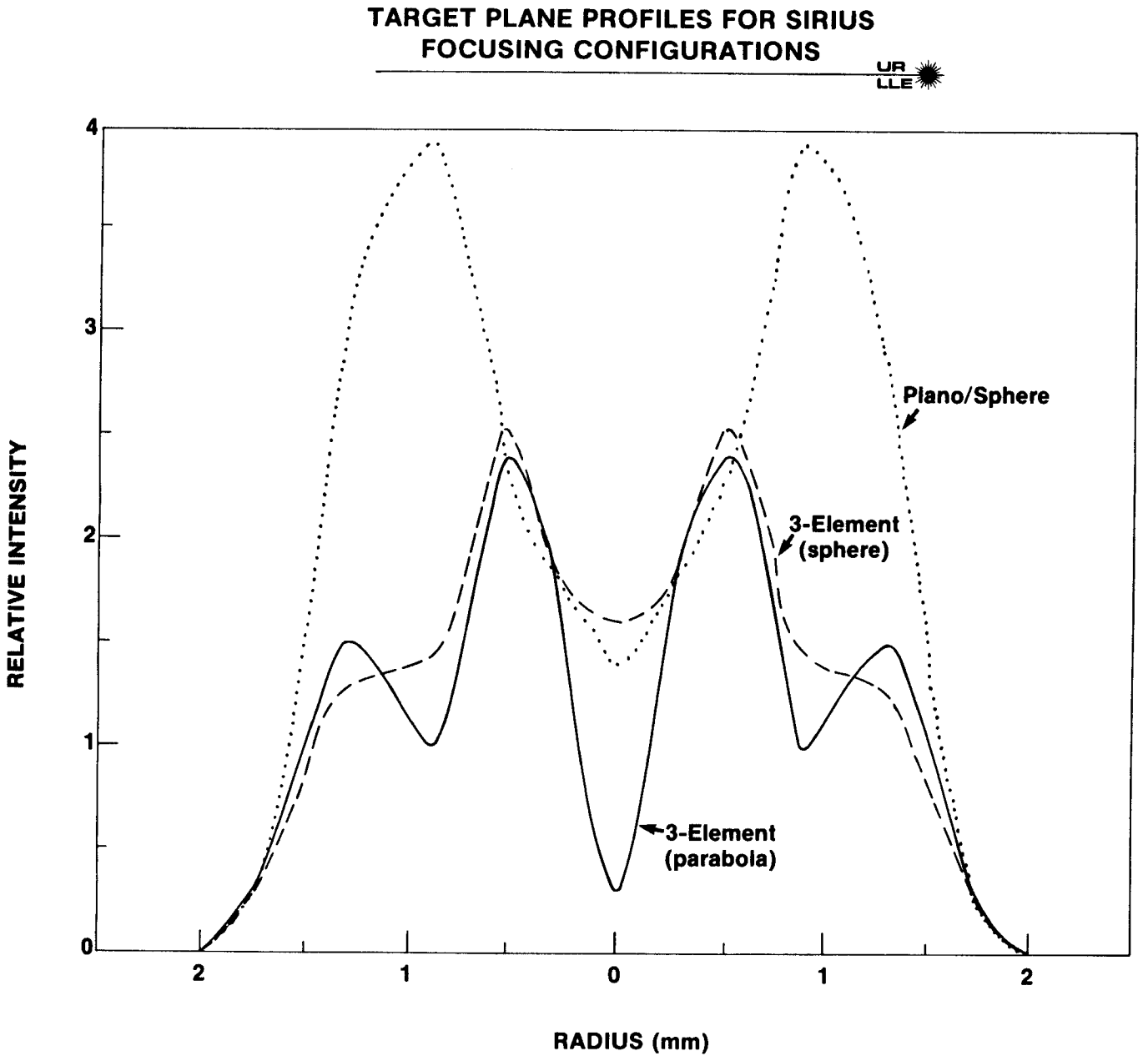
TARGET PLANE PROFILES FOR SIRIUS
FOCUSING CONFIGURATIONS
UR
LLE
RELATIVE INTENSITY
4
3
2
1
0
2
1
0
1
2
RADIUS (mm)
Plano/Sphere
3-Element
(sphere)
3-Element
(parabola)
A114

is required to set tolerances on the acceptable target plane profile. These tolerances are required before further optimization should be pursued.

This optimization proved difficult, at least in part, because of the tilted curved surfaces. Surfaces such as these introduce asymmetries into the image which are hard to remove even with toroidal surfaces.

2.6 Conclusions

The extension of the spherical harmonic analysis of symmetric illumination to 96 beams has shown that the sensitivity of the pellet illumination uniformity to various perturbations such as energy imbalance, intensity modulation or beam profile is greatly diminished when a large number of beams are used. If thermal smoothing is found to be an effective mechanism for reducing nonuniformities, then fewer beams, around 32, could provide adequate illumination uniformity. Analysis of the final focusing optics has shown the ideal case to be difficult to achieve. Further efforts to improve the final focusing geometry should wait for more detailed analysis of the effectiveness of various realistic beam profiles.

References for Chapter 2

1. J.E. Howard, "Uniformity of Illumination of Spherical Laser Fusion Targets," Appl. Optics 16, 2764 (Oct. 1977).

2. J.B. Trenholme, "Target Illumination of Shiva," Laser Program Annual Report - 1974, LLNL Report UCRL-50021-74, Livermore, CA.

3. J.B. Trenholme and E.J. Goodwin, "Theory and Design Analysis," Laser Program Annual Report - 1979, LLNL Report UCRL-50021-79, Livermore, CA, 2-139 (1980).

4. J.B. Trenholme, "Nova Target Illumination Studies," Laser Program Annual Report - 1980, LLNL Report UCRL-50021-80, Livermore, CA, 2-189 (1981).

5. S. Skupsky, K. Lee, "Uniformity of Energy Deposition for Laser Driven Fusion," J. Appl. Phys. 57, 7 (July 1983).

6. R.S. Craxton, private communication.

7. S.E. Bodner, "Critical Elements of High Gain Laser Fusion," J. Fusion Energy 1, 221, Plenum Press, New York (July 1981).

8. R. Kingslake, Lens Design Fundamentals, Academic Press, 1978.

9. Copyright by Genesee Computer Center Inc., Rochester, New York.

3. APPLICABILITY OF PAST REACTOR DESIGNS TO UNIFORM ILLUMINATION LASER FUSION

In the past ten years there have been many inertial confinement fusion (ICF) reactor design studies with different schemes of first wall protection. Almost all of the designs assumed non-uniform target illumination, thus exercising a certain amount of freedom in the placement of beam ports, be they laser beam or ion beam. The presumption is, of course, that classified targets may someday become available for use in ICF reactors. To this day, however, no unclassified target design appearing in the literature will tolerate non-uniform illumination. In this chapter an attempt will be made to identify wall protection schemes which appear to be compatible with uniform illumination.

The design of an ICF reactor cavity must address many issues, some of which are listed below:

(1) Instantaneous high surface wall heating coming from x-ray and ion deposition.

(2) Cyclic fatigue due to repetitive shock and thermal loading.

(3) Neutron and γ heating and the radiation damage in the structure attendant with them, requiring periodic replacement.

(4) Tritium breeding and energy multiplication.

Although all four of the above issues are generic to all fusion systems to various degrees, the first two are dominant in the design of ICF reaction chambers. Several schemes have been proposed to mitigate the problem of instantaneous high surface energy deposition and consequent thermal cyclic fatigue. Among them are liquid metal wetted surfaces, free falling liquid metal jets, buffer gasses, magnetic protection and finally, large cavities,

where the primary mitigating factor is simply $\frac{1}{R^2}$. In the following sections we will discuss each of these schemes separately.

Liquid Metal Protection

Most people lump liquid metal protection into one category. However, there is a difference between wetted surfaces and liquid metal jets. A wetted surface protects against an instantaneous large energy deposition by simply evaporating the fluid and then recondensing it over a longer time scale. It provides no protection for structure against radiation damage, neither does it reduce the effects of a shock wave if the wetted surface is rigidly fixed. On the other hand, liquid metal jets, if they are substantial, can provide some protection against radiation damage to structures simply by absorbing much of the neutron energy. The shock on metallic structures is much reduced by having a space between them and the liquid metal jets. A large fraction of the shock energy is dissipated in the dissassembly of the jets due to rapid volumetric neutron heating following a shot.

There are two major disadvantages of free falling liquid metal jets. Because the liquid metal goes through the cavity very rapidly it does not gain adequate energy in a single pass to be used in a power cycle. Thus it has to be recycled several times before going to a steam generator and consequently uses a lot of pumping power. The second disadvantage has to do with repetition rate. Following each shot the disassembled jets, which are now in the form of a mist, must settle out of the chamber and new jets must be reestablished. For a cavity of 4-5 m radius, this limits the rep-rate to about 1 Hz. The HYLIFE[1] reactor design shown in Fig. 3.1 is an example of the free fall jet scheme.

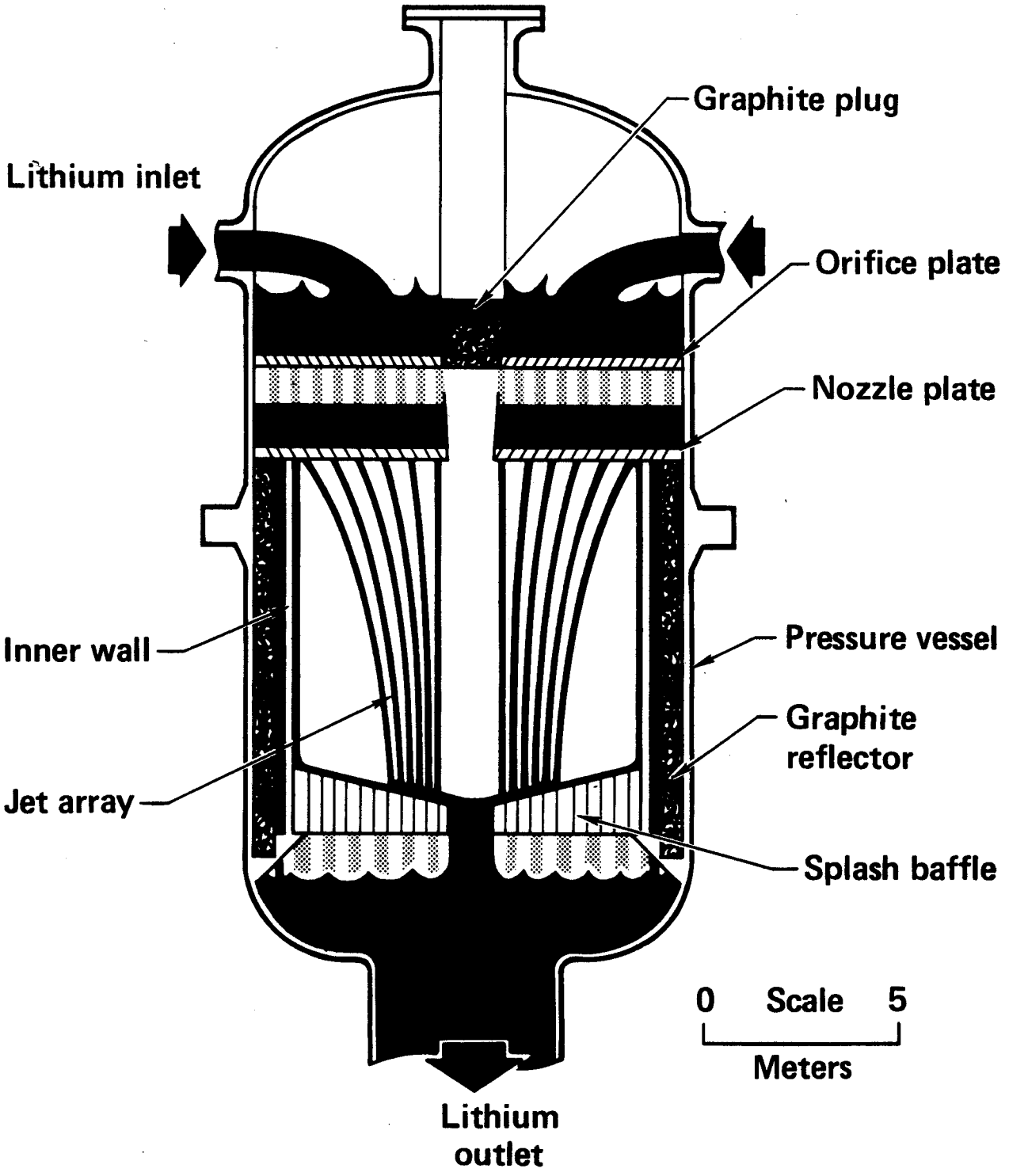

Fig. 3.1. HYLIFE Chamber.

A typical wetted wall design is shown in Fig. 3.2. In this scheme proposed by LANL[2] in 1972, a porous metallic first wall continuously wets the inner surface of the wall with liquid lithium. This layer protects the wall from surface heat by x-rays and target debris, but not from the neutrons. Thus the question of first wall replacement must be faced.

A combination of the wetted wall and free falling jet schemes was used in HIBALL,[3] a heavy ion beam conceptual design completed in 1982 by UW in conjunction with KfK and other groups in the Federal Republic of Germany. In HIBALL, shown in Fig. 3.3, the liquid metal ($Li_{17}Pb_{83}$) jets do not have free surfaces but are encased in porous flexible SiC tubes that are wetted on the outside by seepage of the flowing coolant, as shown in Fig. 3.4. These tubes are called INPORT units for "inhibited flow porous tubes." A sufficient number of INPORT units are placed between the target and the first structural wall, thus extending its survival to the full reactor lifetime. The wetted surface absorbs the surface heat and then recondenses the vapors over a longer time scale, while the flexible tubes absorb the shock without transmitting it to the wall. Further, because mass density of $Li_{17}Pb_{83}$ is higher than that of Li and because the jets are encased in the tubes, they do not disassemble as in the case of free falling jets, allowing rep-rates perhaps as high as 5 Hz. Finally, the transit time of the liquid metal through the reactor is slowed down sufficiently through the INPORT units to allow the heated fluid to be used directly in a power cycle. Obviously, all these advantages do not come free. The SiC tubes suffer radiation damage and must be changed out periodically. Because they are flexible, the changeout of the INPORT units would seem to be easier that other similar metallic components.

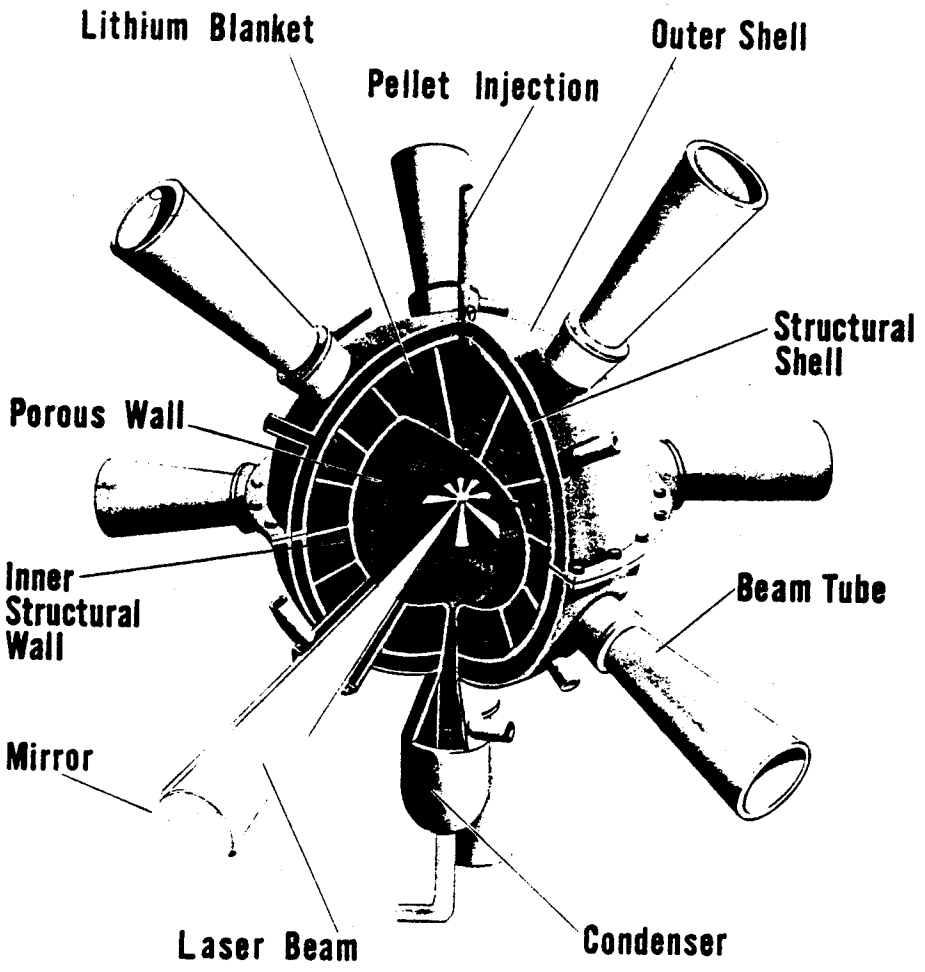

Fig. 3.2. LASL Wetted Wall Chamber.

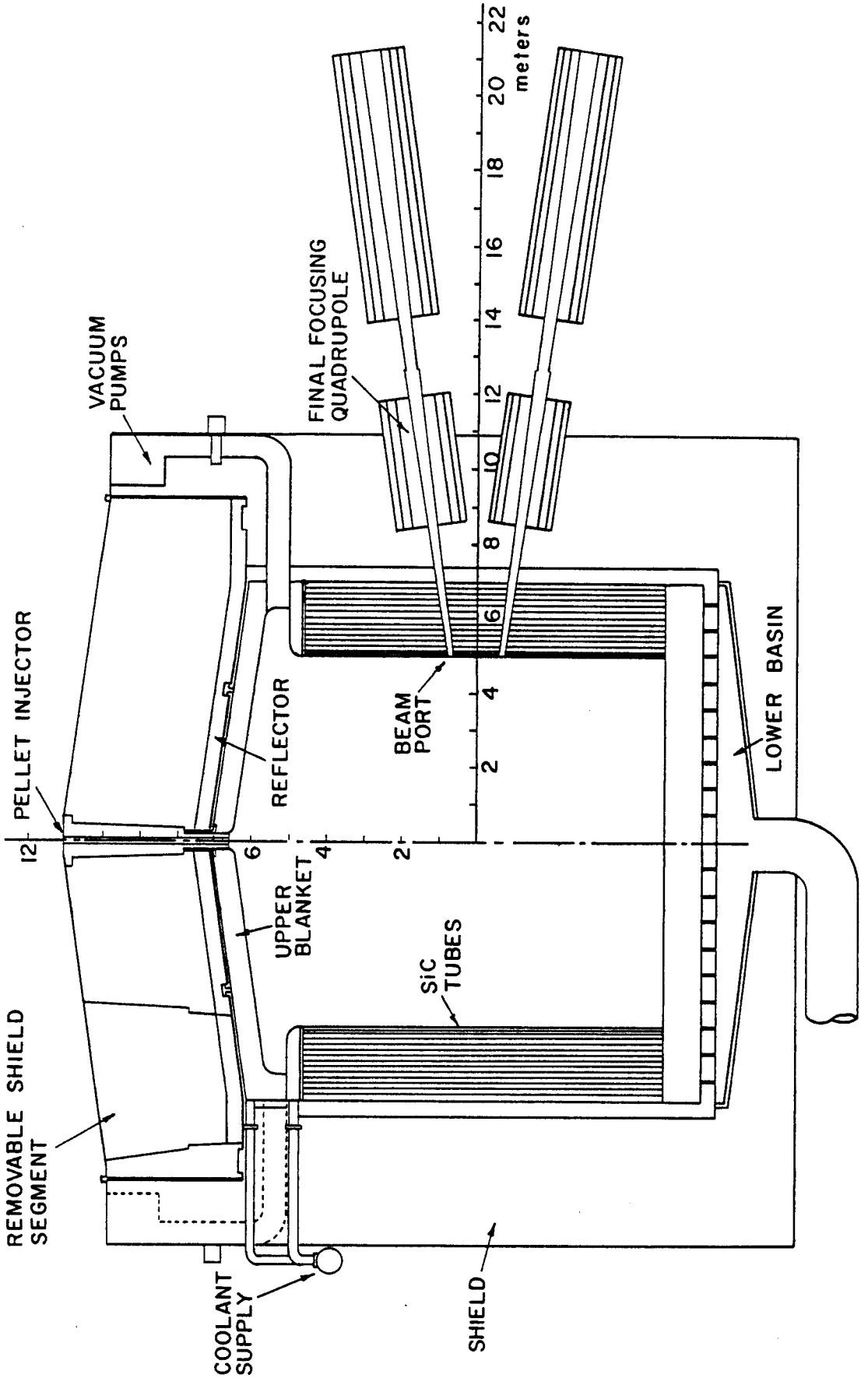

Fig. 3.3. HIBALL Chamber.

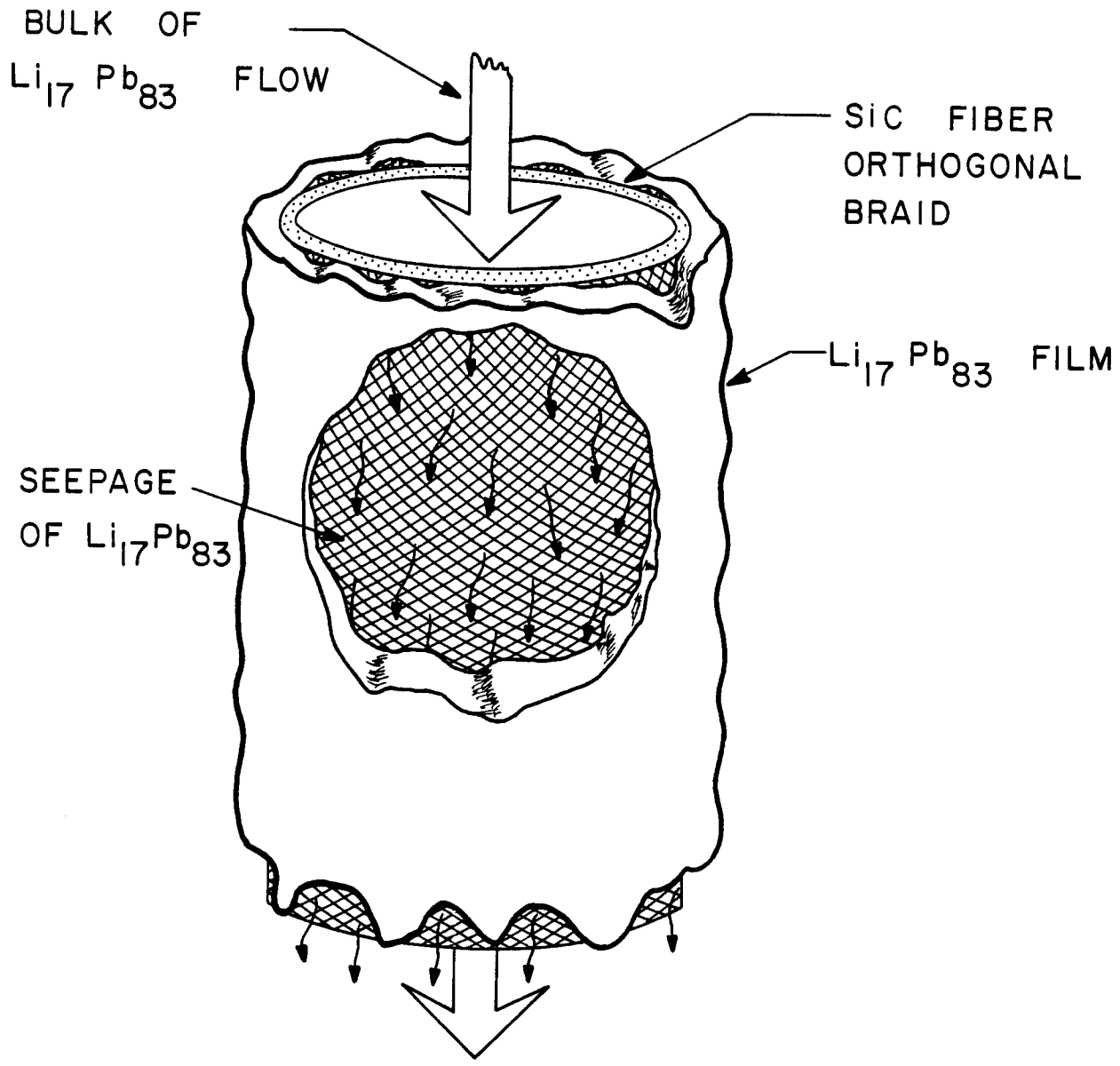

Fig. 3.4. INPORT Unit Concept.

In all of these schemes, protection of the upper and lower parts of the cavity is difficult. For this reason they are more suitable for non-symmetric illumination. The bottom part usually consists of a pool which is the sump for the liquid metal on its way out of the cavity. The upper part of the cavity is more difficult to protect. In HYLIFE, a graphite plug was used with an unspecified means of cooling. In HIBALL, the roof of the cylindrical cavity consisted of pie-shaped wedges of rigidized SiC frames covered with porous SiC fabric. The liquid metal which traversed the upper part then flowed through tubes in the back rows of the INPORT units where the nuclear heating is low. The total energy gain was thus controlled to be consistent with the remaining LiPb.

The two sided illumination in HYLIFE meant that a small number of beams had to penetrate the forest of liquid metal jets from only two sides. At these locations the jets were manipulated in a special way as shown in Fig. 3.5. It is difficult to imagine 32 beams penetrating this cavity from all sides, especially from the bottom pool. In HIBALL the beam ports came through the vertical sides of the cylindrical cavity and consisted of collars woven from rigidized SiC. They were cooled with the flowing LiPb and were porous only on the outer surface. Such a design would also be difficult to implement in the upper and lower parts of the cavity and is therefore not suitable for uniform illumination.

In the wetted wall design shown in Fig. 3.2, uniform illumination is indicated albeit with a small number of beams. This may be possible if the pool on the bottom is small enough that it will not interfere with beam placement. It is questionable if this can be done with 20-32 beams.

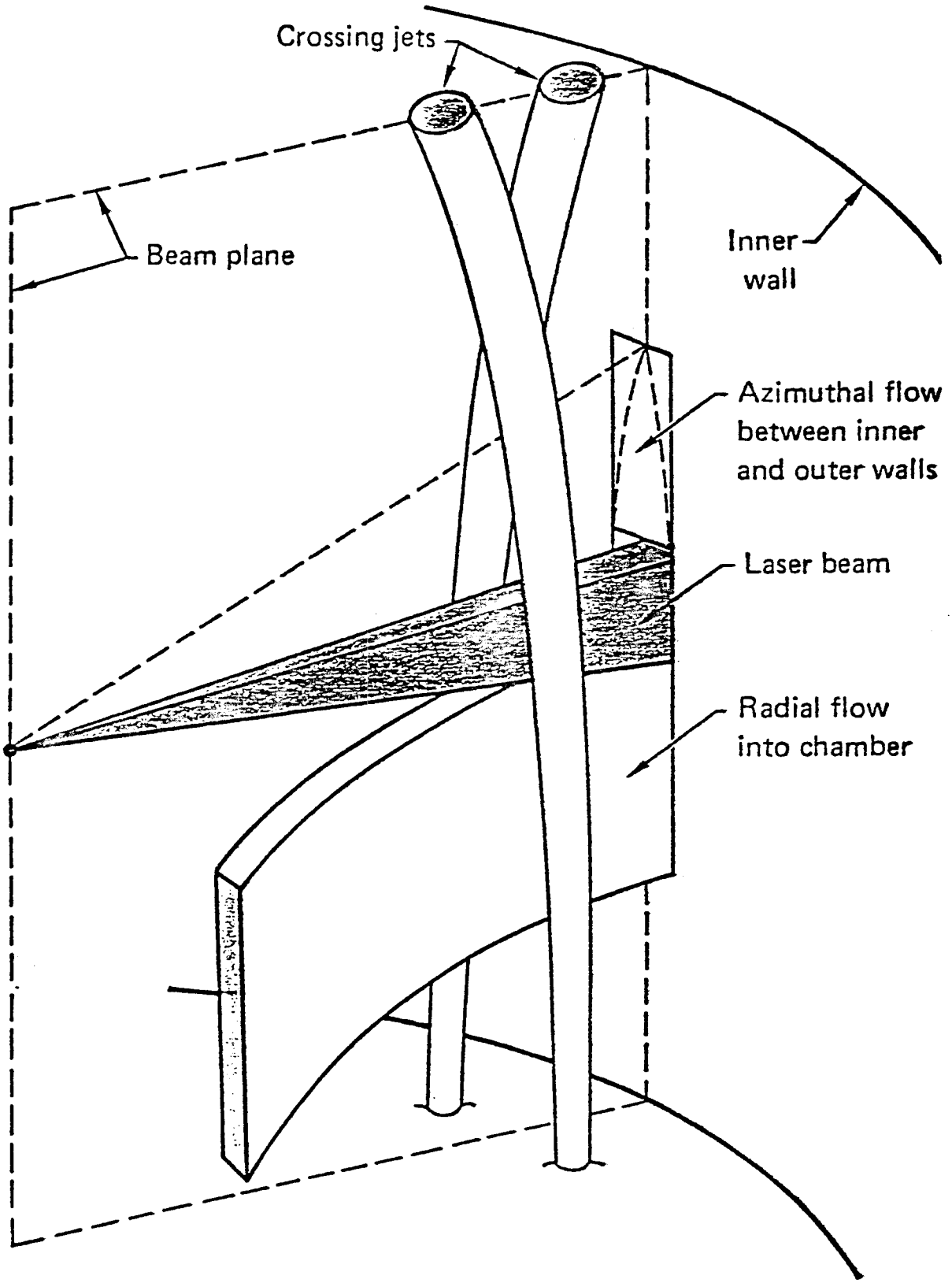

Fig. 3.5. HYLIFE Jets in Beam Vicinity.

Up until now we have concentrated on only one aspect of uniform illumination, namely placement of beams. Other important aspects such as final mirror contamination and protection is presumably the same for uniform and non-uniform illumination. This is only partly true, because in non-uniform illumination such as in HYLIFE, it is possible to place the final focusing mirrors a very long distance away, as much as 50-100 m from the cavity, bringing into play the $\frac{1}{R^2}$ factor. In uniform illumination this implies an enormous structure would be needed to support the mirrors all around the cavity at a long distance making it very impractical. A more reasonable distance for uniform illumination is 10-25 m. At this distance, it would be difficult to guarantee that the mirrors would remain uncontaminated with blast generated spray and will certainly suffer radiation damage.

In conclusion it would appear that liquid metal protection, be it with jets or wetted walls, for uniform illumination using more than 12 beams is extremely difficult if not impossible.

Buffer Gas Protection

A buffer gas has sometimes been proposed as a means of mitigating high surface wall heating. The buffer gas can stop x-rays and target debris and then radiate the energy to the cooled first wall over a longer time scale. It offers no protection against neutron damage to structures. Problems associated with buffer gas protection are laser gas breakdown, shock wave and fireball effects on the first wall, control of the composition and density of the gas in the cavity, pumping the low density gas and finally, extracting the energy from the gas. Such a scheme is more suitable with particle beam inertial fusion where a preionized channel is sometimes needed for beam propagation. Because the emmissivity and transparency of the gas is such a strong

function of temperature, problems sometimes arise in radiating the energy to the first wall fast enough to allow a reasonable rep-rate. If the energy cannot be extracted by radiation, then the gas has to be cooled by pumping it through suitable heat exchangers. Because of the low gas density, extracting the energy in this way is very inefficient and impractical.

To date, the only laser design study using buffer gas protection is SOLASE,[4] a design by the UW finished in 1978 and shown in Fig. 3.6. In SOLASE a neon buffer gas of < 1 torr pressure was used because it has the highest laser induced gas breakdown threshold, followed closely by helium. It has a relatively high stopping power for x-rays and ions and is inert and therefore compatible with the graphite first wall used in the cavity. The blanket design chosen for SOLASE consisted of Li_2O particles 100-200 μm in diameter flowing by gravity through a graphite compartmentalized structure. Such a blanket scheme is not compatible with uniform illumination because the upper and lower portions of the cavity are not available for beam placement. This, however, has nothing to do with buffer gas protection.

Although the use of buffer gas as first wall protection in ICF is a very complex subject, it must be concluded that its use cannot be ruled out strictly on the basis of uniform illumination.

Magnetic Protection

Magnetic protection such as the one used in the design by LANL[5] shown in Fig. 3.7 is effective only against ions, but obviously not against x-rays or neutrons. In this scheme a solenoidal magnetic field fills the cavity and diverts the ion debris to collection regions at the end of the cavity. Symmetric placement of the laser beams is complicated by the end cell ion collection plates and by the magnet coils that must necessarily surround the

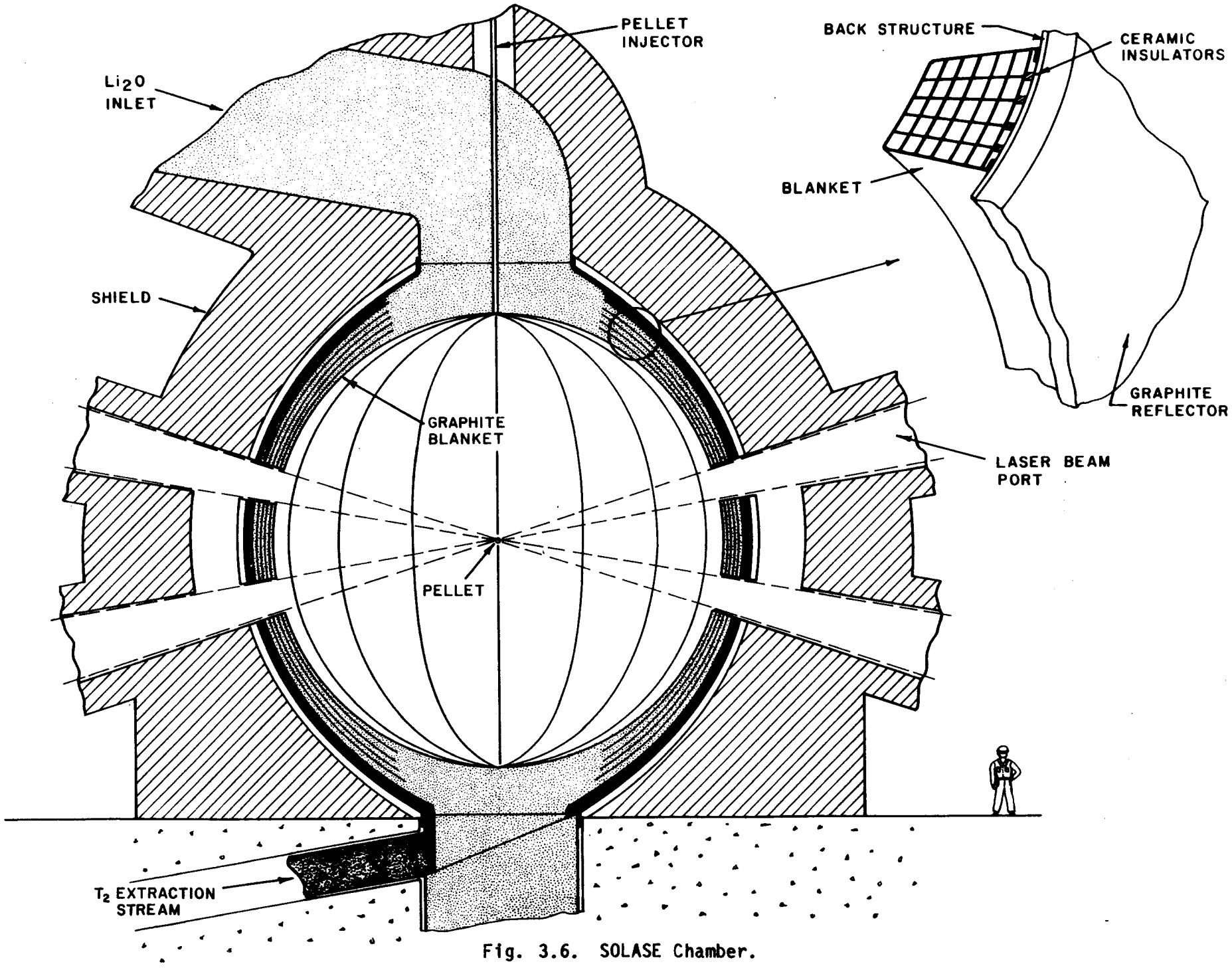

Fig. 3.6. SOLASE Chamber.

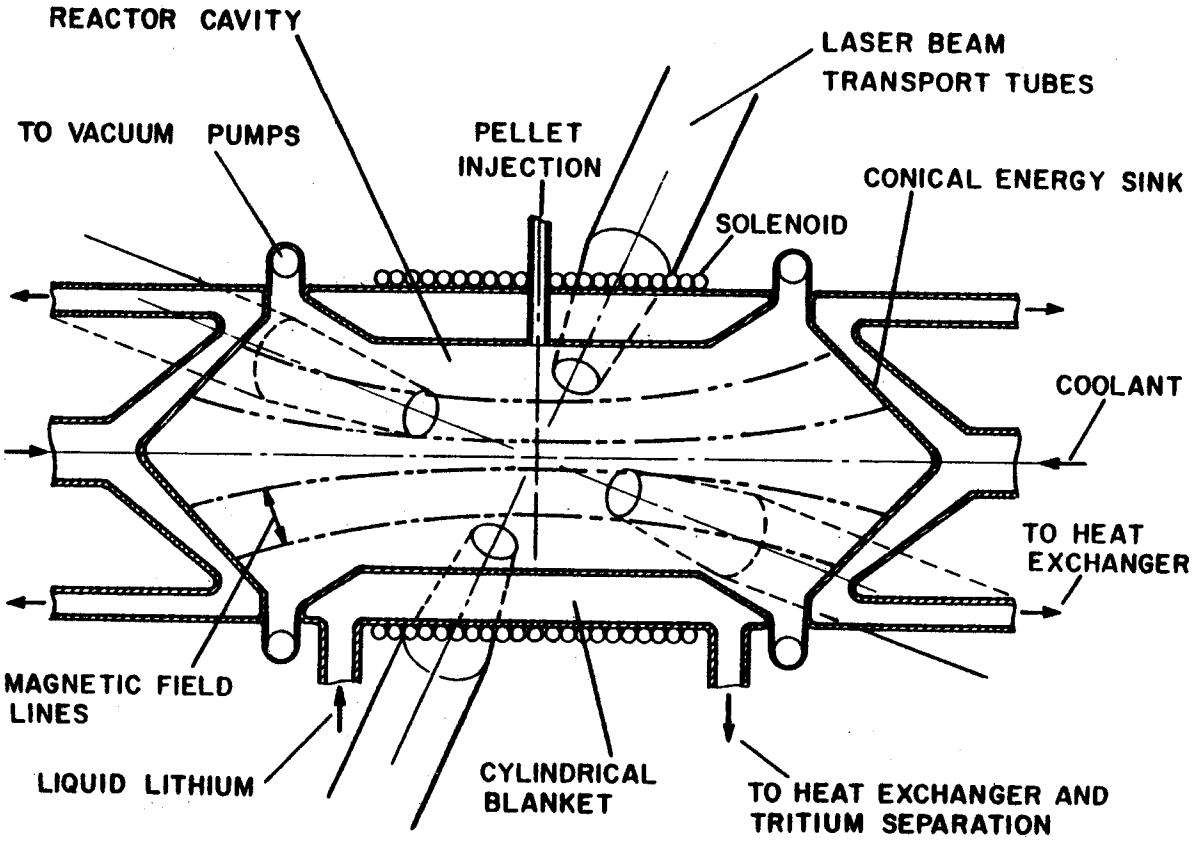

Fig. 3.7. LASL Magnetically Protected Chamber.

radial blanket. It is unlikely that symmetric illumination could be achieved in such a scheme. Aside from that, the magnetic field would impede the pumping of a liquid metal if it is used in the blanket.

Large Cavities

In principle, it is possible to make the cavity of an ICF reactor large enough as to reduce the instantaneous wall loading and even radiation damage to a low enough level, and allow it to survive the lifetime of the reactor. In practice, physical and economic considerations place restrictions on just how far such a concept can be taken. A great deal depends on the materials used for the first wall, their high temperature properties and sputtering characteristics.

A bare wall cavity design was used by the Westinghouse PRDA[6] to investigate both laser and heavy ion beam drivers. The spherical cavity had a diameter of ~ 23 m and the first wall consisted of thin wall HT-9 tubes coated with tantalum with a lithium coolant on the inside. The tantalum coating apparently is needed to mitigate severe thermal cycling. The laser version of this cavity is shown in Fig. 3.8.

One of the major problems of bare metallic walls is the large instantaneous temperature rise on the surface following a shot, leading to evaporation or melting with rather deleterious consequences. It may be possible to reduce the cavity size if the first wall is made of a material such as SiC or graphite which have high temperature properties far superior to any metals. A combination of a graphite first wall radiating to an actively cooled metallic wall may be the best compromise from the standpoint of size reduction and maintainability. Such a scheme was initially proposed by LLNL[7] where a

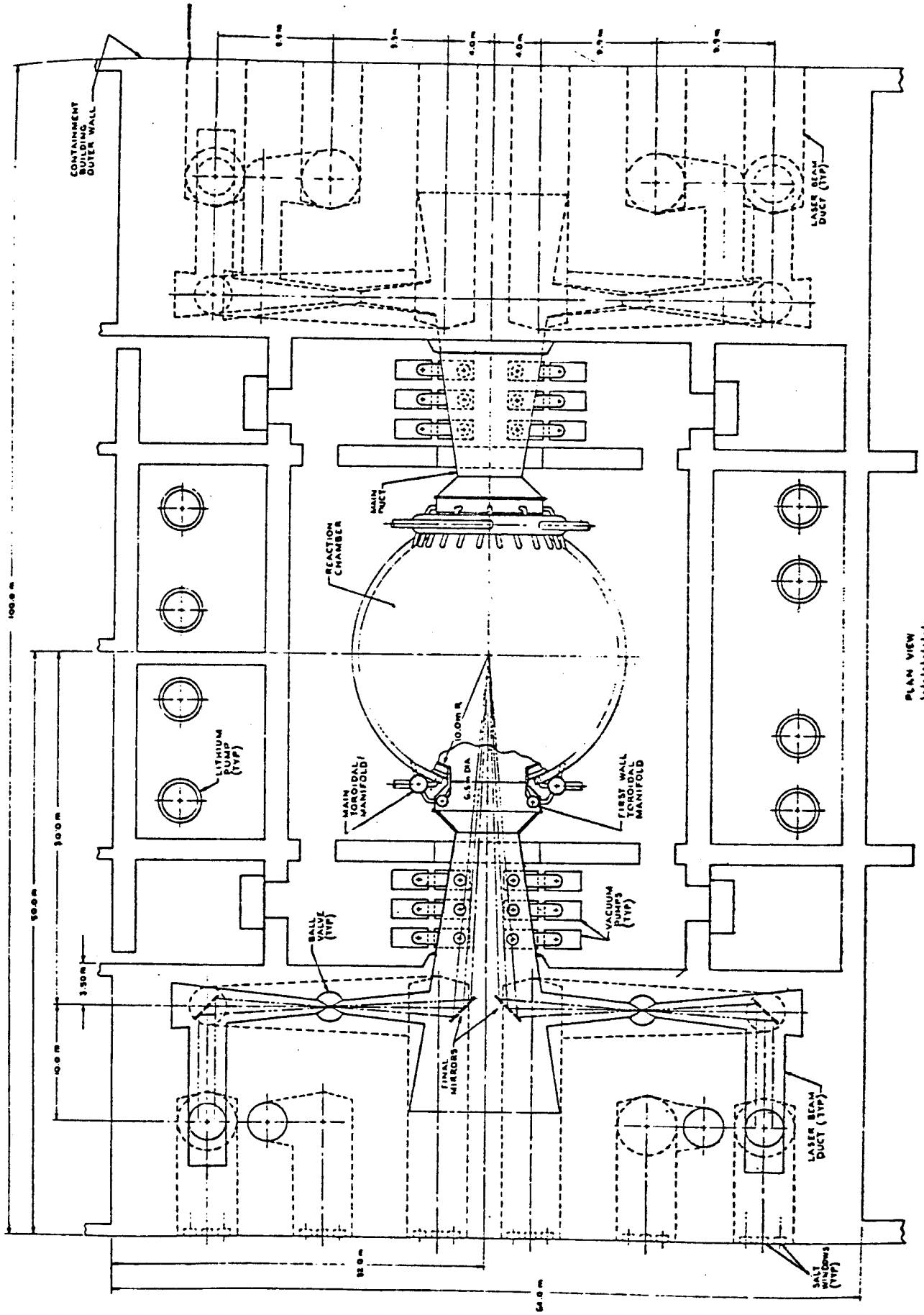

Fig. 3.8. Westinghouse Laser Driven Chamber.

sacrificial graphite wall was used to protect a Li cooled metal first wall. This scheme would be very compatible with uniform illumination.

Conclusions

Of all the first wall protection schemes considered, two appear to have the greatest potential for uniform illumination. They are buffer gas protection and large cavity size. Buffer gas protection has severe limitations with respect to laser gas breakdown, energy extraction and gas handling. A bare wall large cavity size is the most suitable scheme for uniform illumination. The eco-nomic penalty is not too great because experience shows that the cost of the cavity does not usually dominate the cost of the overall fusion power plant. As an example, in SOLASE[7] the cost of the cavity was only 3.6% of the reactor plant equipment and only 2.4% of the total direct costs.

References for Chapter 3

1. M. Monsler et al., "The HYLIFE Inertial Confinement Fusion Reactor Conceptual Design," Lawrence Livermore Laboratory Report UCRL-50021-78, p. 9-1.

2. L.A. Booth et al., Los Alamos Scientific Laboratory Report LA-4858-MS (Feb. 1972).

3. B. Badger et al., "HIBALL, A Joint Federal Republic of Germany - University of Wisconsin Conceptual Heavy Ion Beam Fusion Reactor Design Study," University of Wisconsin Fusion Engineering Program Report UWFDM-450, Sept. 1981.

4. G.A. Moses et al., "The SOLASE Conceptual Laser Fusion Reactor Study," Proc. of 3rd Top. Mtg. on the Tech. of Cont. Nucl. Fusion (Santa Fe, NM, May 1978), p. 448.

5. T. Frank et al., in Proc. 1st Top. Mtg. on the Tech. of Cont. Nucl. Fusion (San Diego, 1974), p. 83.

6. E.W. Sucov, "Inertial Confinement Fusion Central Station Electric Power Generation," Westinghouse Fusion Power Systems Report WFPS-TME-81 (Feb. 1981).

7. J. Hovingh, "First Wall Studies of a Laser Fusion Hybrid Reactor Design," UCRL-78090, Lawrence Livermore Laboratory, Sept. 1976.

8. "Conceptual Balance of Plant Design and Cost Study for the SOLASE Laser Fusion Power Reactor," UE&C/UW-791511, Nov. 15, 1979.

4. SIRIUS PRECONCEPTUAL DESIGN

4.1 Overview of SIRIUS Design

SIRIUS is a preconceptual design for a laser fusion reactor with symmetric illumination of the fusion target by the laser driver. Table 4.1-1 is a parameter list for SIRIUS. The reactor is designed to produce 737 MW of fusion power which becomes 913 MW when energy multiplication in the blanket is included. This fusion power results from microexplosions of fusion targets with 134 MJ released per shot at a rate of 5.5 shots per second. A 2.1 MJ KrF laser system, operating at a wavelength of 0.248 μm and divided into 32 beams, drives these microexplosions. The target yield consists of 100 MJ per shot of neutrons and 34 MJ in x-rays and ion debris.

The preconceptual design of SIRIUS is shown schematically in Fig. 4.1-1. The major components of this design are the final laser optics and beam transport, a system of silicon carbide tiles to protect the surface of the first wall from the thermal load of 34 MJ per shot from the target generated x-rays and ion debris and the blanket reflector and shield. Since the density of the gas in the reaction chamber must be low to allow propagation of the laser beams, the x-ray and debris energy is deposited on the innermost parts of the reaction chamber in a very short time so that these components may experience very high surface temperatures. In this design, silicon carbide tiles, which are 1.25 cm thick, absorb these x-rays and ions. The tiles are far enough away from the microexplosion that their surface temperatures remain below 2650°C and they will not be damaged by the surface heat load. They will then radiate energy to the metallic first wall over a longer period, thus acting as thermal capacitors. The maximum surface temperatures on the first wall will

Table 4.1-1 SIRIUS Parameter List

Quantity	Value	Units
Thermal power	913	MW
Fusion power	737	MW
Target yield	134	MJ
X-ray energy/shot	8	MJ
Debris energy/shot	26	MJ
Neutron energy/shot	100	MJ
Repetition rate	5.5	Hz
Laser output	2.1	MJ
Target gain (see Sect. 4.2)	64	---
# of laser beams (see Sect. 4.2)	32	---
Radius of final focusing mirrors	1.05	meters
f # of final focusing mirrors	f/10	---
Focal length of mirrors	21	meters
Laser wavelength	0.248	microns
First wall protecton	silicon carbide tiles	---
Distance from target to tiles	7.8	meters
Neutron wall loading at tiles	0.7	MW/m^2
Thickness of tiles	1.25	cm
Maximum temperature in tiles	2647	°C
Thickness of blanket	0.4	meters
Distance from target to blanket	8	meters
Breeding material	liquid natural lithium 95%	---
Blanket structure	HT-9 ferritic steel 5%	---
Thickness of reflector	0.4	meters
Distance from target to reflector	8.4	meters
Reflector material	10% lithium, 90% HT-9	---
Thickness of shield	1.0	meters
Distance from target to shield	9.8	meters
Shield material	concrete	---
Tritium breeding ratio	1.14	---
Energy multiplication	1.32	---
Neutron damage to first wall	5.35	dpa/FPY in iron

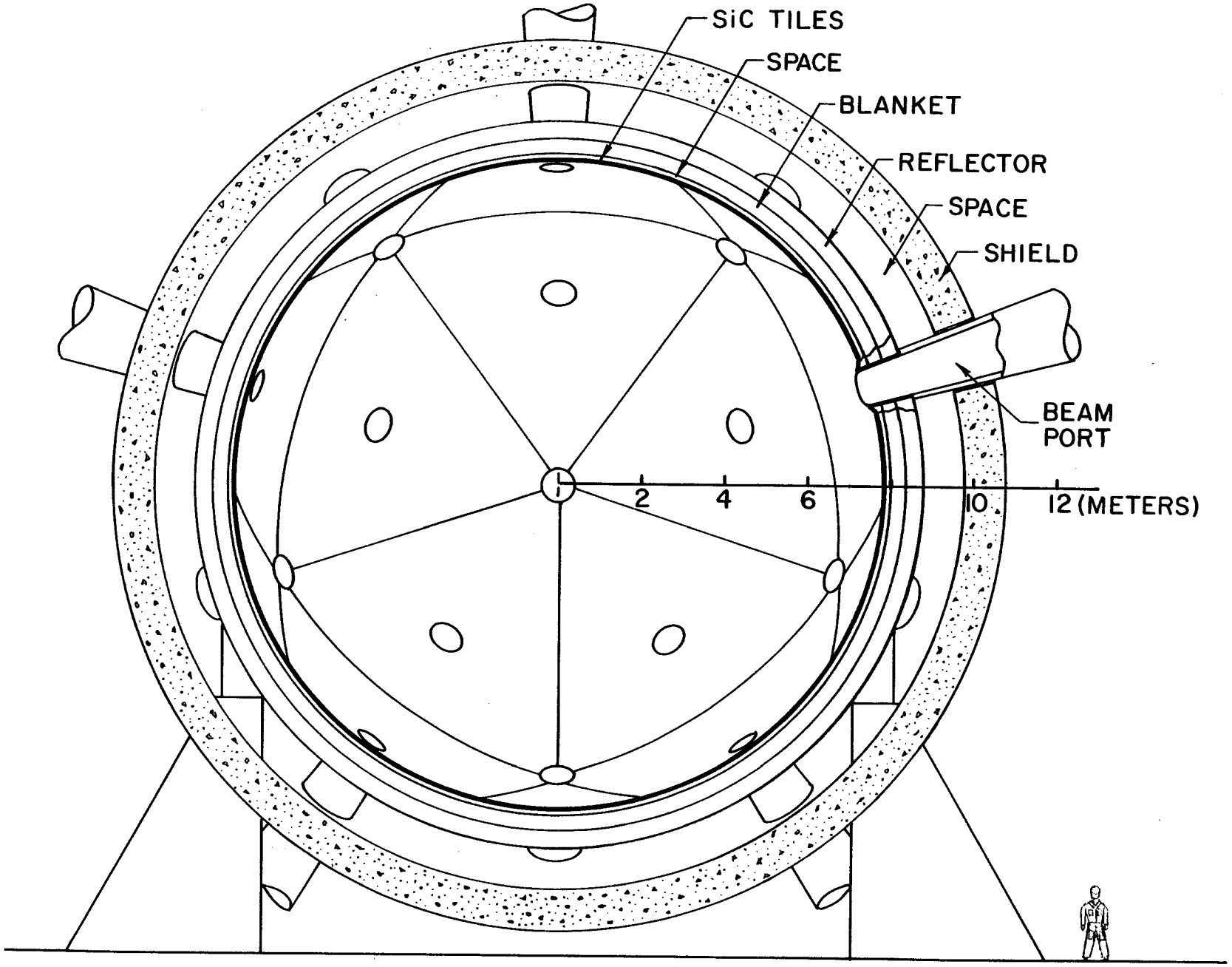

CROSS SECTION OF SIRIUS CHAMBER

Fig. 4.1-1

be much lower and fluctuations in temperature leading to thermal fatigue of the first wall will be mitigated by the tiles.

The symmetric arrangement of the laser beams has led to a geometrical design of the reaction chamber and optical system different from those for non-symmetrical target illumination. Requirements on the size of the final laser optics are dictated by laser damage thresholds to the optics. This and the illumination symmetry needs for target performance led to a particular choice of f-number. For SIRIUS, these requirements determine that f/10 optics are adequate for a 32 beam system and that the final mirrors should be 1.05 meters in radius. Thus, the focal length of the final mirrors is 21 meters. For this optical system, only 2% of the solid angle seen by the target is taken up by beam ports and the effect on the tritium breeding and energy multiplication is minimal. However, the 32 final mirrors located at 21 meters from the target position cause design problems if periodic maintenance to the tiles is to be carried out without upsetting the optical alignment. The design of the tiles as triangular panels supported at the centers by beam ports allows their removal and replacement with minimal movement to the final laser mirrors. The presence of the tiles reduces the thermal damage to the blanket, reflector and shield so that they will not need to be replaced during the life of the reactor.

The blanket, reflector and shield have been designed to provide a tritium breeding ratio of 1.14 and an energy multiplication of 1.32 with liquid lithium as a breeding material, where the effects of neutron losses in beam tubes have been included. The blanket is only 40 cm thick so that the total volume of blanket is not excessive even though the radius of the first wall is 8 meters. In the blanket, liquid lithium flows freely in between the ferritic

steel inner and outer shells to avoid the complexity of the geometry of the beam ports.

The idea of a so-called bare wall reactor cavity design is not new. An earlier bare wall design proposed by Westinghouse is reviewed in Section 3 of this report. It is also noted that this type of design was proposed by LLNL in the early days of ICF conceptual reactor design activity. We propose to return to this type of design for the SIRIUS reactor in order to more completely analyze its economic and technical implications. Recent designs, such as HYLIFE and HIBALL, have included a blanket within the vacuum boundary (i.e., first wall) to protect this first wall from neutron damage. These designs brought the first wall closer to the target and increased the average power density of the reactor as defined by power/volume within blanket and cavity. In addition, the HYLIFE design with its liquid lithium jets was tailored to accommodate very large target yields of 4000 MJ. The two-sided illumination in HYLIFE offered the possibility of placing the final optics at as much as 100 meters from the target explosion. This gives great flexibility to the geometry of structures within the target chamber (e.g., lithium jets).

In the case of uniform illumination, the essential volume of interest is the sphere enclosed within the radius of the final optical elements that are uniformly positioned around the target chamber. Once this volume is established by focusing and radiation damage criteria, one is left with the design of the cavity and blanket to fit inside. The essential question here is: how much does this volume within the final mirrors cost and how much does this cost change as the ratio of blanket structure volume to vacuum volume changes? We believe that this cost is quite insensitive to this ratio and therefore, there is little economic incentive to try to minimize the first wall radius

and increase the power density of the blanket and cavity volume. In other words, the average power density of the volume within the radius of the final optics does not change when the reactor blanket and cavity are made smaller. Hence, there is little economic incentive to make them smaller. There may of course be a technical incentive.

We have learned from this study that a first wall radius of 8 meters is sufficient to reduce the radiation damage to the wall and blanket to the extent that they should last for the lifetime of the plant. Furthermore, if the first wall is protected by a passive shield that operates at high temperature and radiates to the wall in a nearly steady state fashion, then the wall can withstand the thermal cycling that comes from the short range x-ray and ion debris from the target. We propose that this shield be composed of thin SiC tiles that can be periodically replaced while disturbing only a small fraction of the final optic elements.

The radius of the first wall is limited by both radiation damage and thermal loading. The radiation damage constraint is derived from the cumulative damage over time while the thermal constraint is determined from the per shot loading. At yields of ~ 100-200 MJ per shot and total power of ~ 1000 MW, this radius demanded by these two constraints is about the same. This is a key design consideration for SIRIUS. The design cannot accommodate the very large yields (4000 MJ) that HYLIFE was designed to handle. On the other hand, we believe that we are looking in the proper range of yields for direct drive laser fusion.

With our better understanding of radiation damage to structural materials and our more complete understanding of economic trade-offs we believe that it

is worthwhile to re-investigate this relatively simple design concept for application to direct drive laser fusion.

4.2 Energy Spectrum of Neutrons, Radiation and Target Debris

The target used for estimating the energy spectrum of radiation and charged particles striking the chamber wall was a 2 mm radius plastic (CH_2) shell with an inner layer of cryogenic DT fuel (Fig. 4.2-1). The target was driven by 2.1 MJ of KrF laser light (248 nm) having a 20 ns time-tailored laser pulse. The target performance discussed here might not be optimal (conceivably the gain could be almost a factor of two higher), but the calculated energy emission spectrum is still expected to be characteristic of optimal direct-drive targets with laser energies around 1 MJ. The target size and laser pulse were chosen to produce an implosion consistent with current thinking about hydrodynamic stability[1] and irradiation uniformity.[2] Specifically, the in-flight aspect ratio (shell radius divided by shell thickness) was typically below 50, and the initial laser irradiation was above 80% of the tangential focal distance (focus ratio = 0.8).

The implosions were calculated with the one-dimensional hydrodynamics code LILAC[3] which has been used extensively at the University of Rochester to analyze laser fusion experiments. The code contains a realistic equation-of-state,[4] multifrequency-group radiation[5] transport, and the transport of charged particles from fusion reactions. Neutron transport was not included in the calculation. The neutron energy spectrum incident on the reactor wall was inferred after the calculation as described below. The laser energy was deposited by a ray-trace algorithm which includes refractive effects. (To achieve high uniformity of drive the laser must be focused behind the target so that the beams overlap and each beam irradiates approximately an entire hemisphere, making refraction an important factor.)

PRELIMINARY TARGET DESIGN FOR THE SIRIUS REACTOR

UR LLE

- **TARGET:**

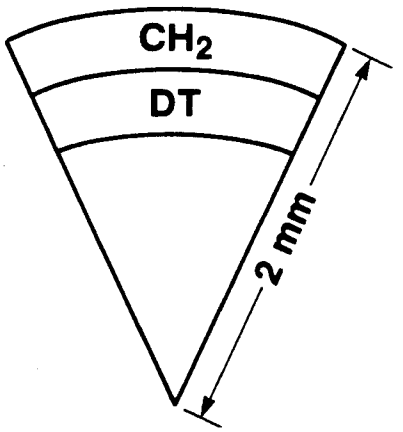

- **LASER PULSE (248 nm):**

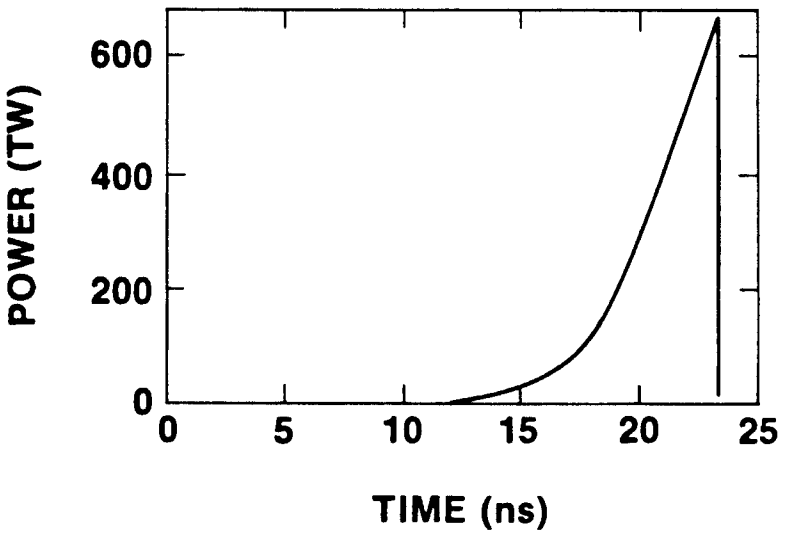

A110

Figure 4.2-1

The target performance is summarized in Table 4.2-1. Two cases are considered. Case (a) assumed a flat-top laser pulse at tangential focus. A considerable amount of energy was lost due to refraction, resulting in only 63% absorption. These results were used for the initial SIRIUS reactor design. Case (b) used a quadratic beam profile (i.e., less laser energy at the beam edge and more at the center) with the beams focused at 80% of the tangential focus position. This focus gives near-optimal uniformity for a 32-beam system. Considerably less refraction occurs in Case (b), resulting in a higher gain and permitting a reduced incident laser energy. The improved performance of Case (b) with respect to absorbed energy is due to improved beam timing. Gains higher than 110 at this absorbed laser energy are possible by: (a) further optimizing the laser/target timing, (b) using polarized DT fuel[6] or (c) relaxing the presently accepted constraints on hydrodynamic stability and uniformity of irradiation.

The energy spectrum of x-rays emitted from the target is shown in Fig. 4.2-2. The high frequency component is the result of Bremsstrahlung emission at electron temperatures around 40 keV during the burn. The neutron spectrum in Fig. 4.2-2 was inferred, assuming neutrons make at most one collision (isotropically) within the target. Cross sections of 0.92 b and 0.62 b were used for deuterium and tritium respectively, and a fuel ρR of 1.35 g/cm^2 was used, taken from the implosion simulation at the peak of the burn. Only 22% of the neutrons had collisions, which justifies the single-scatter approximation. If higher accuracy for the spectrum of scattered neutrons is required, then account should be taken of the known anisotropy of the neutron cross section of 14 MeV. Finally, the spectrum of charged particles is shown in Table 4.2-2.

Table 4.2-1. Target Performance for the SIRIUS Reactor

		Case (a)	Case (b)
1.	Gain	64	110
2.	Incident Laser Energy	2.1 MJ	1.6 MJ
3.	Laser Absorption	63%	88%
4.	Absorbed Laser Energy	1.3 MJ	1.4 MJ
5.	Yield	134 MJ	172 MJ
	Neutrons	108 MJ	138 MJ
	Target Debris	18 MJ	26 MJ
	Radiation	8 MJ	8 MJ

Case (a) Flat-top pulse at tangential focus. These results were used for the initial SIRIUS design.

Case (b) Quadratic laser pulse at 0.8 times tangential focus.

Table 4.2-2. Spectrum of Charged Particles from Target Debris

Ions	Velocity
1.3×10^{20} D	
1.3×10^{20} T	3×10^{8} cm/s
1.0×10^{20} α	
1.4×10^{20} C	$4\text{-}7 \times 10^{8}$ cm/s
0.7×10^{20} H	

EMISSION SPECTRUM FROM TARGET USED IN SIRIUS REACTOR DESIGN

UR LLE

- X RAYS (8.6 MJ - 6% of yield)

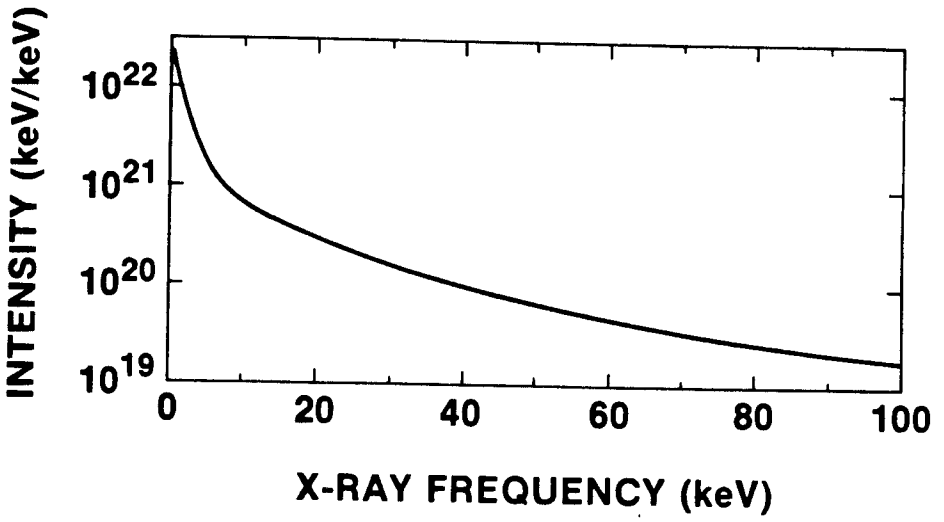

- NEUTRONS (5×10^{19} neutrons - 75% of yield)
  - Single isotropic scattering approximation

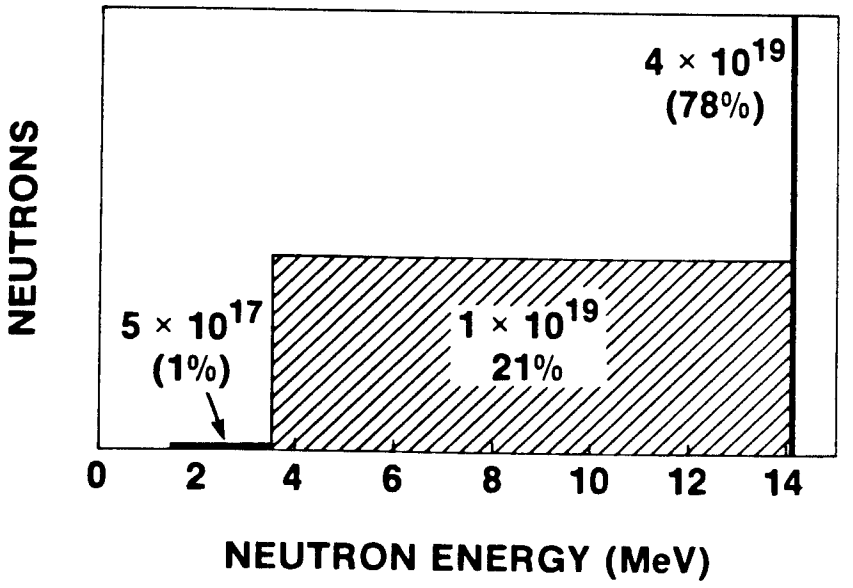

A109

Figure 4.2-2

The partitioning of energy among target products is about: 80% neutrons, 14% charged particles and 6% x-rays. Including neutron deposition in the calculation would reduce the neutron percentage by about 10%, with the energy going mainly to the charged particles.

References for Section 4.2

1. C.P. Verdon, R.L. McCrory, R.L. Morse, G.R. Baker, D.I. Meiron and S.A. Orszag, Phys. Fluids 25, 1653 (1982).
2. S. Skupsky and K. Lee, J. Appl. Phys. 54, 3662 (1983).
3. See for example: B. Yaakobi et al., Phys. Rev. A 19, 1247 (1979).
4. B.I. Bennet, J.D. Johnson, G.I. Kerley and G.T. Road, LA-7130 (1979).
5. W.F. Heubner, A.L. Mertz, N.H. Magee and M.F. Argo, LA-6760-M (1977).
6. R.M. More, PRL 51, 396 (1983).

4.3 Neutronics & Radiation Damage to First Wall & Blanket

4.3.1 Impact of Laser Optics Design on Blanket Neutronics Performance

The number of beams and the final optics f# are determined from the target illumination uniformity requirements. These parameters will also impact the solid angle fraction subtended by the beam ports and hence will influence the blanket tritium breeding ratio (TBR) and energy multiplication (M). The fraction of solid angle subtended by beam ports is given by

$$\Delta\Omega/4\pi = \frac{N}{2}\left[1 - \frac{2f}{\sqrt{4f^2 + 1}}\right] \qquad (4.3\text{-}1)$$

where N is the number of beams and f is the f# of the final focusing optics. Figure 4.3-1 gives the fractional solid angle predicted by Eq. 4.3-1 for 12, 20, and 32 beams with different values for the f#.

However, it is necessary to emphasize the fact that several design constraints will limit our ability to arbitrarily change the number of beams and the f#. For a given total laser output and a laser damage fluence threshold for the coatings of the final optics, the area of these optics must remain the same. Hence, the area of final mirrors per beam must be increased if the number of beams is reduced. Furthermore, for the damage to these coatings from the x-rays, ion debris, and neutrons produced at the target to remain the same, using fewer beams must be accompanied by decreasing the f# such that the spacing of the final optics from the target remains unchanged. Our analysis indicates that in order to satisfy these constraints, N/f^2 should remain the same. It is interesting to note that for $f \gg 1/2$, Eq. 4.3-1 reduces to

$$\Delta\Omega/4\pi = N/16\ f^2\ . \qquad (4.3\text{-}2)$$

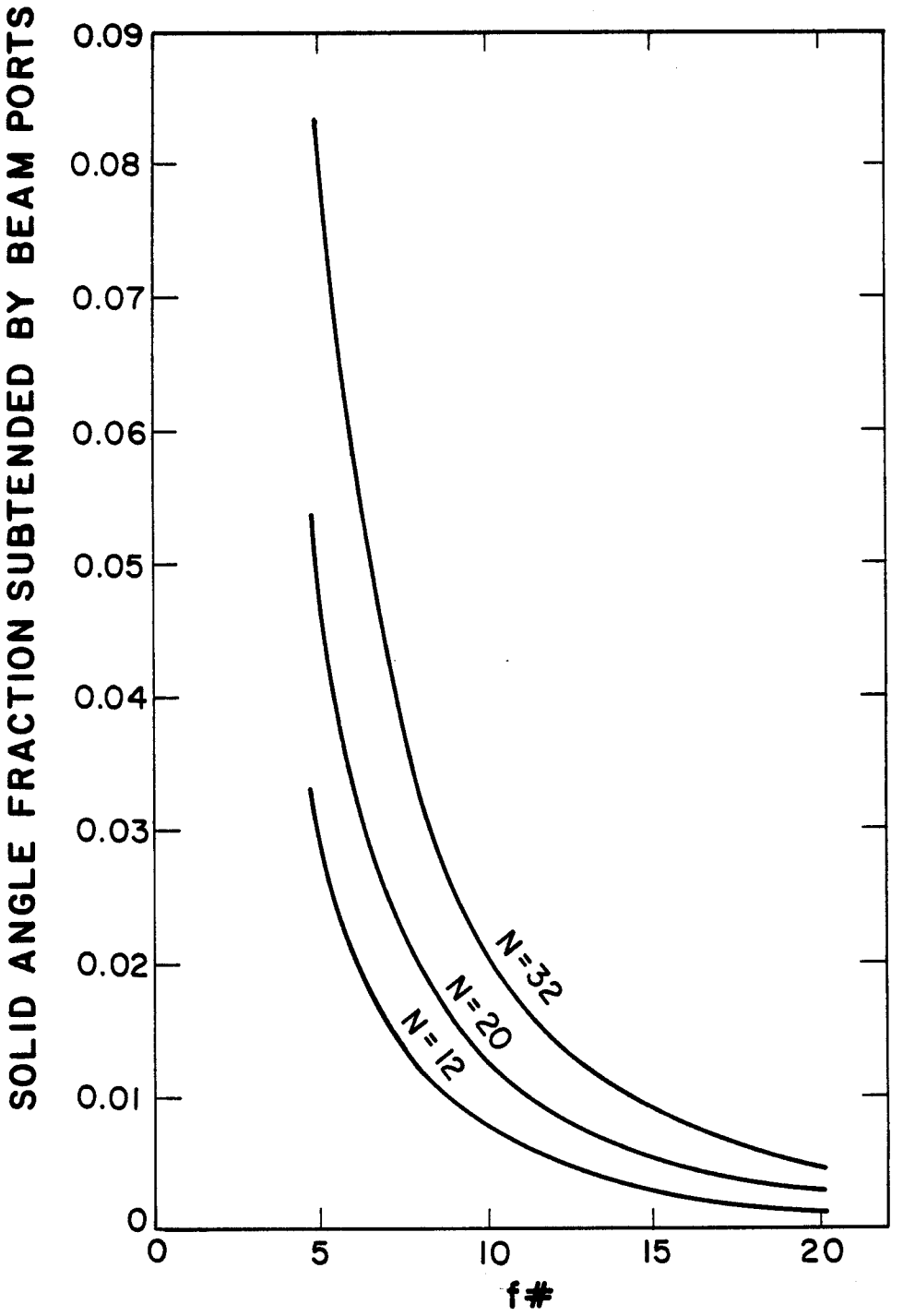

Fig. 4.3-1. Variation of fractional solid angle subtended by beam ports with number of beams and f number of final focusing optics.

Hence, the beam ports will occupy the same solid angle if the damage to the coatings of the final optics from both laser and fusion products is to be fixed. On the other hand, if only the laser damage is constrained, one can still vary the f# arbitrarily and get different solid angles.

The base case considered for the SIRIUS design utilizes 32 beams with f/10 final optics. This implies that the solid angle subtended by the 32 beam line penetrations is only ~ 2% of the total solid angle at the target. This implies that ~ 2% of the source neutrons will stream directly into the ports and will not contribute to tritium breeding and nuclear heating. However, some of the neutrons reentering the cavity after diffusing in the blanket might stream through the beam ports, yielding further reduction in TBR and energy multiplication. Meier[1] performed three-dimensional neutronics calculations for a spherical chamber with two diametrically opposed beam ports for Li and $Li_{17}Pb_{83}$ blankets. Natural lithium was used in both cases. The results indicate that both TBR and energy multiplication decrease at rates greater than predicted based on the loss of blanket coverage. Greater reduction was obtained for the Li-Pb case due to the (n,2n) reaction in lead that results in more neutrons reentering the cavity. Eight and twenty percent reduction in TBR was obtained for Li and Li-Pb, respectively, for ports subtending 5% of the total solid angle. Energy multiplication was reduced by 7 and 14% for Li and Li-Pb, respectively. Similar analysis was performed by Hovingh[2] for 12 and 20 beams with f# $\lesssim$ 5. Extrapolating from the results of Meier and Hovingh, we estimated the TBR to be ~ 2.5 and 8% less than the results without ports for the Li and $Li_{17}Pb_{83}$ blankets, respectively, for the reference SIRIUS design. Lower reduction in TBR for a $Li_{17}Pb_{83}$ blanket that utilizes highly enriched Li is expected as the ^6Li will absorb more of the

secondary neutrons produced in the Pb(n,2n) reaction resulting in less neutrons reentering the cavity. In this phase of the study only one-dimensional neutronics calculations, in which the beam ports are not modeled, have been performed. The blanket is designed to yield a TBR that has enough margin allowing for the expected reduction when the beam ports are included. We note that the results of Meier and Hovingh yield a conservative estimate for the reduction in TBR in the SIRIUS design as these results were calculated for a small number of large beam ports. In SIRIUS, where a large number of small beam ports is used, the neutrons reentering the cavity and streaming into the beam ports will have a larger probability of impinging on the sides of the penetration and contributing to tritium breeding and nuclear heating. Detailed three-dimensional neutronics calculations need to be performed in the future to quantify the TBR in the SIRIUS design with all blanket penetrations and heterogeneity effects included.

4.3.2 Calculational Model

The multigroup discrete ordinates ANISN code[3] was used to perform coupled neutronics and photonics calculations for the SIRIUS reactor. One-dimensional spherical geometry was used in the calculations. A P_3-S_8 approximation was used. A coupled 46 neutron-21 gamma group cross section library that consists of the RSIC DLC-41B/VITAMIN-C cross section data library[4] and the DLC-60B/MACKLIB-IV-82 response data library[5] was used.

The neutron source was considered to be an isotropic point source at the center of the cavity. The spectrum of neutrons emitted from the target was used to represent the source for the blanket calculations. This spectrum calculated by the University of Rochester based on single isotropic scattering approximation shows that 78% of the neutrons are emitted at 14.1 MeV without

having any collision in the target while 21% of the neutrons are emitted with energies in the range 3.5-14.1 MeV and 1% of the neutrons with energies in the range 1.5-3.5 MeV. The target calculations predict that 5×10^{19} neutrons are emitted per shot with a total yield of 100 MJ. This implies that the average energy of emitted neutrons is 12.5 MeV which is an indication of the spectrum softening resulting from neutron-target interactions. The neutron source intensity used in the calculations is 3.75×10^{20} n/s which is based on a 7.5 Hz repetition rate.

A schematic of the geometrical model used in the calculations is given in Fig. 4.3-2. Liquid lithium is used as the breeder and coolant. In this preconceptual design Li was chosen because of its lighter weight compared to $Li_{17}Pb_{83}$ resulting in reduced blanket support requirements. Furthermore, more neutrons will be reentering the cavity from a $Li_{17}Pb_{83}$ blanket. These neutrons might end up streaming into the beam ports resulting in larger reduction in both TBR and energy multiplication compared to the Li case. The ferritic steel alloy HT-9 is used for structure because of its resistance to radiation damage and its compatability with liquid lithium. A metallic reflector is used to enhance the energy multiplication in the system. SiC tiles are used to protect the blanket from the fusion products, particularly the x-rays and ion debris. A concrete biological shield is used behind the reflector. This shield is required to reduce the biological dose outside the shield to an acceptable level (~ 2.5 mrem/hr) that allows hands-on maintenance of auxiliary components outside the reactor during operation. Since in this stage of the study we are concerned only with blanket and reflector neutronics performance, a 1 m thick shield was included in the model to properly represent the

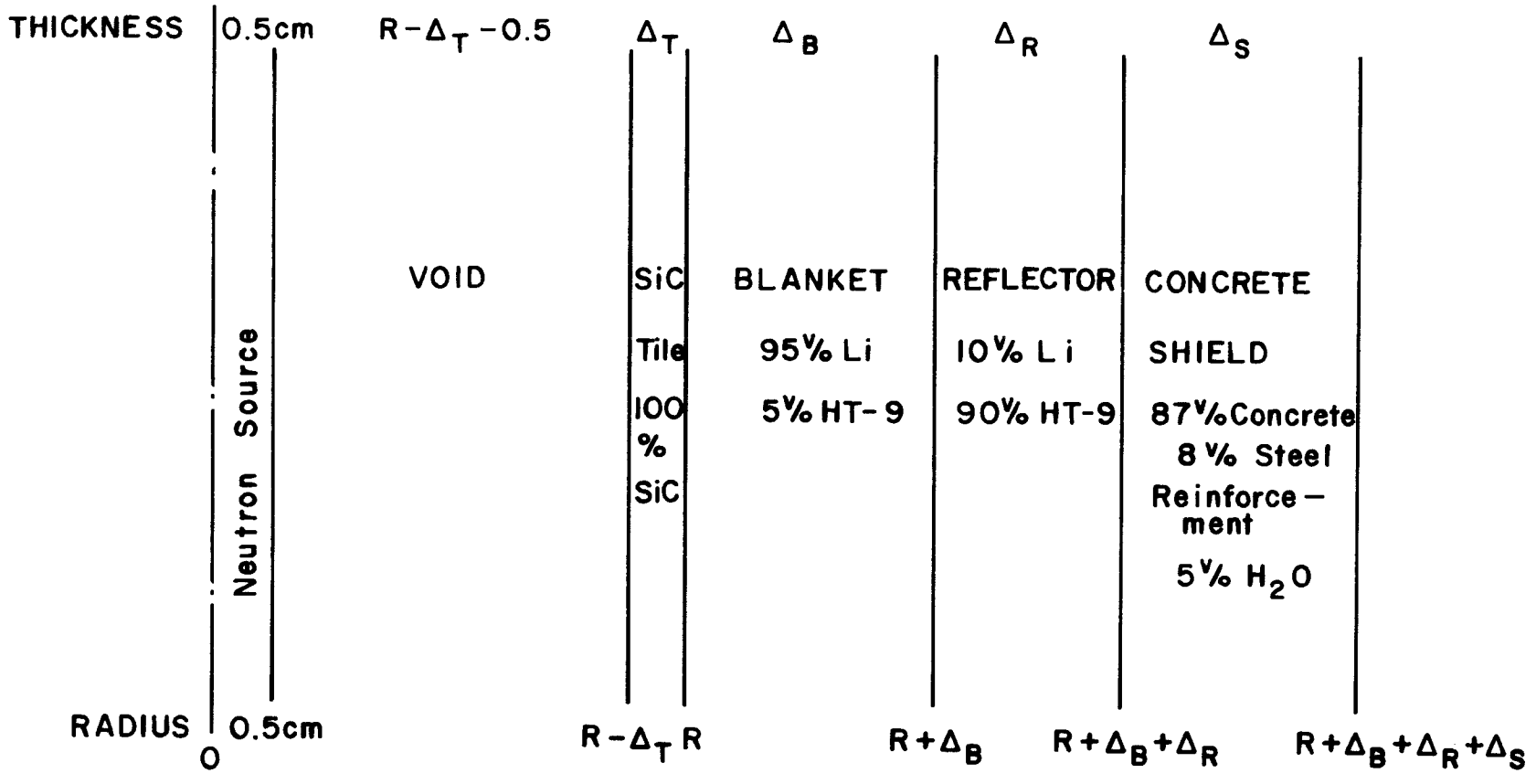

Fig. 4.3-2. A schematic of the geometrical model used in the calculations.

boundary condition at the back of the reflector. Dose calculations will be required in the future to determine the required shield thickness.

4.3.3 Neutronics Parametric Analysis

The blanket in the SIRIUS reactor is required to breed tritium and convert the kinetic energy of the fusion reaction into heat. The energy multiplication (M) should be as high as possible in a power reactor due to its impact on the cost of produced electricity. The energy multiplication is defined here as the energy deposited in the blanket and reflector divided by the fusion neutron energy incident on the blanket. Varying the design parameters results in different effects on both tritium breeding ratio (TBR) and M.[6] Increasing TBR usually results in decreasing M. Hence, the goal of the design is to obtain a TBR that exceeds unity by a small margin that accounts for any deficiencies and uncertainties in the calculational models and cross section data used and to allow for tritium losses and radioactive decay and supplying fuel for startup of other fusion reactors. A value of 1.1 is usually required from the three-dimensional calculations for fusion power reactor conceptual designs.[7,8] In this one-dimensional analysis we require a TBR $\gtrsim$ 1.14 to account for loss in tritium breeding due to neutron streaming into the laser beam ports. Another goal of the design is to reduce the radiation damage in the first metallic wall to values that eliminate the need for replacing the blanket during the reactor lifetime estimated to be 24 full power years (FPY). A lifetime dpa limit of 200 dpa is considered for HT-9.

In the preliminary design for the SIRIUS blanket, a separate SiC shell was used at a radius of 5 m while the first metallic wall of the blanket was located at a radius of 7 m. A series of one-dimensional neutronics calculations was made for this design to investigate the effects of the SiC shell

thickness, the blanket thickness, the reflector thickness and the lithium enrichment on TBR, M and the radiation damage to the first metallic wall and the SiC shell. The results are tabulated in Table 4.3-1.

The effect of the SiC shell thickness on the neutronics performance of the blanket is obtained by comparing the results of cases 1, 17, and 18. Damage levels in the first metallic wall obtained without SiC protection or with only a 2.5 cm thick SiC shell are not acceptable. Using a 5 cm thick SiC shell reduces the peak dpa in the blanket by ~ 26%. A slight increase in the peak dpa rate in C is observed as the SiC shell thickness increases. The reason is that the dpa cross section for C peaks in the low MeV region resulting in an increase in dpa in carbon as the spectrum softens. Increasing the SiC shell thickness results in decreasing both the TBR and M. The reduction in TBR is primarily due to the softening of the neutron spectrum incident on the blanket which results in a reduced $^{7}Li(n,n'\alpha)t$ reaction rate which has a threshold energy of ~ 2.86 MeV. In a liquid Li blanket this reaction plays a major role in tritium breeding because in addition to producing a triton it releases a low energy neutron that will be available for breeding tritium via the ^{6}Li $(n,\alpha)t$ reaction. The reduced energy multiplication results from the lower kerma factors for Si and C. Using a 5 cm thick SiC shell reduces TBR and M by ~ 20% and ~ 6%, respectively.

The effect of blanket and reflector thickness is given by comparing the results of cases 1-6. It is clear that the peak radiation damage in the SiC shell and the first wall is not affected by varying the blanket and reflector thickness. For a fixed reflector thickness, the TBR decreases as the blanket thickness decreases while M remains nearly unchanged. TBR decreases because of the reduced amount of breeding material in the blanket. On the other hand,

Table 4.3-1. Neutronics Characteristics for the SIRIUS Reactor with a SiC Shell at R = 5m and Inner Blanket Radius of 7m.

Case	% ^{6}Li	Δ_T(cm)	Δ_B(cm)	Δ_R(cm)	TBR	M	Peak Fe dpa/ 24 FPY	Peak C dpa/FPY
1	7.4	5	80	40	1.212	1.300	180	13.5
2	7.4	5	80	30	1.208	1.293	180	13.5
3	7.4	5	70	40	1.186	1.300	180	13.5
4	7.4	5	70	30	1.181	1.293	180	13.5
5	7.4	5	60	40	1.152	1.302	180	13.5
6	7.4	5	60	30	1.145	1.291	180	13.5
7	5	5	80	40	1.195	1.307	183	13.7
8	5	5	80	30	1.191	1.300	183	13.7
9	5	5	70	40	1.166	1.308	183	13.7
10	5	5	70	30	1.161	1.298	183	13.7
11	5	5	60	40	1.127	1.308	183	13.7
12	5	5	60	30	1.120	1.296	183	13.7
13	10	5	80	40	1.219	1.295	178	13.3
14	20	5	80	40	1.207	1.287	173	12.8
15	50	5	80	40	1.105	1.279	162	12.1
16	90	5	80	40	0.962	1.276	153	11.5
17	7.4	2.5	80	40	1.355	1.338	212	12.6
18	7.4	0	80	40	1.518	1.381	243	--

M does not change, even though the total blanket and reflector thickness decreases, due to the fact that a neutron absorbed in ^6Li releases ~ 4.8 MeV, while if it is absorbed in the structure of the reflector ~ 7 MeV is released. For a fixed blanket thickness, decreasing the reflector thickness results in a slight reduction ($\lesssim$ 1%) in both TBR and M due to the reduced amount of breeder and structure in the reflector.

In Table 4.3-1 results are given for cases with different lithium enrichments. Natural Li (7.4% ^6Li), depleted Li (5% ^6Li), and enriched Li (10, 20, 50, and 90% ^6Li) were considered. The effect of enrichment can be studied by comparing the results of cases 1, 7, 13, 14, 15, and 16. It is clear that as the ^6Li atom content increases, the peak damage rate in the SiC shell and the first metallic wall decreases. This is attributed to the large neutron absorption in ^6Li that results in reduced reflection from the blanket to the first wall and SiC shell. The TBR reaches a maximum at ~ 10% ^6Li and starts to decrease as the lithium is enriched further. The peak value is only ~ 0.6% larger than the value obtained with natural Li. This does not justify the extra cost of enriching the lithium. The variation of TBR with enrichment is attributed to the beneficial effect of the $^7Li(n,n'\alpha)t$ reaction that dominates tritium breeding at low enrichments. As the enrichment increases M decreases because of the increased neutron absorption in ^6Li that releases less energy than that released from absorption in the structure. However, this effect is relatively small with a gain of only ~ 0.5 % when depleted lithium is used. This does not justify the extra cost of depleting the lithium.

The results of Table 4.3-1 indicate that a TBR goal of ~ 1.145 can be achieved by different blanket designs. A natural Li 60 cm thick blanket followed by a 30 cm thick reflector, a depleted Li (5% ^6Li) 64 cm thick blanket

followed by a 40 cm thick reflector, and an enriched Li (35% ^{6}Li) 80 cm thick blanket followed by a 40 cm thick reflector are three of these possible designs. The energy multiplication for these three designs are 1.291, 1.308 and 1.283, respectively. The third design is discarded because of the large total blanket and reflector thickness (120 cm) and the smaller M. While the depleted Li design gives ~ 1.1% larger M than the natural Li case, the total thickness is ~ 15% larger. For this reason and because of the extra cost of depletion, case 6 was picked as a reference design.

Due to thermal considerations of limiting the temperature of the surface of the SiC tiles, the use of thinner SiC tiles at a larger radius was recommended. A series of neutronics calculations has been performed for a SIRIUS design in which a 2.5 cm thick protective SiC tile is used at the inner wall of the blanket located at a radius of 8 m. The results of these calculations are shown in Table 4.3-2. The results for the 7 m radius reference design are included for the purpose of comparison. For the same blanket and reflector thickness both TBR and M increase due to the reduced SiC tile thickness and the increased first wall radius that leads to more breeder and structure volume in the blanket and reflector. The peak damage rate in the SiC tile decreases because of the distance increase from the target from 5 to 8 m. The peak damage rate in the first metallic wall decreases since the effect of increasing the radius counterbalances the effect of decreasing the thickness of the SiC tiles. Since a TBR of 1.267 obtained in case 19 is much larger than the design goal, an attempt was made to reduce it by varying the blanket and reflector thicknesses. In case 20, the blanket thickness was reduced by 10 cm. This resulted in reducing the TBR by ~ 4.4% while M reduced slightly (~ 0.4%). The peak damage in the first wall and the SiC tiles increased

Table 4.3-2. Blanket Neutronics Characteristics for Different Designs with 8m First Wall Radius

Case	Rep. Rate (Hz)	R(m)	% ^{6}Li	Δ_T(cm)	Δ_B(cm)	Δ_R(cm)	TBR	M	Peak Fe dpa/ 24 FPY	Peak C dpa/FPY
6	7.5	7	7.4	5	60	30	1.145	1.29	180	13.5
19	7.5	8	7.4	2.5	60	30	1.267	1.33	160	7.25
20	7.5	8	7.4	2.5	50	30	1.212	1.32	160	7.31
21	7.5	8	7.4	2.5	45	35	1.182	1.33	161	7.37
22	7.5	8	7.4	2.5	40	40	1.147	1.33	161	7.43
23	5.5	8	7.4	1.25	40	40	1.172	1.35	128	5.72

slightly ($\lesssim$ 1%) due to the increased reflection from the reflector to the first wall and SiC tiles. In cases 21 and 22, the blanket and reflector thicknesses were changed keeping the total thickness fixed. Case 22 gives a TBR of 1.147 close to the design goal. The energy multiplication increased to 1.33 due to the larger space occupied by the metallic reflector. Thermal design considerations required decreasing the SiC tile thickness further to 1.25 cm with the repetition rate being reduced to 5.5 Hz. The volume fraction of structure in the blanket was increased to 8%. The neutronics results for this SIRIUS preconceptual point design, referred to as case 23, are given in Table 4.3-2. Comparing the results for cases 6 and 23, it is clear that besides satisfying the thermal requirements, changing the design from case 6 to case 23 has the attractive neutronics characteristics of achieving larger M and TBR with less total blanket and reflector thickness. Lower damage rates are obtained also in the SiC tiles and first metallic wall.

4.3.4 Neutronics Performance of the SIRIUS Preconceptual Point Design

A schematic of the SIRIUS preconceptual reactor design is given in Fig. 4.3-3. A summary of the tritium production results is given in Table 4.3-3. The overall tritium breeding ratio is 1.172. It is estimated that the TBR will be reduced by ~ 2.5% as a result of streaming into the laser beam ports. This will still leave an adequate margin to account for uncertainties in the calculational model and cross section data and to allow for tritium losses and radioactive decay and supplying fuel for the startup of other fusion reactors. The nuclear heating results are summarized in Table 4.3-4. The total energy recovered from the SiC tiles, the blanket and the reflector is 16.88 MeV per source neutron from the target. Since the neutrons emitted from the target have an average energy of 12.5 MeV, this corresponds to an energy multipli-

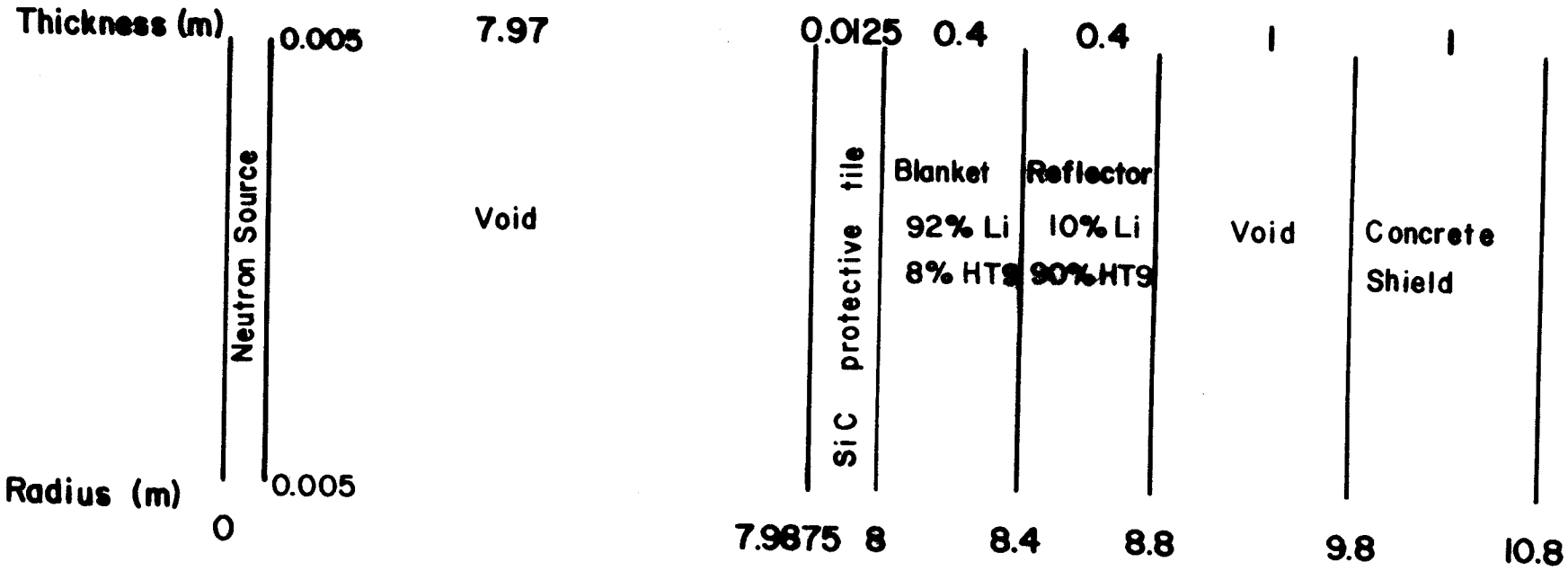

Fig. 4.3-3. A schematic of the SIRIUS preconceptual reactor design.

Table 4.3-3. Tritium Production (Tritons/Source Neutron)

	$^{6}Li(n,\alpha)t$	$^{7}Li(n,n'\alpha)t$	Total
Blanket	0.721	0.365	1.086
Reflector	0.083	0.003	0.086
Total	0.805	0.367	1.172

Table 4.3-4. Nuclear Heating (MeV/Source Neutron)

	Neutron	Gamma	Total
SiC Tile	0.61	0.30	0.91
Blanket	9.74	2.50	12.24
Reflector	0.92	2.81	3.73
Shield	0.02	0.21	0.23
Total	11.29	5.82	17.11

cation of 1.35. For a 100 MJ neutron target yield per shot and a repetition rate of 5.5 Hz, this corresponds to a total blanket power from nuclear heating of 744 MW. Adding the energy carried by the x-rays (8 MJ yield) and the ion debris (26 MJ yield) which is deposited in the SiC tile, we get a total thermal power of 931 MW. When the effects of neutron loss out the beam tubes are considered the total thermal power becomes 913 MW. The unrecovered power in the shield is only 9.8 MW which represents only ~ 1% of the total thermal power. The spatial variation of power density in the SiC tile, blanket, and reflector is shown in Fig. 4.3-4. The neutron wall loading at the SiC tile is 0.93 MW/m^2. The peak power density in the SiC tile is 4.1 W/cm^3. The power density in the first metallic wall is 5.1 W/cm^3. The peak power density in the reflector is 1.6 W/cm^3. While ~ 75% of nuclear heating in the reflector comes from gamma heating, only ~ 20% of the total heating in the blanket comes from gamma heating.

Figure 4.3-5 gives the spatial variation of displacement damage (dpa) and helium production in the SiC protective tile. Because of the relatively large threshold energy for the (n,α) reaction, the helium production rate has a steeper spatial variation than the dpa rate. The dpa rate drops from a peak of 5.75 dpa/FPY at the front to a value of 5.56 dpa/FPY at the back. On the other hand, the helium production rate drops from 536 to 477 He appm/FPY. The spatial variation of the dpa rate and helium production in the HT-9 structure of the blanket and reflector is shown in Fig. 4.3-6. Again the helium production rate drops faster than the dpa rate as one moves towards the back of the reflector. Steeper spatial variation is obtained in the reflector than in the blanket because of the effective neutron slowing down via the inelastic interaction in the structure. The peak dpa rates in the structure of the blanket

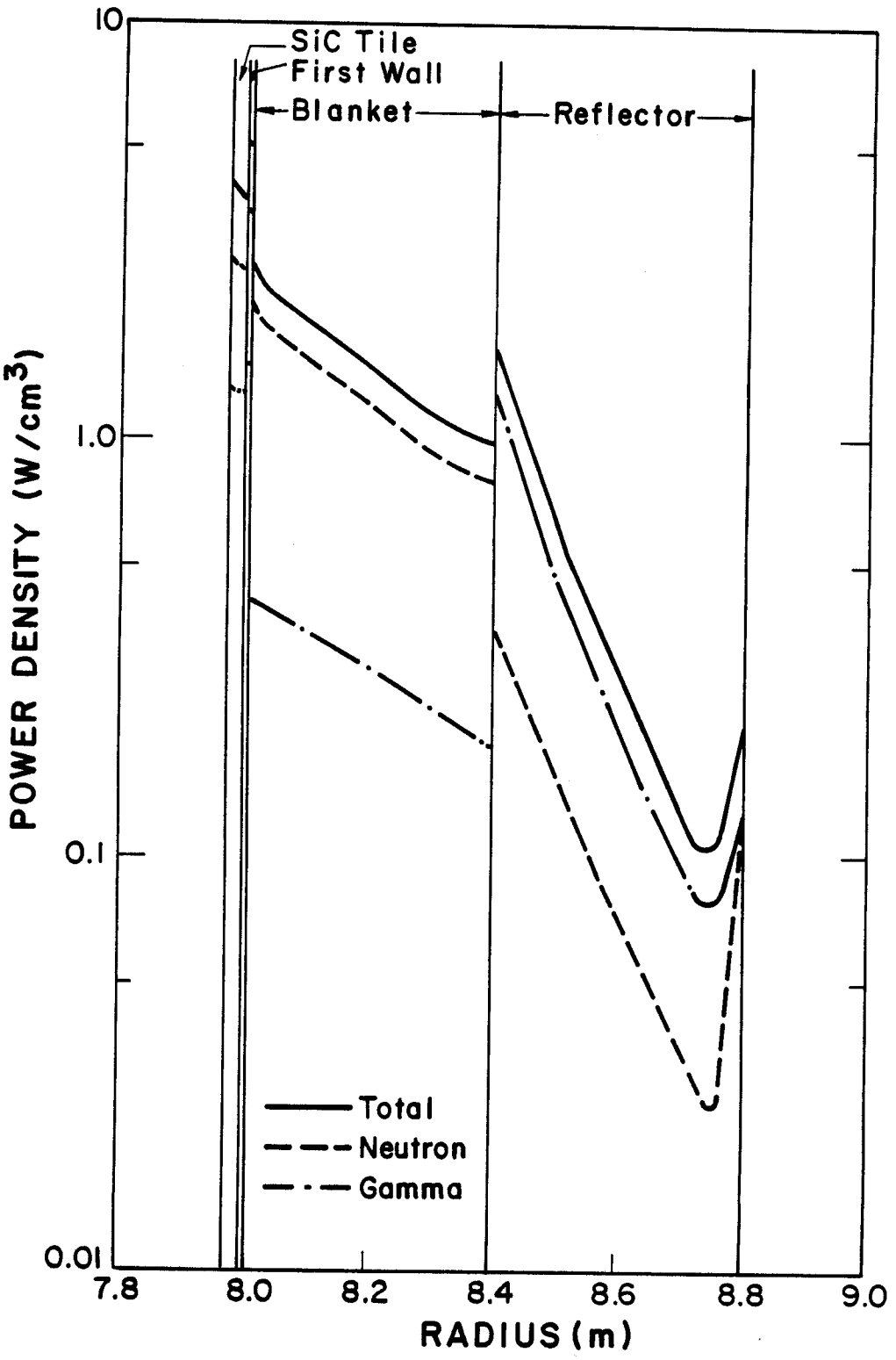

Fig. 4.3-4. Spatial variation of power density in the SIRIUS reactor.

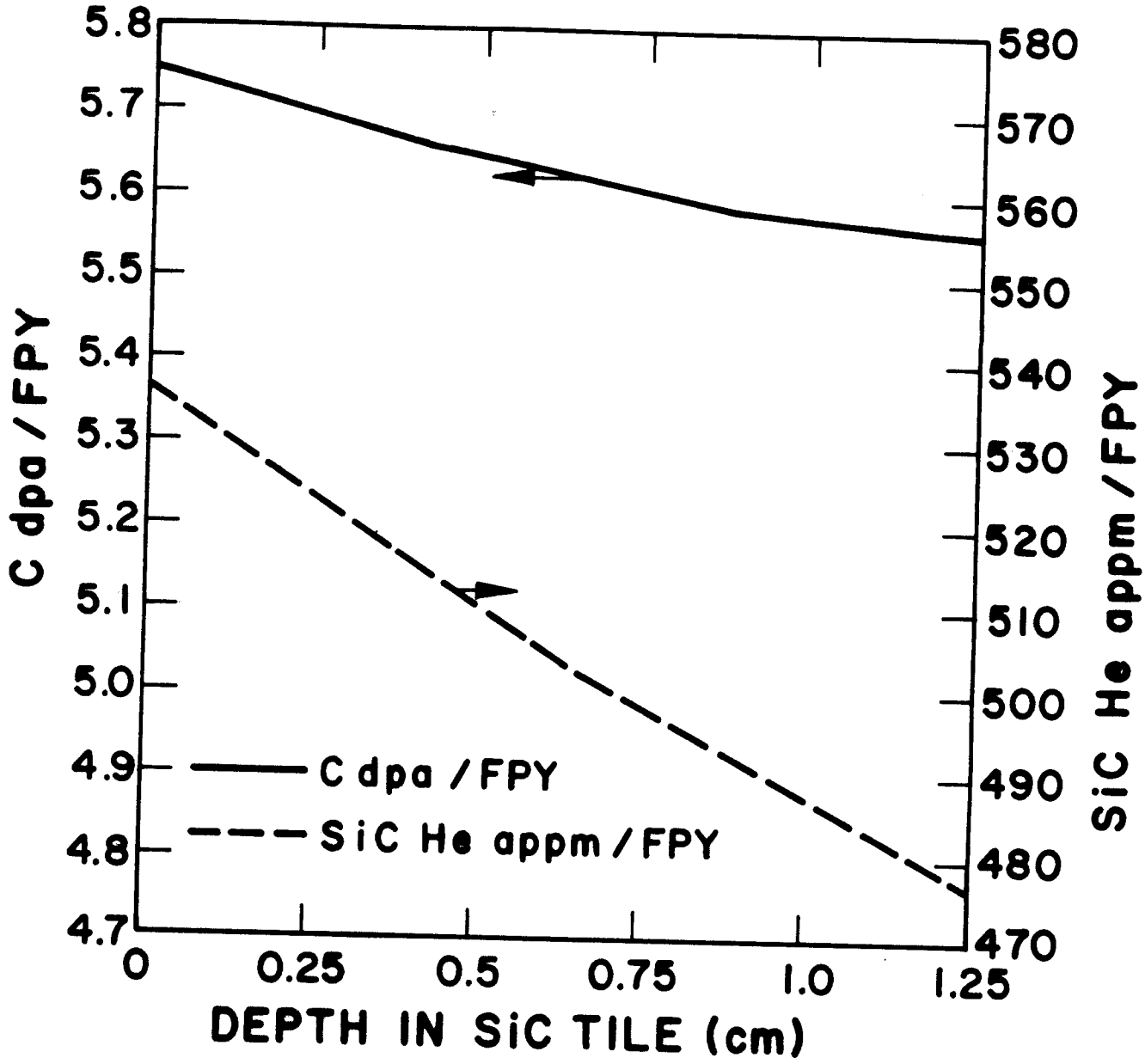

Fig. 4.3-5. Spatial variation of damage rate in the SiC tile.

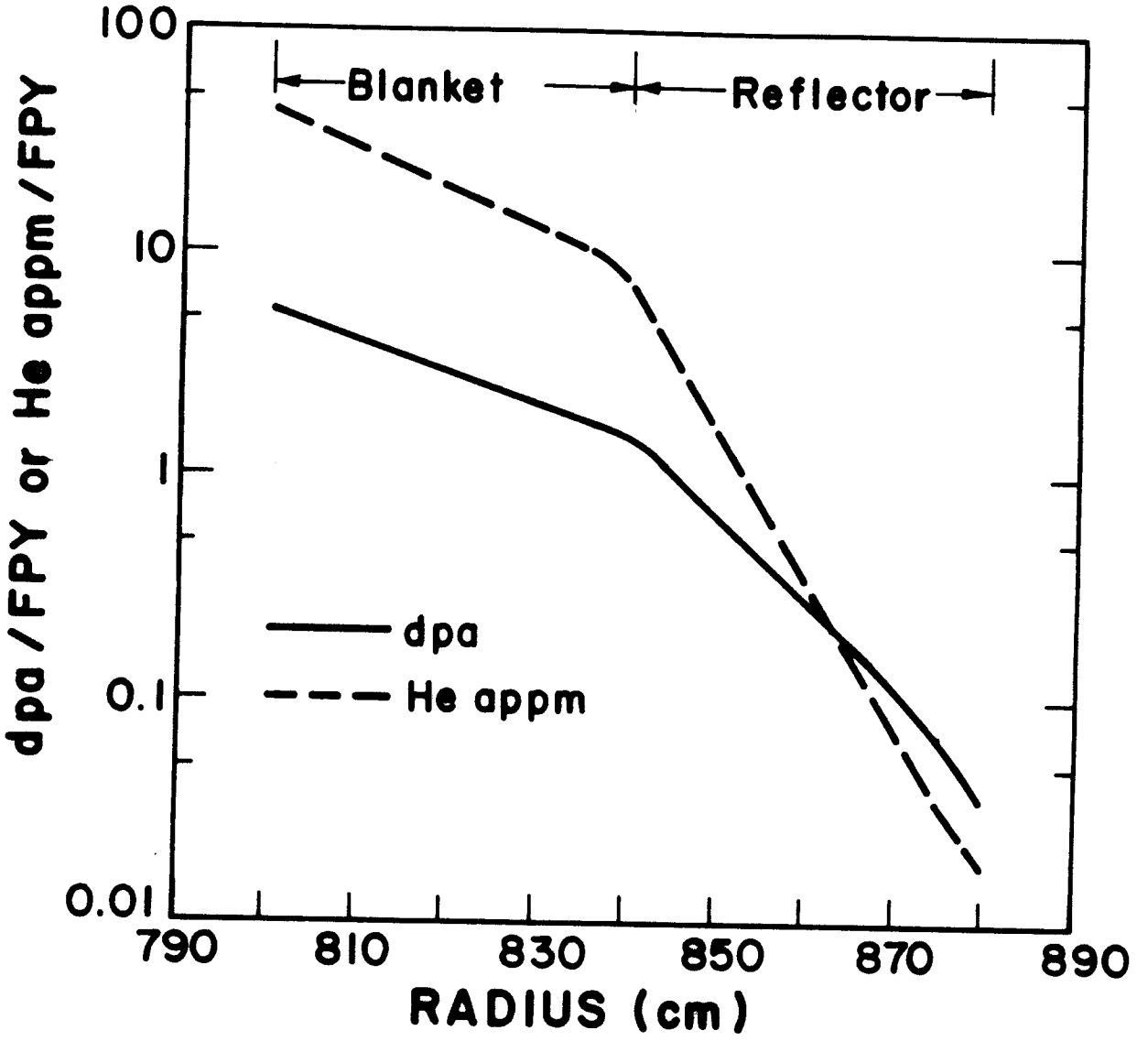

Fig. 4.3-6. Spatial variation of damage rate in the HT-9 structure of the blanket and reflector.

and reflector are 5.35 and 1.45 dpa/FPY, respectively. The peak He production rates in the structure of the blanket and reflector are 43 and 7 He appm/FPY, respectively. The peak accumulated dpa and helium production after 24 FPY of operation are 128 dpa and 1032 He appm, respectively. These damage levels allow the blanket to remain in the reactor for the whole reactor lifetime.

References for Section 4.3

1. W.R. Meier, "Neutron Leakage Through Fusion Chamber Ports: A Comparison of Lithium and Lead-Lithium Blankets," Nucl. Tech/Fusion, 3, 385 (1983).

2. J. Hovingh, "Design Considerations for Direct-Illumination-Driven Inertial Fusion Reactors," Nucl. Tech/Fusion, 4/2, 973 (1983).

3. "ANSIN-ORNL," RSIC Code Package CCC-254, Radiation Shielding Information Center, Oak Ridge National Laboratory (1979).

4. "VITAMIN-C, 171 Neutron, 36 Gamma-Ray Group Cross Section Library in AMPX Interface Format for Fusion Neutronics Studies," DLC-41, RSIC Data Library, Oak Ridge National Laboratory (1979).

5. "MACKLIB-IV-82, 171 Neutron, 36 Gamma-Ray Group Kerma Factor Library," DLC-60B, RSIC Data Library, Oak Ridge National Laboratory (1982).

6. M.E. Sawan and J.H. Huang, "The Tritium Breeding-Energy Multiplication (T-M) Plot for Fusion Blanket Design," Trans. Am. Nucl. Soc., 44, 146 (1982).

7. B.G. Logan et al., "Mirror Advanced Reactor Study Final Report," Lawrence Livermore National Laboratory, UCRL-53333-83 (1983).

8. B. Badger et al., "HIBALL - A Conceptual Heavy Ion Beam Driven Fusion Reactor Study," Univ. of Wisconsin Fusion Engineering Program Report UWFDM-450 (1981).

4.4 Thermal Response of First Wall

The cavity design described in previous sections will be analyzed here in regard to its thermal response to surface and volumetric energy deposition. This energy deposition is caused by incident radiation in the form of ion debris and x-rays (short penetration distances -- i.e., surface deposition), as well as gamma rays and neutrons (long penetration distances -- i.e., volumetric deposition). The design limit for the cavity and the silicon-carbide protective tiles (SiC tiles) is expressed in terms of a maximum operating temperature for the cavity first wall (500°C or 773 K) and a damage limit for the SiC tiles (less than 2800°C or 3073 K). These temperature limits reflect material limits placed on the cavity wall for strength and on the SiC tiles for resistance to decomposition.

Since the reactor cavity is spherical in shape with a radius much larger than its thickness we can represent the SiC tiles as a one-dimensional slab (see Fig. 4.4-1). In addition the pressure inside the cavity is sufficiently low that convective heat transfer can be neglected and the main mechanisms for heat transfer for the energy deposited would be conduction through the SiC tile and radiation to the cavity wall. In this simple quasi-steady state analysis we have assumed:

(1) SiC thermophysical properties are constant,

(2) Surface emissivities of the SiC tile and cavity wall are known,

(3) Conduction heat transfer through structural supports from the SiC tile to the cavity wall is negligible,

(4) The energy deposition from ion debris and x-rays is treated together by using one single averaged attenuation coefficient,

Fig. 4.4-1

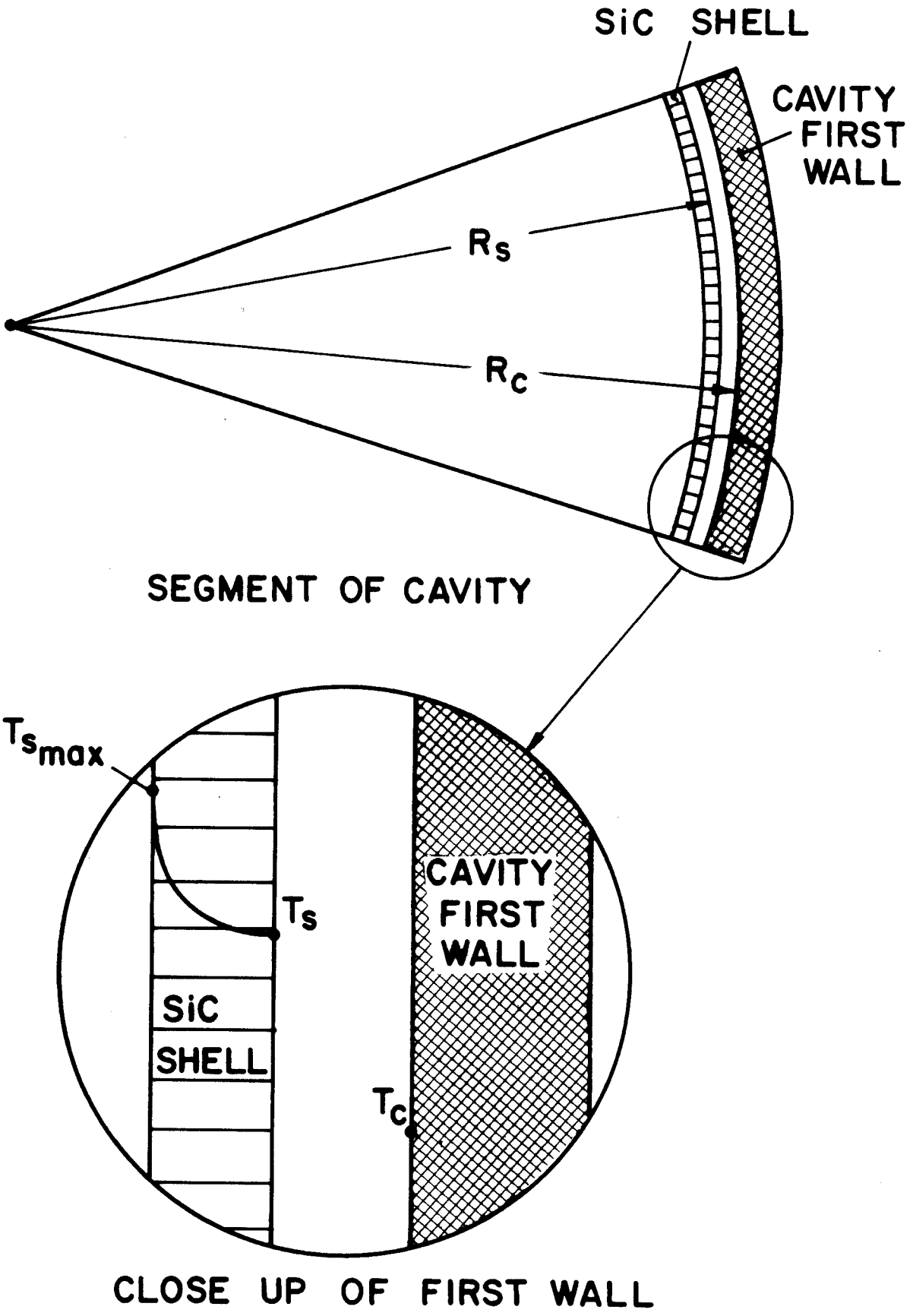
SiC SHELL
CAVITY FIRST WALL
R_s
R_c
SEGMENT OF CAVITY
$T_{s_{max}}$
T_s
SiC SHELL
CAVITY FIRST WALL
T_c
CLOSE UP OF FIRST WALL

(5) The energy deposition from gamma rays and neutrons is modeled as a volumetric energy generation rate with an averaged source strength.

The first and second assumptions are used in these design calculations because it is recognized that we are only looking for the approximate design values which satisfy the thermal limits. Any detailed calculations will take into account the temperature dependent nature of these properties. The third assumption seems quite reasonable because the SiC tile structure will be thin-walled and easily supported by a thin ribbed structure. Conduction heat transfer through this support structure will not be substantial. The final two assumptions will be discussed later.

If one fixes the cavity wall temperature (T_c = 500°C), then one can calculate the maximum inner surface temperature of the SiC slab by the relation

$$T_{s\ max} = T_c + \Delta T_{rad} + \Delta T_{vol} + \Delta T_{surf} \qquad (4.4\text{-}1)$$

where: ΔT_{rad} is the temperature rises across the cavity-SiC tile gap

ΔT_{vol} is the temperature rise in the SiC tile due to volumetric energy deposition

ΔT_{surf} is the temperature rise in the SiC tile due to surface energy deposition.

One can add the temperature rise across the SiC tile in such a simple way because the energy balance for the SiC is linear for our constant property case.

The temperature rise across the gap between the SiC tile and the cavity wall is given by[1]

$$q = \frac{A_s \sigma (T_s^4 - T_c^4)}{\frac{1 - \varepsilon_s}{\varepsilon_s} + 1 + \left(\frac{1 - \varepsilon_c}{\varepsilon_c}\right) \frac{A_s}{A_c}} \qquad (4.4\text{-}2)$$

where: q is the total power transferred

A is the surface area of the cavity, c, and shell, s, respectively

$= (4\pi R^2)$

ε is the emissivity of each surface

and $T_s - T_c \equiv \Delta T_{rad}$.

The temperature rise in the SiC tile due to volumetric energy deposition can be calculated from a simple one-dimensional energy balance to be

$$\Delta T_{vol} = \frac{q''' L_s^2}{k_s} \qquad (4.4\text{-}3)$$

where: q''' is the average volumetric energy deposition rate

L_s is the SiC tile thickness

k_s is the SiC thermal conductivity.

The volumetric energy generation rate was averaged based on the spatially dependent neutronic calculations. These neutronic calculations indicated that the thin SiC tiles absorbed energy from the neutron and gamma ray flux with an attenuation coefficient of 0.0425 cm^{-1} (i.e., a characteristic length of 23 cm). This low attenuation coefficient indicates that the volumetric heating is fairly uniform (±15% deviation from the average) and substantiates the assumption stated previously.

The temperature rise due to surface energy deposition is a complex function of the frequency of the power deposited[2] and the attenuation coefficient of the SiC shell to ion debris and x-rays.[3] Based on related work done for a conceptual design of a laser driven ICF reactor, SOLASE,[3] one can

calculate the temperature rise due to surface deposition in a relatively straightforward manner. One need only specify the surface energy flux, the pellet repetition rate, the SiC tile properties and the attenuation coefficient of SiC for these particles. Separate calculations indicated that the energy averaged attenuation coefficient for ion debris and x-rays was approximately 1.3×10^8 cm^{-1}. This indicates that this volumetric energy source closely resembles a high surface energy deposition (34 MJ per event).

The results of these calculations are given for selected design parameters in Table 4.4-1. The table illustrates the results for two specific geometries. In the first case the SiC tiles are considered to be at a position of 5 meters with the cavity wall at a radius of 7 meters. This represents the original cavity design where the SiC tiles were considered to be a separate structure within the cavity. The second design represents the case of the SiC tiles as a protective layer directly on the cavity wall. This design has the effect of decreasing the energy flux deposited on the tiles with a slight increase in the overall cavity radius.

From a thermal design limit viewpoint the first design is not feasible unless one reduces the SiC tile thickness significantly and decreases the pellet repetition rate below 3.5 s^{-1}. It is not desirable to reduce either of these two parameters to these values for a number of reasons: (1) at this radius a thinner SiC tile will reduce its neutron shielding capability and thereby cause the radiation damage on the first wall to increase significantly; (2) the thinner tile will be much more difficult to structurally support as a separate integral structure; and (3) a large reduction in the repetition rate will significantly reduce the reactor power output.

Table 4.4-1. SiC Tile Surface Temperatures for Selected Design Parameters*

R_s (m)	R_c (m)	L_s (mm)	r_p (s^{-1})	T_s (K)	ΔT_{vol} (K)	ΔT_{surf} (K)	$T_{s_{max}}$ (K)
5	7	50	7.5	2348	1620	18790	22758
5	7	25	7.5	2220	405	9395	12020
5	7	12.5	7.5	2148	101	4697	6946
5	7	50	3.5	1947	756	8769	11472
5	7	25	3.5	1835	189	4384	6408
5	7	12.5	3.5	1775	47	2192	4014
7.95	8	50	7.5	1788	384	7355	9527
7.975	8	25	7.5	1721	96	3678	5495
† 7.9875	8	12.5	7.5	1685	24	1839	3548
7.975	8	25	5.5	1586	70	2697	4353
7.9875	8	12.5	5.5	1554	18	1348	2920
7.95	8	50	5.0	1616	256	4903	6775
7.975	8	25	5.0	1549	64	2452	4065
† 7.9875	8	12.5	5.0	1517	16	1226	2759

*Properties used in these calculations:

SiC surface emissivity = 0.8
SiC thermal conductivity = 17 W/m K
SiC specific heat = 1255 J/kg K
SiC theoretical density = 3000 kg/m^3
SiC attenuation coefficient = 1.3 (10^8) cm^{-1}

†Design parameters which satisfy thermal limits.

The latter cavity design although larger in overall size has the advantage of maintaining a SiC tile which is thick enough (12.5 mm) to reduce the radiation damage to the cavity first wall (i.e., below 200 dpa). Also it successfully serves its second function of absorbing the ion/x-ray surface energy flux without exceeding thermal limits for a repetition rate of 5.5 s^{-1} or below. Finally, it may be structurally simpler to build since it is more of a protective "tile" on the cavity wall rather than a separate integral structure. Therefore, from the perspective of meeting the thermal design limit the latter design seems more feasible.

References for Section 4.4

1. F. Kreith, Fundamentals of Heat Transfer, McGraw-Hill Pub., New York (1970).

2. H.S. Carslaw, C. Jaeger, Conduction of Heat in Solids, Oxford Univ. Press, London (1961).

3. B. Badger et al., "SOLASE - A Laser Fusion Reactor Study," University of Wisconsin Fusion Engineering Program Report UWFDM-220 (1978).

4.5 Mechanical Design Considerations

4.5.1 General Discussion

Various schemes for ICF first wall and blanket structure protection were discussed in Chapter 3. These schemes were proposed in past reactor designs and were intended primarily for non-uniform illumination. A cursory look at these schemes indicated that two of them appeared to have the greatest potential for use in a uniformly illuminated reactor cavity, namely the buffer gas and the large cavity schemes. It was pointed out that a good combination would be the use of size to take advantage of the $\frac{1}{R^2}$ factor, and a ceramic surface protection, to take advantage of the high temperature properties of materials such as graphite or SiC. In this section we describe the mechanical aspects of a uniformly illuminated ICF reactor cavity utilizing such a first wall protection scheme.

The reactor cavity, a cross section of which is shown in Fig. 4.5-1, is spherical, nominally 8 m in radius and consists of the following radial build:

1. 1.25 cm thick SiC protective tiles, 100% of theoretical density.
2. 10 cm space.
3. 40 cm thick blanket made of the ferritic steel HT-9 cooled with elemental lithium. Volumetric composition is 5% structure, 95% lithium.
4. 40 cm thick reflector consisting of 90% HT-9 structure and 10% elemental lithium coolant.
5. 100 cm thick space.
6. 100 cm thick concrete shield.

The cavity is illuminated with 32 beams equidistantly distributed around the sphere as shown in Fig. 4.5-2. The beam distribution is based on a twenty sided icosahedron, where the sides are equilateral triangles superimposed on

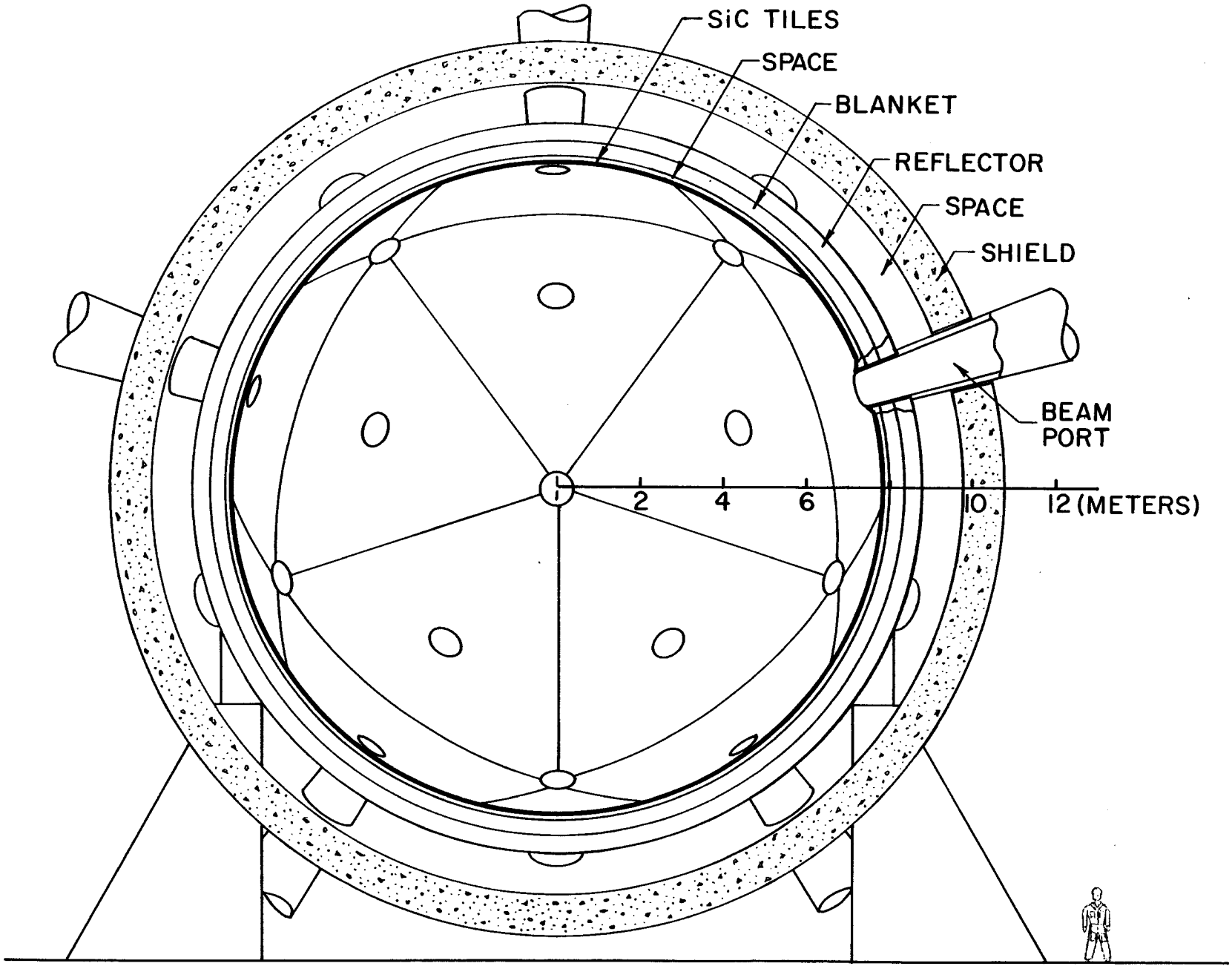

Fig. 4.5-1

CROSS SECTION OF SIRIUS CHAMBER

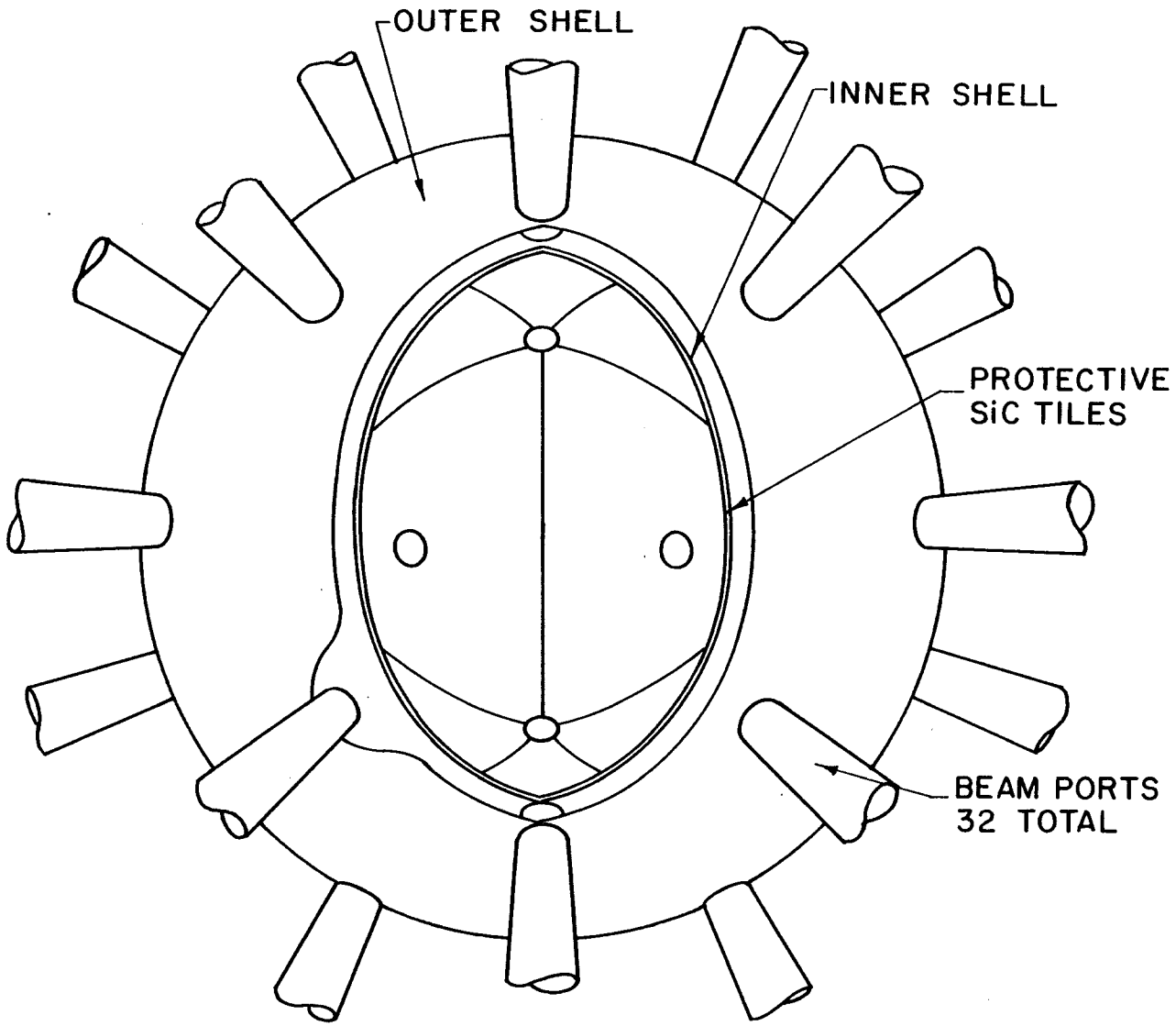

ISOMETRIC VIEW OF SIRIUS CHAMBER WITH CUTAWAY

Fig. 4.5-2

a spherical surface. The thirty two equidistant points on the sphere come from the centers of each triangle (20) plus the vertices where the triangles meet (12).

The essence of this cavity design can be summed up in two statements:

1. The SiC tiles protect the blanket first wall from the cyclic high heat flux and are designed to be replaced on a regular schedule.
2. The blanket, reflector and shield are designed to withstand the nuclear radiation environment without replacement for the reactor lifetime.

In the next sections, the different parts of the cavity will be discussed from the mechanical standpoint.

4.5.2 SiC Protective Tiles

The primary function of the tiles is to absorb on their front side, the high short pulsed heat load from target generated x-rays and ion debris and radiate it over a much longer pulse from the back side to the actively cooled front surface of the blanket. In this way, they act as a thermal capacitor which reduces a highly cyclic source of heat to an approximately steady state source. Eventually, the surface of the tiles will be eroded away by the target x-rays and energetic ions. The eroded material will redeposit itself both on the tiles and other cooled surfaces such as the beam ports. For this reason, and because they will sustain radiation damage, the tiles will have to be replaced periodically on a yet to be determined schedule. The blanket itself, however, is spared from the sputtering of the ions and because of the reduced neutron induced radiation damage can survive the lifetime of the reactor.

The tiles are made of sintered SiC in the shape of equilateral triangles which conform to a spherical contour. One beam port is located in the center

of the triangle, and the vertices of each triangle subtend one-fifth of the circumference of each of the three beam ports at the vertices. This can be clearly seen in Fig. 4.3-1 in which a cross section is taken at a plane which does not intersect any beam ports. The beam port in the center of the cavity is one of the 12 beam ports where the vertices of the triangles meet.

The length of the triangle side along the spherical arc is 8.63 m and the surface area of each triangle exclusive of beam ports is 37.94 m^2. Each tile is supported at the center only. It is, therefore, unrestrained at any other point and in this sense will not have high thermal stresses. The tile support consists of a SiC sleeve which fits into the beam port up to a certain distance. One possible attachment scheme is shown in Fig. 4.5-3. The outside of the collar has a reverse conical configuration from the beam tube itself, thus making insertion from the inside of the cavity possible. Some type of locking mechanism on the collar can be envisaged to anchor the tile to the beam port along with slots which give it the proper orientation within the cavity for that particular beam port. It is not difficult to imagine that all the tiles can be identical to the minutest detail and are interchangeable as long as the guide slots in the beam ports are properly located. This support scheme extends the SiC surface into the beam ports which will also receive a high surface heat load. It is cooled in the same way as the tile, by radiating to the support structure behind it.

A brief look at the bending stresses on the support collar shows that they are trivial compared with the bending stresses on the tiles themselves. We take the worst case for the support collar where the tile is in a vertical orientation. For a 1.25 cm thick 100% density factor tile weighing 1.5 tonnes, supported on a 75 cm ID collar with a wall thickness of 2.5 cm, the

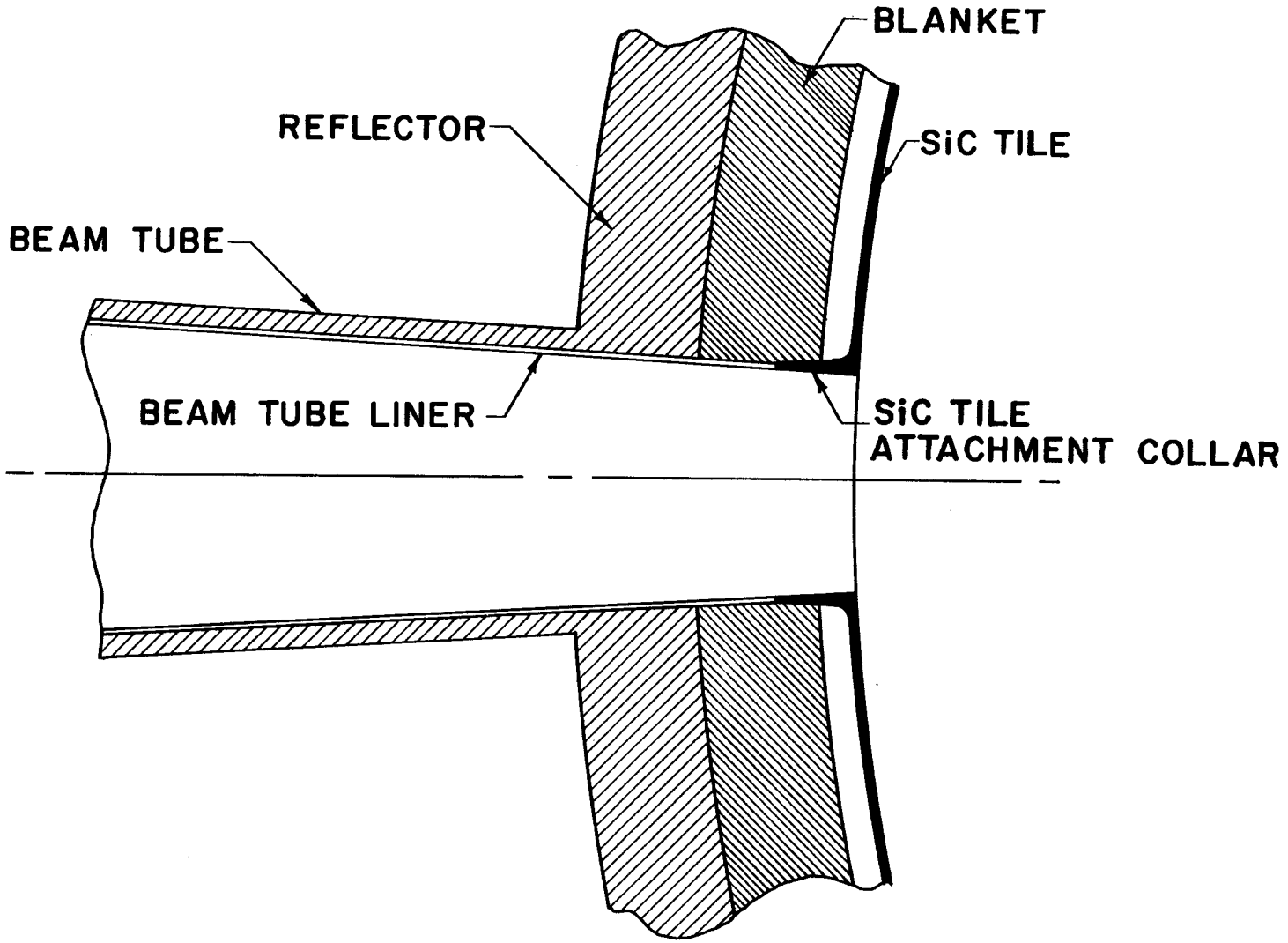

PROPOSED TILE ATTACHMENT SCHEME

Fig. 4.5-3

Table 4.5-1. Parameters of Protective Tiles

Material	SiC
No. of tiles in the cavity	20
Shape of tiles	Equil. triangular
Thickness of tiles, cm	1.25
Dimension of side, m	8.63
Area of Tile, m^2	37.9
Max. operating temp. °C	2650
Max. support stress, MPa	55
Mass of one tile, tonnes	1.5

maximum bending stress is 0.16 MPa. On the other hand, a horizontal tile of the same thickness will have a bending stress of ~ 55 MPa due to the cantilevered part if no credit is taken for stiffening coming from the spherical shape. This too, however, is a low stress, even at the high operating temperature. Table 4.5-1 gives the parameters of the protective tiles.

4.5.3 Blanket Design

The blanket for SIRIUS is shown in Fig. 4.5-1 as a continuous spherical shell penetrated by 32 beam ports. It is 40 cm thick with a volumetric fraction of 5% structure and filled with elemental lithium.

The vacuum boundary in the reactor chamber is the reflector, thus the only load the blanket experiences is that of its own weight and the weight of the Li. It will be evacuated on both sides and will not experience a collapsing pressure. On the other hand, the Li will be pumped under pressure and thus the blanket will be subjected to internal pressure.

The blanket is envisaged as being two concentric spherical shells, 40 cm apart, with 32 uniformly distributed port holes radiating outward from the center of the sphere. Tubes welded to both inner and outer shells within the ports seal the ports and also provide reinforcing to the blanket. There will have to be an access door in the cavity which is required for replacement of tiles during routine maintenance. This access door is envisaged as a triangular segment of the blanket shell attached to a slightly larger triangular segment of the reflector. Flanges on the reflector segment provide the vacuum seal for the chamber. It appears that four beam ports will be included in the access door. As the door is opened, a single tile will come out with it. This provides enough space for a remote handling machine to operate within the chamber.

The lithium flow pattern in the blanket has not been analyzed, but there are many possible ways for achieving a good flow distribution. Since there are no magnetic fields to deal with, pumping the Li at a high velocity should not present problems. Clearly baffles and orifices will have to be provided, and the blanket divided into appropriate segments to be fed by supply and return headers.

The blanket has not been stress analyzed as a separate entity. It is assumed that the reflector, which is also 40 cm thick with 90% steel constituent, can provide the structural strength needed to support the blanket. Obviously the coupling between the blanket and the reflector will have to be carefully analyzed.

4.5.4 Reflector

The reflector plays an important part in the SIRIUS chamber. Aside from its important neutronic function, it also provides the vacuum boundary for the

reaction chamber as well as the support of the blanket.

The reflector is 40 cm thick, made of HT-9 steel and is cooled with a 10% volumetric fraction of elemental lithium. It is spherical and has 32 beam ports penetrating it. The beam ports have tubes welded to them which extend through the shield and on to the final mirrors. Immediately outside the shield, a set of cryopumps are situated off to the side of each beam tube. These pumps maintain the chamber vacuum at the prescribed value.

The mass of the reflector structure is 2590 tonnes. It is rather large and awkward to handle; however, nuclear reactor pressure vessels are comparable in size and weight.

As mentioned earlier, a triangular access door will be provided in the reflector as part of the maintenance scheme for the protective tiles.

Table 4.5-2 gives some physical parameters of the blanket and reflector.

4.5.5 Maintenance

Although the blanket, reflector and shield are designed for the reactor lifetime, the SiC protective tiles will have to be changed out due to vaporization, sputtering and radiation damage. For this reason access must be provided into the reaction chamber.

The maintenance scheme envisaged for the SIRIUS chamber depends on the ability to replace the protective tiles from inside of the chamber. As described earlier, the tiles are designed to be supported in the center on a collar which fits into a beam port (see Fig. 4.5-3). The tiles are identical and completely interchangeable. This is significant in the manufacture of the tiles. Each beam port will have a unique pattern of guide slots which will act to orient the tile for that particular beam port. A locking mechanism

Table 4.5-2. Some Physical Parameters of Blanket and Reflector

Blanket shape	Spherical
Blanket inner radius, m	8.0
Blanket outer radius, m	8.4
Structural fraction, %	5
Structural material	HT-9
Mass of structure, tonnes	131
Mass of lithium, tonnes	168
Reflector shape	Spherical
Reflector inner radius, m	8.4
Reflector outer radius, m	8.8
Structural fraction, %	90
Structural material	HT-9
Mass of structure, tonnes	2590
Mass of lithium, tonnes	19.5

secures the tile to the beam port. This mechanism can be activated mechanically from inside the collar for unlocking and removing of the tile.

Before a tile replacement operation can be started there are many tasks that have to be executed simply to provide access to the chamber. We envisage that access would be provided from one side of the chamber, rather than from the top or bottom. Four beam ports will be affected, which means that the four beam tubes leading from the back of the shield to the final focussing mirror will have to be dismantled and removed out of the way. Before the

access door in the shield can be opened, the connecting beam tubes leading up to the back of the reflector have to be disconnected and removed. Such an operation can actually be conducted from the inside of the beam tube. A cutting head is inserted into the beam tube which machines a seal weld and disconnects the tube. This now makes it possible to unfasten and remove a triangular access door in the shield.

At this point the back of the reflector is exposed, revealing the coolant connections. The coolant connection to the access door in the reflector/ blanket must be undone and the vacuum seal on the reflector access door has to be machined off. As the reflector/blanket access door is removed, a single tile attached to it comes out as well.

The large opening thus provided will allow a sizeable remotely manipulated boom to be inserted and indexed to reference points within the chamber. The boom can now rotate and twist within the chamber with three degrees of freedom in order to reach each of the remaining tiles. Once the boom grabs a tile by inserting a tool into the attachment beam port, it activates the locking mechanism and removes the tile. As the tiles are accumulated, they can be taken out of the chamber by retracting the boom.

Tile replacement is done the same way in a reverse sequence. The last tile goes into place when the access door in the reflector/blanket is closed and sealed. Reconnecting the coolant lines, replacing the shield access door and rebuilding the beam tubes completes the tile replacement process.

4.6 Radiation Damage to the Final Mirrors

4.6.1 Introduction and Radiation Environment

The choice of a KrF laser, whose wavelength is 0.248 microns, for SIRIUS will rule out the use of a metallic final mirror. This can be easily seen from Fig. 4.6-1 where the reflectance of various metal films is plotted versus the wavelength of the incident light. Typically reflectances of > 99% are required so as not to overheat the mirror. Figure 4.6-1 shows that Rh and Al fall below the required reflectance at wavelengths above 1 micron whereas Cu and Au fail the reflectance criteria below 0.7 microns. The acceptable wavelength range can be extended to about 0.4 microns with the use of Ag but at 0.248 microns even the reflectance of Ag falls to approximatley 30%. The conclusion one is then faced with is that highly reflecting (HR) coatings will be required for the final mirrors in SIRIUS.

The environment that these mirrors will experience is given in Table 4.6-1. We have assumed that the HR coating in a series of Al_2O_3/SiO_2 layers on an Al substrate. The damage threshold for this material is 5 J/cm^2 (see Chapter 2). The 14 MeV uncollided neutron fluence to the final mirrors some 21 meters away is 1.6×10^{20} cm^{-2} per full power year (FPY) of operation. This would correspond to roughly 3×10^{11} rads per full power year.

The charged particle damage and x-rays could correspond to very high radiation damage levels if they are not stopped. Fortunately, gas windows (basically a small amount of gas, a few torr-meters, flowing in front of the mirror) can completely stop such radiation from reaching the mirror. While such a window has not been designed for SIRIUS, previous studies such as SOLASE showed such windows are possible.

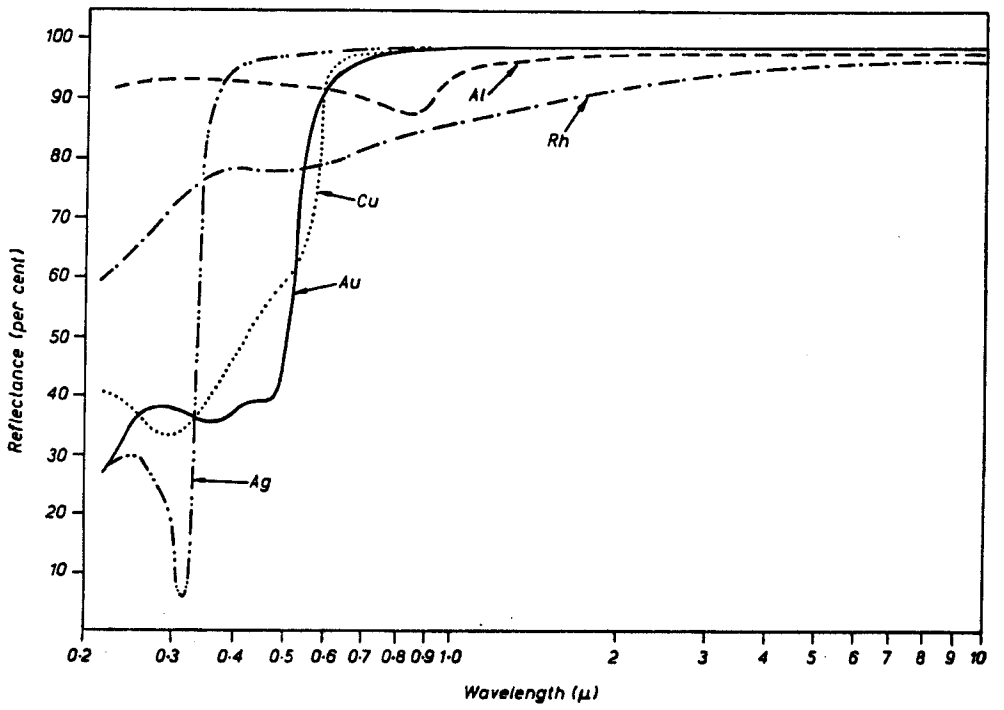

Fig. 4.6-1. Reflectance of freshly deposited films of aluminum, copper, gold, rhodium and silver as a function of wavelength from 0.2-10 μ.

Table 4.6-1. SIRIUS Last Mirror Parameters

Substrate material	Al
HR coating materials	Al_2O_3/SiO_2
Assumed laser damage threshold	5 J/cm^2
Distance to cavity center	21 m
Mirror diameter	2.1 m
Repetition rate	5.5/sec
DPA/FPY in Al	< 0.5
Charged particle energy density*	8.11×10^7 J/cm^2/FPY
X-ray energy density*	2.49×10^7 J/cm^2/FPY
14 MeV neutron fluence on coatings	1.6×10^{20} n/cm^2/FPY
Radiation dose to HR coatings	3×10^{11} rads/FPY

*It may be possible to stop this radiation by flowing a dilute (1 torr-m) gas in front of the mirror.

4.6.2 HR Coatings[1]

A simple HR coating is composed of a stack of an odd number of quarter-wave dielectric layers of alternate high and low index. Maximum reflectance is always obtained with the high-index layers on the outboard side. The quarter-wave thickness of the layers in the stack of the coating is necessary to ensure that all the beams reflected from all the interfaces in the assembly are of equal phase when they reach the front surface where they combine constructively. More complex coatings are needed if the incident laser beam contains more than one wavelength. The reflectance of the coating is proportion-

al to the number of the layers and to the ratio of the refractive index of the high-index layers to that of the low-index layers. A typical high-index material is Al_2O_3, and a typical low-index material is SiO_2.

4.6.3 Radiation Damage to HR Coatings

To investigate the radiation damage to the coatings of the last mirror, and in the absence of any experimental data on the effect of irradiation on the optical properties of the coatings, it is helpful to state first the basic requirements of HR coatings, and to show the possible effects of irradiation on this required performance.

The first requirement of the HR coatings[2] on the last mirror is to have very high reflectance (> 99%), with correct spectral performance, and with uniformity of reflection over the coated surface. Correct spectral performance is the average value of reflectance for each wavelength to which the coating will be exposed. Lack of uniformity, which may result from variations in the thickness of the layers in the coating, could produce wavefront errors in the beam in addition to amplitude variations. These in turn affect beam propagation and focusing on the target. The possible effects of radiation on this requirement could be:

(a) Formation of Color Centers.[3,4] Most dielectric materials are susceptible to color center formation under neutron, ion and x-ray irradiation. The formation of these centers means the increase of absorption and the decrease of reflectance. Non-uniform distribution of these centers means also non-uniformity of reflectance mentioned above.

(b) Change of Refractive Indices. Irradiation with neutrons or ions could affect the refractive indices in the coating by different processes. It can change the density, the polarizability, the chemical bonding, and it

can destroy the crystalinity (for crystals) and the stoichiometry (for compounds). The change in the refractive indices due to neutron irradiation could be quite different from that produced by ion irradiation due to the different spatial extent of the damage produced in both cases. It was shown[5] that the change (increase) of the refractive index in fused silica due to inert gas implantation has almost the same depth distribution as the deposited energy that goes to atomic collision processes. It is expected that under both types of radiation that the refractive indices would be changed in a non-uniform manner that leads to change of reflectance and lack of its uniformity.

(c) Density Change. Density change due to irradiation could destroy the required uniformity of the quarter-wave thickness of the coating layers.

The second and the most important requirement of the HR coating is resistance to laser induced damage (LD). To minimize both the cost and the laser beam apertures, for a given laser power, the laser fluence on the coatings should be just below those which produce damage. The LD is caused by absorption of laser energy by particulate inclusions, physical defects or chemical impurities. These sites are randomly distributed over the coated surface with a typical surface density in high quality coatings of 100-1000/cm^2. The absorbed energy from the laser pulse heats a small volume around the defect site to the melting temperature or to the point of thermal-stress fracture. Another mechanism for LD is the creation of an absorbing plasma by electron avalanche initiated by free, or easily-liberated electrons.

Since most of the laser energy is concentrated in the outermost layers of the HR coating, laser damage occurs normally in the first or the second outermost layers. Consequently radiation damage that occurs only at those layers

would have impact on the resistance of the coating to LD. Sputtering, blistering, formation of color centers, all could add more absorption sites and decrease the resistance to LD. Change of density due to irradiation could build up stress that accelerates the LD. It was found[2] that adding a half-wave thick silica overcoat layer on the top of the HR coating would significantly increase the resistance of the coating to LD.

As mentioned earlier there is no known experimental data on the effect of neutron or ion irradiation on the optical properties of the dielectric coatings in the UV region. What is needed is an experimental verification of the change of both reflectance and LD resistance as a function of irradiation dose.

In the SOLASE study,[4] the conclusion about the use of coatings in laser fusion reactors was "...all the above problems may very well eliminate dielectric coatings for application in reactors. This has profound implications for the use of lasers in the 2000-6000 Å range...". Until the required experimental effort, mentioned above, is carried out, one has to be very concerned about the useful lifetime of the final focusing elements.

References for Section 4.6

1. H.A. Maclead, Thin-Film Optical Filters, American Elsevier Pub. Comp. Inc., New York, (1969).

2. W.H. Lowdermilk, "Coatings for Laser Fusion," SPIE Vol. 325 Optical Thin Films (1982).

3. P.D. Townsend and J.C. Kelly, Colour Centres and Imperfections in Insulators and Semiconductors, Crane, Russak & Comp. Inc., New York (1973).

4. R.W. Conn et al., "SOLASE, A Laser Fusion Reactor Study," University of Wisconsin Fusion Engineering Research Program UWFDM-220 (1977).

5. J. Heibei and E. Voges, "Refractive Index Profile of Ion-Implanted Fused Silica," Phy. Stat. Sol. (a) 57, 609 (1980).

5. CRITICAL ISSUES

The purpose of the SIRIUS study was to identify the critical issues associated with the conceptual design of a symmetric illumination laser fusion reactor. These issues may be broken down into categories in the following manner:

- TARGET
  - Injection of cryogenic targets into a reactor environment
  - Target performance vs. illumination uniformity
  - Target fabrication costs and reliability
- LASER
  - Repetitive operation
  - Reliability
  - Coupling of the laser hall to primary containment
- FOCUSING OPTICS
  - Radiation damage to mirror coatings
  - Alignment tolerances and uniformity of target illumination
  - Dimensional stability of large mirrors
- SiC TILES
  - Degradation of SiC at high temperatures
  - Tritium retention
  - Thermal and recoil stresses and fatigue
  - Radiation damage
  - Effects of target debris
  - Vaporization
  - Heat transfer properties of SiC at high temperatures

- BLANKET AND SHIELD
  - Pulsed radiation damage
  - Maintenance
  - Pulsed thermal behavior
  - Induced radioactivity and impact on maintenance
- ECONOMICS
  - Impact of cost of cavity blanket and shield on total cost
  - Extrapolation to commercial viability
  - Maximization of target gain and laser efficiency
- CAVITY
  - Vacuum pumping
  - Tritium recovery

Many of these are generic to all laser fusion reactor designs and some, such as target fabrication, are concerns for all inertial confinement fusion reactor concepts.

Several of these critical issues are specific to the SIRIUS design concept or symmetric illumination laser fusion in general. The aiming of the many symmetrically arranged mirrors and timing the firing of the laser, so that acceptable illumination uniformity on the moving target is achieved, is important to consider. The acceptable level of uniformity, which is needed to determine the aiming tolerances, must be determined by studying the target performance as a function of the illumination symmetry. If commercial viability is to be ultimately achieved, higher gain targets are needed in order to overcome the limited efficiency of the laser. These targets must be designed to operate with the achievable illumination uniformity. The final optics, which provide this illumination, must survive in the neutron environ-

ment. Therefore, neutron induced reduction in the threshold laser energy density for damage to the optics must be analyzed.

The use of SiC tiles to protect the first wall is a component of the design which influences much of the reactor cavity, blanket and shield. It is therefore of critical importance that the behavior of such tiles at high temperature be well understood. In the present analysis, certain assumptions are made about heat transfer in the tiles which are thought to be conservative. There are certain issues concerning the tiles about which very little is known and which may invalidate the present design. One such topic is degradation of SiC brought on by long periods at high temperature.

More general in nature but no less important are the blanket maintenance issues brought about by the complex geometry required for symmetric illumination. These complications will lead to a cost for the cavity which may be different than for two-sided or axisymmetric illumination. In order to proceed with an overall plant design, one must have an estimate of the cost of cavities relative to the total cost of the plant.

The discussion above indicates that there are many unanswered questions remaining which are critical to the SIRIUS design. This list is not complete because as reactor designs proceed more issues arise. Part of the value of the work to date has been to provide point design which brings some of the critical issues into focus.

6. CONCLUSIONS

It was found that recent indirect drive ICF reactor designs are not compatible with symmetric illumination of targets. Fortunately, the lower yield (100-150 MJ) direct drive targets allow a dry wall concept to be utilized. It has been concluded that there is no fundamental impediment to cavity blanket and shield design for the SIRIUS reactor concept proposed in this work.

There is further work which needs to be performed before one could proceed with a conceptual reactor design. Some of the most critical issues involve target performance as a function on non-uniformity of laser irradiation, radiation damage resistances of final focusing mirrors, and thermal performance of ceramic tiles such as SiC in the harsh radiation environment of the cavity. As found in many previous studies the commercial feasibility still depends very heavily on the laser and target performance.

Acknowledgement

This work has been supported by the U.S. Department of Energy.

APPENDIX I

Uniformity of energy deposition for laser driven fusion

Stanley Skupsky and Kotik Lee
Laboratory for Laser Energetics, University of Rochester, Rochester, New York 14623

(Received 18 January 1983; accepted for publication 1 April 1983)

Laser driven fusion requires a high degree of uniformity in laser energy deposition in order to achieve the high density compressions required for sustaining a thermonuclear burn. The characteristic nonuniformities produced by laser irradiation, with multiple overlapping beams, are examined for a variety of laser-target configurations. Conditions are found for which the rms variation in uniformity is less than 1%. The analysis is facilitated by separating the contributions from (1) the geometrical effects related to the number and orientation of the laser beams and (2) the details of ray trajectories for the overlapping beams. Emphasis is placed on the wavelength of the nonuniformities in addition to their magnitudes, as the shorter wavelength nonuniformities are more easily smoothed by thermal condution within the target. It is demonstrated how the geometrical symmetry of the laser system effectively eliminates the longer wavelengths, and how shorter wavelength nonuniformities can be "tuned out" by varying parameters such as the focal position and the radial intensity profile of the beam. The distance required for adequate thermal smoothing of the irradiation nonuniformities is found to be 2 to 3 times smaller than previously estimated due mainly to the relatively small spatial wavelength of the nonuniformities. This is a consequence of the geometrical symmetry of the laser system and is relatively insensitive to the details of overlapping beams. The results are particularly important for irradiation with short wavelength laser light (e.g., 0.35 μm), as the small smoothing distances anticipated for moderate laser intensities are found to produce adequate attenuation of the calculated nonuniformities.

PACS numbers: 28.50.Re

I. INTRODUCTION

To achieve high energy production by laser fusion, deuterium-tritium fuel must be compressed to ~ 1000 times its liquid density, and simultaneously heated above the ignition temperature (~ 5 keV) needed to sustain a thermonuclear burn.[1] Compression and heating of the fuel are obtained by depositing energy on the surface of a fuel-containing spherical target, causing surface material to be ablated, and driving the remainder of the target inward like a spherical rocket to implosion velocities greater than 10^7 cm/sec. For the method to be successful, a high degree of spherical convergence of the fuel is required, placing severe constraints on uniformity of energy deposition on the target surface. The level of nonuniformity in deposition that can be tolerated depends on the details of individual target designs. Typically an rms variation ($\sigma_{\rm rms}$) of less than a few percent is required.[2] Two approaches for using laser light to achieve high deposition uniformity are presently under investigation. One approach uses "hohlraum" targets to absorb the laser energy and convert it to x rays which drive the target[3] (indirect drive). The second method is to drive the target directly with laser light, by irradiating it with a large number of overlapping laser beams[4–7] (direct drive). The uniformity attainable by the second approach of direct irradiation is calculated here for different laser-target configurations, to investigate the nature of the nonuniformities associated with different parameters such as: number of beams, beam orientation, lens f-number, beam intensity profile, target scale lengths, etc. Results of the calculations suggest that some of the anticipated constraints on directly-driven targets (related to the separation distance between the critical and ablation surfaces) can be relaxed. This is partly the result of the high uniformity ($\sigma_{\rm rms} < 1\%$) obtained for some laser-target conditions, but it is mainly due to the relatively small spatial wavelength of the irradiation nonuniformities which are found to be several times smaller than previously estimated.

Processes involved in direct laser drive are illustrated in Fig. 1. Shown schematically are two overlapping beams at tangental focus, each beam irradiating half the target surface. The calculations below use examples with 24 and 32 such beams. Not shown in the figure, but included in the calculations, is the refraction of laser rays as they pass

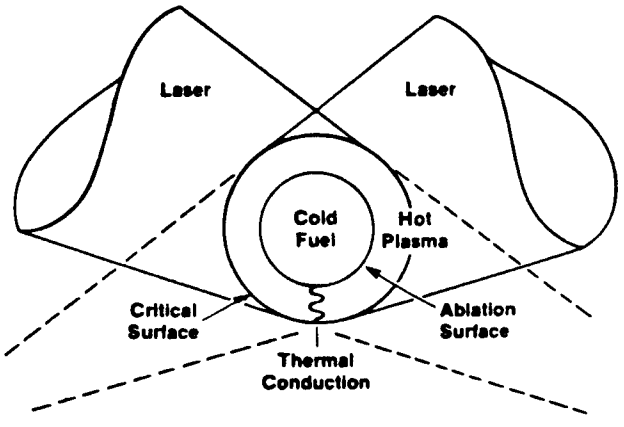

FIG. 1. High irradiation uniformity can be achieved by overlapping laser beams. The laser light is refracted in the plasma atmosphere surrounding the target, with the majority of energy deposited near the critical density. Heat is then transported inward to the ablation surface where the implosion is driven. Some smoothing of nonuniformities in energy deposition can occur over the distance of heat transport.

 0021-8979/83/073662-10$02.40

through the plasma atmosphere surrounding the target. After energy is deposited (which generally occurs close to the critical density) some of the nonuniformities in temperature are smoothed by thermal conduction[8,9] as heat is transported inward to the ablation surface where the implosion is actually driven. The shorter wavelength nonuniformities are more easily smoothed due to the proximity of the hotter and colder regions. Thus, in examining uniformity of energy deposition, we place considerable emphasis on calculating the spatial wavelength of nonuniformities in addition to their magnitudes.

The constraints on uniformity can be estimated as follows.[9,10] A nonuniformity in pressure at the ablation surface will cause a variation in velocity Δv of the target shell, and consequently a variation in the position δR of different parts of the target. At the time of peak compression, δR should be less than about $\frac{1}{4}$ of the imploded-core radius R to avoid complete mixing of the target material. The time for compression t is roughly R_0/v, in terms of the initial target radius R_0, and the average implosion velocity v. The total shell distortion is $\delta R = \Delta v \cdot t$, yielding $\delta R/R = (\Delta v/v)(R_0/R)$. Since the convergence ratio R_0/R is generally greater than ~ 10, the velocity variation $\Delta v/v$ must be kept below a few percent. The relationship between $\Delta v/v$ and the nonuniformity in energy deposition $\Delta\epsilon/\epsilon$ at the critical surface depends on the amount of thermal smoothing and on details of the target design. Without smoothing, the two should be comparable. For the purpose of these calculations, we seek conditions such that $\Delta\epsilon/\epsilon$ is less than $\sim 5\%$, or equivalently $\sigma_{\rm rms} \lesssim 1\%$, at the critical surface. The nonuniformity that actually reaches the ablation surface and drives the target is estimated using the thermal smoothing model discussed in Sec. II.

The thermal smoothing of a temperature nonuniformity is determined by the nonuniformity wavelength λ and by conditions in the target, particularly the separation distance ΔR between the critical and ablation surfaces. Classically, a temperature nonuniformity will be attenuated roughly by the factor[10]: $e^{-k\Delta R}$, where $k = 2\pi/\lambda$. (The attenuation can be different for saturated heat flow,[11] but the exact details are not important for the present discussion.) Previous estimates[12] have assumed that λ was approximately equal to the target radius R, requiring that $\Delta R/R$ be about 0.3 to achieve a tenfold attenuation. However, the results below indicate that the characteristic spatial wavelength can be 2 to 3 times smaller than R for a 32-beam laser system, reducing the required values of $\Delta R/R$ to about 0.1. In fact, results will be presented for $\Delta R/R = 0.05$.

It is particularly important for irradiation with short wavelength laser light, that adequate thermal smoothing can occur for small fractional separation distances ($\Delta R/R < 0.1$). Short wavelength light (e.g., $\lambda_L = 0.35\ \mu$m) has the attractive features of a high collisional absorption in the target and a high hydrodynamic efficiency for implosion,[13] but it has the drawback of a small fractional separation distance between the critical and ablation surfaces at moderate laser intensities[12] ($I \lesssim 10^{15}$ W/cm^2). The relation between $\Delta R/R$, laser intensity I, and laser wavelength λ_L has been calculated[12] to be approximately $\Delta R/R \sim (I\lambda_L{}^{3.8})^{0.7}$. Extrapolating the results of Ref. 12 to $\lambda_L = 0.35\ \mu$m (frequency-tripled Nd:glass light) and $R = 1$ mm, a laser intensity of $\sim 5\times 10^{15}$ W/cm^2 is required to produce $\Delta R/R = 0.3$; but if $\Delta R/R = 0.05$ is adequate for smoothing, then an intensity of only $\sim 5\times 10^{14}$ W/cm^2 is needed. The advantage of using lower laser intensities is that this minimizes early heating of the fuel by hydrodynamic shocks and heating by energetic electrons from plasma processes such as resonance absorption. Too much preheat will degrade the target performance by preventing a high-density compression.

This relation beween $\Delta R/R$ and I is based on steady-state conditions. Transient effects must also be considered. Uniformity at the start of irradiation, when plasma scale lengths are small, can be very different from uniformity at the peak of the laser pulse when the plasma has expanded. Until an adequate separation distance is established, the laser nonuniformities can imprint themselves on the target, causing surface damage which can "seed" the Rayleigh–Taylor fluid instability.[14] The instability grows exponentially in time and fastest for short wavelengths with the result that small surface defects can substantially degrade the target performance. These time-dependent effects are not discussed here but are under active investigation. The present calculations concentrate on the longer wavelength nonuniformities (spherical harmonic modes $l < 40$) using static target conditions as a first step in determining the effect on nonuniformity of different laser-target conditions.

The uniformity of energy deposition in the target is calculated by tracing laser rays through the plasma atmosphere according to geometrical optics, and depositing energy along the ray trajectory by inverse bremsstrahlung (Appendix). The calculation is greatly simplified by using beams with identical, azimuthally-symmetric intensity profiles and perfectly spherical targets. Then, only one beam must be calculated, and results for the other beams are obtained by rotation. To analyze the spatial variations of nonuniformities, the energy deposition pattern is decomposed into spherical harmonics. The nonuniformity wavelength λ in each spherical harmonic mode is related to the mode number l approximated by

$$\lambda = 2\pi R/l,$$

where R is the target radius. For identical beam profiles, the formalism developed in Sec. II, shows that the rms nonuniformity in each model σ_l can be written as the product of two factors which depend on, respectively,

(1) The geometrical configuration of the laser system, including the number and orientation of the laser beams, and the laser energy balance between beams;

(2) The energy deposition pattern from a *single* beam, which is determined by the focal position, intensity profile across the beam, lens f-number, and the density and temperature profiles in the target plasma.

If either factor is zero, then the nonuniformity σ_l in that mode is zero. For example, the geometrical term constrains the lowest dominant mode of nonuniformity to be about $l = 10$ for a 32-beam laser system, as it approximately eliminates all lower-order modes for perfect beam balance. (For reference, $l = 6$ corresponds to $\lambda \approx R$). The magnitude of the higher-order modes is affected by the single-beam fac-

tor which can even be "tuned" to eliminate some modes.

The effects of specific laser-target conditions are illustrated in Sec. IV using as examples: (1) the 24-beam OMEGA laser system at the University of Rochester,[15] and (2) a 32-beam system ("truncated" icosahedron) comprised of beams at the 20 faces and 12 vertices of an icosaherdron. The first system illustrates the uniformity potentially available with a presently-operating laser system. The second is an example of how high uniformity can be attained with the high f-number optics required for future fusion reactors. High f-number is required to keep the final optical elements as far from the target explosion as possible.[16] The results below show that high uniformity ($\sigma_{\rm rms} < 1\%$) is obtained with the 24-beam system, using $f/4$ lenses (which is adequate for present-day experiments), but the nonuniformity was found to double when the f-number was increased to 10. For the 32-beam system, however, $\sigma_{\rm rms} < 1\%$ is obtained with $f/20$ lenses (subtending a total solid angle of only $1/2\%$ of 4π), which is well within the range envisaged for fusion reactors.[16]

II. FORMALISM

In order to calculate the magnitude and wavelength of nonuniformities from multiple, overlapping laser beams, it is convenient to express the energy density deposited on target $\epsilon(\mathbf{r})$ as the sum of energies from the individual beams $\epsilon_k(\mathbf{r})$.

$$\epsilon(\mathbf{r}) = \sum_k \epsilon_k(\mathbf{r}) . \tag{1}$$

Interference between beams has been neglected as the fringe separation is estimated to be less than $\sim 1\,\mu$m (Ref. 6), corresponding to $l \sim 1000$ for a 1-mm-radius target. Such small-scale variations should be easily smoothed by thermal conduction once a plasma is established, but prior to that they might damage the target surface and "seed" the Rayleigh–Taylor instability.[14] Throughout, we use laser-beam intensity profiles that are azimuthally symmetric around the beam axis, with the axis passing through the center of the target. (The effect of off-center beams is estimated in Sec. IV). The energy deposited at a position $\mathbf{r}$ is then determined by only the distance from the target center $|\mathbf{r}|$ and the angle α_k between $\hat{r}$ and the beam axis $\hat{\Omega}_k$ (Fig. 2), i.e.,

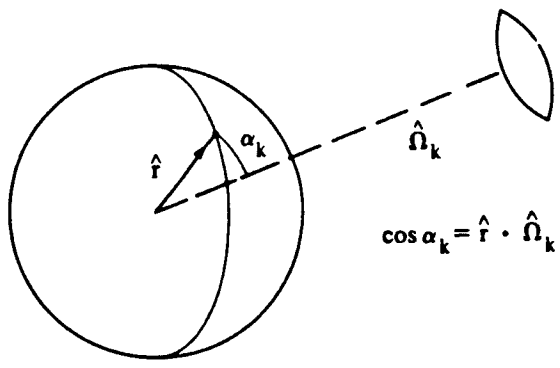

FIG. 2. Energy deposition pattern for any laser beam k depends only on the angle α_k from the beam axis (for azimuthally symmetric beam profiles) and on the distance r from the target center, in a spherically symmetric target.

$$\epsilon_k(\mathbf{r}) = \epsilon_k(r,\alpha_k)$$

and

$$\cos(\alpha_k) = \hat{r}\cdot\hat{\Omega}_k .$$

The energy density ϵ_k is obtained by tracing rays through the target plasma, using inverse bremsstrahlung absorption (Appendix). To obtain a conservative estimate of uniformity, only the energy deposited between the critical and 0.4 critical densities is used, as discussed in Sec. III B. (The results are relatively insensitive to choices of a cutoff between 0.5 and 0.3 critical density.) Integrating ϵ over the region between critical and 0.4 critical density, at radii R_1 and R_2, we obtain the energy (or power) deposited per solid angle:

$$E_k(\alpha_k) = \int_{R_1}^{R_2} \epsilon_k(\alpha_k, r)\, r^2 dr .$$

The spatial wavelength dependence of nonuniformities in energy deposition is found by expanding $E_k(\alpha)$ in Legendre polynomials:

$$E_k(\alpha) = W_k \sum_l \frac{2l+1}{2} E_l\, P_l(\cos\alpha) , \tag{2}$$

where

$$E_l = W_k^{-1} \int_{-1}^{1} E_k(\alpha)\, P_l(\cos\alpha)\, d(\cos\alpha)$$

and the beam energy W_k has been explicitly factored out. The decomposition for the total energy distribution is the sum of Eq. (2) over all beams:

$$E(\hat{r}) = \sum_l \frac{2l+1}{2} E_l \sum_k W_k\, P_l(\hat{r}\cdot\hat{\Omega}_k) , \tag{3}$$

where each beam is assumed to have the same energy deposition pattern, but different beam energies are considered. Using the sum rule for Legendre polynomials:

$$P_l(\hat{r}\cdot\hat{\Omega}_k) = \frac{4\pi}{2l+1} \sum_{m=-l}^{l} Y^*_{lm}(\hat{\Omega}_k)\, Y_{lm}(\hat{r}) ,$$

Eq. (3) can be rewritten in terms of spherical harmonics:

$$E(\hat{r}) = 2\pi \sum_{lm} E_l \left[\sum_k W_k\, Y^*_{lm}(\hat{\Omega}_k)\right] Y_{lm}(\hat{r}) . \tag{4}$$

A useful measure of the illumination nonuniformity is the rms deviation defined as

$$\sigma_{rms} = \left(\frac{1}{4\pi}\int |E(\hat{r}) - \langle E\rangle|^2\, d\hat{r}\right)^{1/2} \Big/ \langle E\rangle , \tag{5}$$

where $\langle E\rangle = \int E(\hat{r})d\hat{r}/4\pi$. Substituting Eq. (4) into Eq. (5) and using the orthogonal property of spherical harmonics, $\sigma_{\rm rms}$ can be written explicitly in terms of the contribution from each l mode:

$$\sigma_{\rm rms} = \left(\sum_{l\neq 0} \sigma_l^2\right)^{1/2} , \tag{6}$$

where σ_l is

$$\sigma_l = |E_l/E_0| \left[(2l+1)\sum_{kk'} P_l(\hat{\Omega}_k\cdot\hat{\Omega}_{k'})\, W_k W_{k'}/W_T^2\right]^{1/2} , \tag{7}$$

and W_T is the total energy in the beams: $W_T = \Sigma\, W_k$. The significance of the factors in σ_l is discussed in Sec. III, and σ_l

is evaluated for different conditions in Sec. IV.

Another measure of nonuniformity is the peak-to-valley variation $\Delta E/E$. We use $\sigma_{\rm rms}$ here because it can be expressed analytically [Eq. (7)], and the different factors can be examined directly. In contrast, the peak-to-valley variation requires a computer search over the target surface to find the extreme values of E. Typically, $\Delta E/E$ was found to be 3 to 5 times larger than $\sigma_{\rm rms}$ for the different cases examined.

The nonuniformity in energy deposition $\sigma_{\rm rms}(E)$ can be attenuated by thermal conduction. To estimate the nonuniformity in pressure $\sigma_{\rm rms}(P)$ that actually reaches the ablation surface we make the following approximations: (1) The nonuniformity in temperature at the critical surface is equal to the nonuniformity in energy deposition; (2) a temperature nonuniformity of wave number k is attenuated by the factor $\exp(-k\Delta R)$ which corresponds to $\exp(-l\Delta R/R)$ for each spherical harmonic mode; and (3) the pressure nonuniformity at the ablation surface is equal to the attenuated temperature nonuniformity. From this model, the pressure nonuniformity at the ablation surface is related to the nonuniformity in laser energy deposition by

$$\sigma_{\rm rms}(P)=\left\{\sum(\sigma_l(E)\,e^{-l\Delta R/R})^2\right\}^{1/2}.$$

Results are shown in Sec. IV for $\Delta R/R=0.1$ and 0.05.

III. FACTORS CONTRIBUTING TO NONUNIFORMITY

The quantity σ_l [Eq. (7)], characterizing the contribution of each mode to nonuniformity, is factored into two terms. The first, $|E_l/E_0|$, depends on the ray-trace results for a *single* beam. The second factor contains all the geometrical information about the laser system related to the number and orientation of the beams, and the energy balance between beams. The nonuniformity in a mode can vanish, if conditions are found such that either of the two factors is zero. The dependence of each factor on laser and target conditions is now examined.

A. Geometrical and symmetry considerations

Several general results about uniformity are determined by just the number and orientation of the laser beams. These are independent of details about beam overlap or the laser absorption process. For identical, individual beams on target, the entire difference in uniformity between the various laser configurations (e.g., 12 or 32 beams) is contained in the second term in Eq. (7), denoted by the geometrical factor G_l:

$$G_l=\left[(2l+1)\sum_{kk'}P_l(\hat{\Omega}_k\cdot\hat{\Omega}_{k'})\,W_k W_{k'}/W_T\right]^{1/2}. \qquad (8)$$

This term depends on the geometry of the system (i.e., the number and orientation of the beams) through the dot product between the axis directions of all beams, and it depends on the energy W_k of each beam.

One simple result from symmetry is that all odd order values of G_l (and consequently σ_l) vanish for any laser system having opposing beams with equal beam energies. Physically, this means that the intensity patterns on both sides of any great circle around the target are the same. Mathematically, the result is obtained by rewriting the k' sum in terms of only the beams above the target equator, using $P_l(-\hat{\Omega})=(-1)^l P_l(\hat{\Omega})$ for opposing beams below the equator, i.e.,

$$G_l=\left\{(2l+1)\sum_k\sum_{k'}[1+(-1)^l]\,P_l(\hat{\Omega}_k\cdot\hat{\Omega}_{k'})\right\}^{1/2}\frac{1}{N},$$

using $W_k=W_{k'}$ and N is the number of beams. The vanishing of odd modes is immediately obtained, and is independent of the choice of the equatorial circle.

As another example, we estimate the lowest dominant mode of nonuniformity as follows. The angle between two beam axes, $\cos^{-1}(\hat{\Omega}_k\cdot\hat{\Omega}_{k'})$, is approximately an integral multiple of d/R (for a large number of beams N) where d is the average distance between beam axes across the target surface and R is the target radius. To obtain d, the target surface area is divided into N circles; $4\pi R^2=N\pi(d/2)^2$ yielding $d/R=4/\sqrt{N}$. When these angles are substituted into P_l in Eq. (8), they produce roughly randomly varying numbers between -1 and 1, and the sum is small, unless d is the characteristic wavelength of the Legendre polynomial, $2\pi R/l$. Thus the condition for the terms adding in phase is for l to be an integral multiple of $2\pi R/d$ or equivalently[17]

$$l=\pi\sqrt{N}/2. \qquad (9)$$

This approximates only the *lowest* mode for the nonuniformity. The total nonuniformity will contain higher modes and the average value of l can be considerably higher than the estimate in Eq. (9). For laser systems with 12, 20, 24, and 32 uniformly distributed beams, the estimated lowest dominant modes are $l=5$,7, 8, and 9, respectively.

For a more detailed analysis of the mode structure, the geometrical factor G_l [Eq. (8)] is evaluated exactly for four beam configurations: dodecahedron (12), icosahedron (20), OMEGA at the University of Rochester (24), and a 32-beam system. Coordinates for the first two can be found in Ref. 5; the last two are listed in Table I. The 32-beam configuration ("truncated" icosahedron) corresponds to an icosahedron with beams centered at the 20 faces and on the 12 vertices.

TABLE I. Orientation of beams for two laser systems.[a]

	OMEGA (24-Beam)		32-Beam System	
	θ	ϕ	θ	ϕ
1	30.361	45.0	0	0
2	30.361	135.0	37.377	0
3	30.361	225.0	37.377	72
4	30.361	315.0	37.377	144
5	69.059	22.5	37.377	216
6	69.059	67.5	37.377	288
7	69.059	112.5	63.435	36
8	69.059	157.5	63.435	108
9	69.059	202.5	63.435	180
10	69.059	247.5	63.435	252
11	69.059	292.5	63.435	324
12	69.059	337.5	79.188	0
13			79.188	72
14			79.188	144
15			79.188	216
16			79.188	288

[a] Angles are in degrees. Opposing beams have coordinates $\theta\rightarrow 180-\theta$ and $\phi\rightarrow 180+\phi$.

TABLE II. The geometrical contribution to nonuniformity [Eq. (8), with $W_k = 1$] for different laser systems. All odd modes are zero from symmetry.

	G_l			
l/Beams	12	20	24	32
2	0.0	0.0	0.0	0.0
4	0.0	0.0	0.1	0.0
6	2.4	1.5	0.3	0.1
8	0.0	0.0	1.7	0.0
10	1.7	2.8	1.5	2.2
12	2.9	0.0	1.6	1.0
14	0.0	0.0	0.0	0.0
16	2.5	2.9	1.2	0.7
18	3.2	1.5	3.0	2.1
20	0.6	3.0	0.4	2.0

The first 10 even modes of G_l are listed in Table II and show qualitative agreement with the estimate from Eq. (9). (Odd modes are zero from the symmetry discussion above.) Comparing the 20- and 24-beam systems: for 20 beams the lowest order nonuniformity is concentrated into two modes, $l = 6$ and $l = 10$; while it is spread out between $l = 6$ and $l = 12$ for 24 beams. The difference in concentration of the modes presumably lies in the higher-order symmetry of the icosahedron configuration. In going from 20 to 32 beams, we see that the higher symmetry of the 32-beam system results in elimination of the $l = 6$ mode, leaving $l = 10$ as the lowest dominant mode.

To obtain a high degree of uniformity, the single beam factor $|E_l/E_0|$ must be "tuned" (e.g., by focus or by varying the beam intensity profile), until it is negligible for those modes where G_l is large. For example, high uniformity for $l < 10$ is obtained in the 32-beam system by tuning out only a single mode, $l = 10$. However, for the other three configurations considered, E_l must be small for several modes simultaneously. As a result, high uniformity is most easily obtained with the 32-beam system. This is a consequence of geometrical symmetry, assuming perfect energy balance between beams. The effect of beam imbalance is discussed in Sec. IV.

B. The single beam factor

The single beam factor $|E_l/E_0|$ in Eq. (7) is calculated by dividing the laser beam into individual rays and tracing the rays through the refractive target atmosphere using geometrical optics (Fig. 3 and Appendix) and depositing energy into the target by classical absorption (inverse bremsstrahlung). Wave effects can create diffraction fringes which are treated in an approximate way (Sec. IV A) by superposing intensity variations on the radial beam profile. All the examples below use 0.35-μm laser irradiation (frequency-tripled, Nd-glass light) for which uniform energy deposition is a particularly crucial issue (Sec. I). For 0.35-μm illumination at moderate laser intensities ($\lesssim 10^{15}$ W/cm^2), light is absorbed predominately by inverse bremsstrahlung[18] due to the relatively high critical density. At higher intensities, plasma processes such as resonance absorption can become important, but these have not been considered here.

All examples use a 500-μm-radius target. The plasma atmosphere is at a temperature of 3 keV, with a density profile of 10 μm between critical and 1/3 critical density (except in Sec. IV B) and a 50-μm scale length beyond. Such double scale-length profiles are obtained in computer simulations of high-intensity laser irradiation with flux-limited heat flow.[19] All the energy deposited in the short scale-length (10 μm) region should contribute about equally to the implosion as it covers a range of just a few electron mean free paths. However, the energy deposited beyond 1/3 critical density can be at a relatively long distance from the ablation surface and should be less effective in driving the target. Since we are interested in drive uniformity, this distant energy deposition is not included in the calculation of σ_{rms} in order to obtain a conservative estimate. This energy represents about 15% of the total and is relatively uniformly distributed. Including it in the results can reduce σ_{rms} by up to a few percent. (Since this energy is not included, the results are insensitive to the choice of the 50-μm scale length.) The sensitivity to the shorter scale-length is discussed in Sec. IV B.

To illustrate how the single-beam factor E_l can be "tuned" by focus, we use the example of the 32-beam, $f/20$ system, with a quadratic laser-intensity profile:

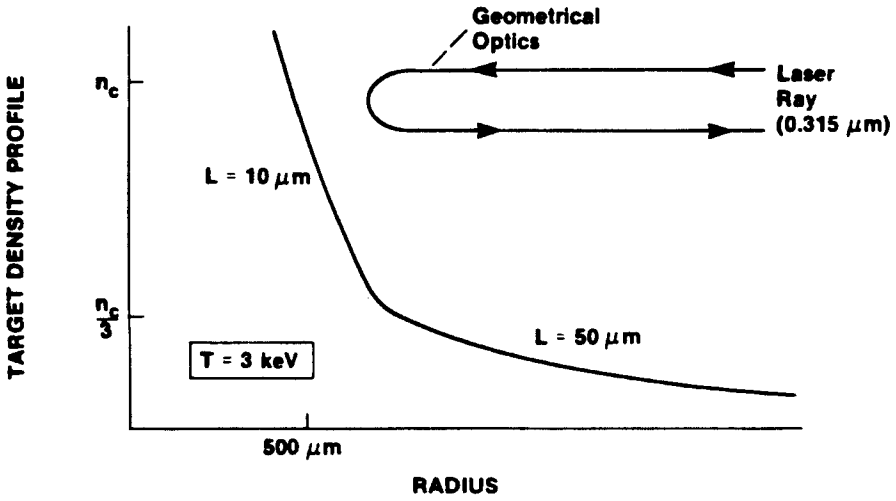

FIG. 3. Target conditions used for most examples consisted of a fully ionized CH_2 plasma at a temperature of 3 keV. Critical density was at a radius of 500 μm. Exponential density profiles were used with a scale-length L of 10 μm between critical density, n_c, and 1/3 critical density; and a 50-μm scale length beyond. The laser rays followed a trajectory given by geometrical optics and deposited energy by inverse bremsstrahlung.

TABLE III. Variation of the single beam factor $|E_l/E_0|$ in Eq. (7) with focus for an $f/20$ lens. Note how the $l = 10$ component can be "tuned-out" to achieve high uniformity for the 32-beam system. The focus is in target radii behind the target. $40R$ is tangential focus.

l/Focus	$\lvert E_l/E_0\rvert \times 100$		
	32	35.6	38
1	88.1	85.3	84.0
2	67.9	62.0	58.8
3	44.9	37.4	33.4
4	24.5	18.0	15.0
5	10.0	6.4	5.1
6	2.2	1.4	1.4
7	−0.6	0.1	0.4
8	−0.7	0.0	0.1
9	0.0	0.1	−0.2
10	0.4	0.0	−0.2
11	0.2	0.0	0.0
12	−0.0	0.0	0.2
13	−0.2	0.1	0.1
14	−0.1	0.0	−0.0
15	0.0	0.0	−0.1

$I(r) = I_0(1 - r^2/r_0^2)$, where r is the radial distance from the center of the beam, and r_0 is at the beam edge. Results for E_l at different focal positions are listed in Table III. The $l = 10$ value passes through zero at a focus of 35.6 target radii (R) behind the target. ($40R$ is tangential focus.) The small values of E_{10} around $35R$ compensate for the relatively large value of the geometrical factor G_{10}, (Table II) resulting in a total nonuniformity $\sigma_{\rm rms}$ of less than 0.5% (Sec. IV A).

IV. RESULTS

The uniformity of laser energy deposition is now examined for different laser and target conditions. Both the 24-beam OMEGA system and the 32-beam system of Table I are used in the examples. From among the large number of possible variables, we consider some aspects of the following: (1) radial laser-intensity profile, (2) focus, (3) beam number and configuration, (4) plasma-density profile in the target, (5) energy balance between beams, and (6) beam-target alignment. The nonuniformity in energy deposition created by these factors is not necessarily the nonuniformity that will drive the target implosion. Some nonuniformities can be smoothed by thermal conduction. The longer wavelength nonuniformities are the most difficult to attenuate due to the relatively long distance between the hot and cold regions. Beam-imbalance and laser-target misalignment are found to be the main contributors to these modes ($l<4$). The remaining variables are responsible for shorter wavelength nonuniformities. For these results, $\sigma_{\rm rms}$ is calculated from Eqs. (6) and (7) using the first 40 modes. The target plasma conditions are as described in Sec. III B, except for the examples in Sec. IV B.

A. Beam profiles, focus, and beam configuration

The rms variation in energy deposition for the 24-beam system is shown in Fig. 4(a), for three different radial beam profiles as a function of focus. Two of the profiles are: (1) quadratic, $I = I_0(1 - r^2/r_0^2)$ and (2) flat top, $I = I_0$ for $r < r_0$.

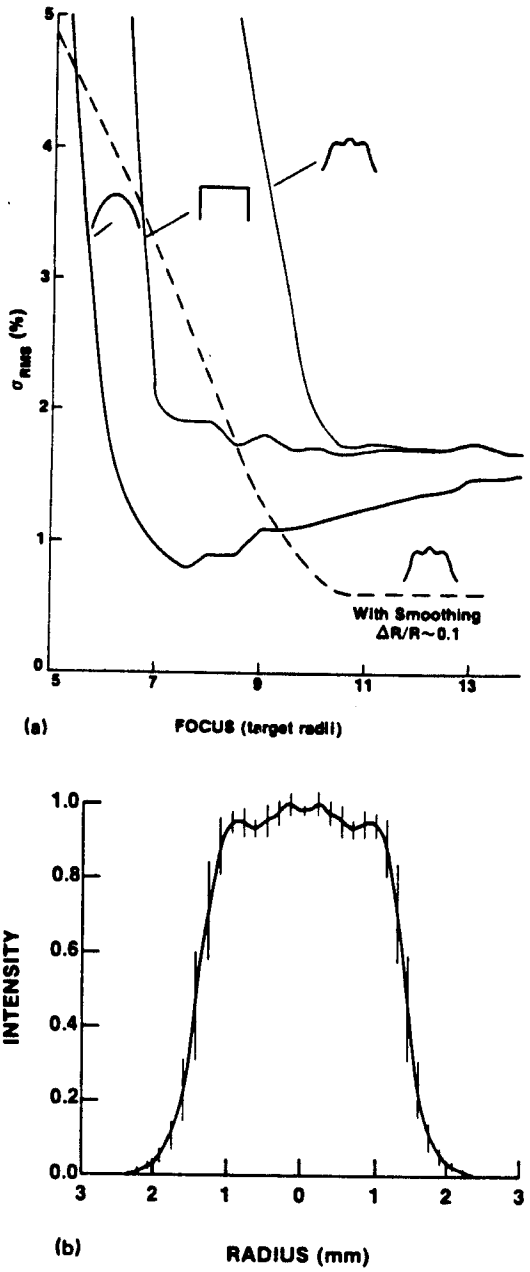

FIG. 4. (a) Effect of the laser-beam intensity profile on uniformity for the 24-beam OMEGA system, as a function of focus. Compared are a quadratic, flat-top, and recent experimental profile (b). The focal position is expressed in terms of target radii behind the target; $8R$ is tangential focus here. Note that the 2% nonuniformity level is relatively independent of beam profile and can be achieved by defocussing the beam beyond tangential focus. Moderate thermal smoothing, corresponding to $\Delta R/R \sim 0.1$ reduces the "asymptotic" nonuniformity below 1%. (b) An azimuthally-averaged intensity profile from the University of Rochester. The vertical bars indicate the variation around the average.

The third is a recently obtained experimental profile from the University of Rochester[20]; details are shown in Fig. 4(b) where the bars indicate the variation around the aximuthal average. Comparing these three three profiles, the qualitative result is that the highest uniformity ($\sigma_{\rm rms} < 1\%$) requires smoothly varying profiles without sharp edges. (The effect of small intensity variations are discussed more quantitatively below.) The ideal quadratic-like shape need not be produced

directly by the laser, but can be created in the target plane by the final focusing elements. Note that beyond tangential focus [corresponding to 8 target radii, $8R$, behind the target in Fig. 4(a)] the uniformity is insensitive to the beam shape. All profiles converge to the same result ($\sigma_{rms} \sim 2\%$) because only the central part of the beam—which is similar for these profiles—reaches the target; the outer part is refracted. The 2% nonuniformity level does not require profiles very different from those presently available (though, deviations from azimuthal symmetry have not yet been considered). The penalty for energy loss by refraction is relatively small in this example; the fractional absorption decreases by about 15% in defocussing rom $7R$ to $12R$. Further, the nonuniformity can be substantially reduced if there is a moderate amount of thermal smoothing in the target. Shown in Fig. 4(a), is the result of multiplying the rms nonuniformity in each mode σ_l by $\exp(-l/8)$, corresponding to $\Delta R/R = 0.125$ in Sec. II. This model of smoothing reduces σ_{rms} to below 1% for focussing beyond $10R$. Thus, near-term experiments can proceed with relatively high uniformity, in parallel with the development of a beam shaping capability.

The 24-beam ($f/4$) system is compared with the 32-beam ($f/20$) system in Fig. 5 using the quadratic profile. (Here the focus parameter should be multiplied by twice the f number to obtain target radii; tangential focus equals 1 in these units.) There is a factor of 2 decrease in nonuniformity over a small focal range for the 32-beam system. The improved uniformity for 32 beams is the result of higher geometrical symmetry (Sec. III A), and it is particularly impressive since the solid angle subtended by the lenses is about 10 times smaller than for the 24-beam system. Note that the results are relatively insensitive to f numbers greater than ~ 10 as the laser rays are effectively parallel at that point.

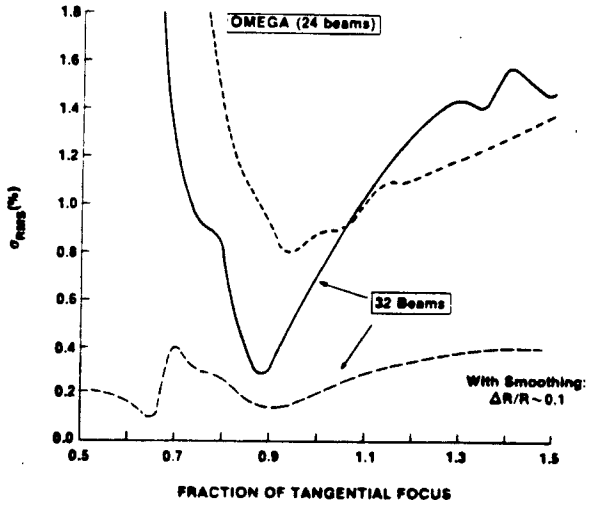

FIG. 5. Comparison of nonuniformity between the 24-beam ($f/4$) laser system and the 32-beam ($f/20$) system using a quadratic beam profile. Also shown is the reduction in nonuniformity by thermal smoothing which is modeled here by multiplying each mode σ_l by the factor $\exp(-l/8)$ corresponding to $\Delta R/R \sim 0.1$. The focus is expressed as the ratio F/F_{tan} where F is the focal position (in target radii, R) and F_{tan} is the position of tangential focus. F_{tan} is $8R$ and $40R$ respectively for $f/4$ and $f/20$ lenses.

The high values of uniformity ($\sigma_{rms} < 1\%$) are obtained over a limited focal region. It is difficult to remain in this region during the entire laser fusion implosion, as the focus (expressed in terms of the instantaneous target radius) will be constantly changing. One strategy is to focus so that the highest uniformity is obtained initially. At later times the nonuniformity will increase; but the target plasma will have expanded, and it could permit some thermal smoothing of the short wavelength nonuniformities. The effect of thermal smoothing is estimated in Fig. 5 for the 32-beam system, again by multiplying each σ_l by $\exp(-l/8)$. With such smoothing the nonuniformity remains at the 0.3% level over the entire focal range shown.

A decomposition of σ_{rms} into wavelengths of the nonuniformity characterized by σ_l [Eq. (7)] is shown in Table IV which compares the 24- and 32-beam systems for various conditions. Column 1 lists the mode structure for the 24-beam system with a quadratic profile and perfect beam balance, near optimal focus. The higher-order modes ($l>6$) have been approximately "tuned out" and the $l=4$ mode is left with most of the nonuniformity. Although the geometrical factor for $l=4$ is relatively small (Table II), the single beam factor is large (Table III), and it is relatively insensitive to focal position, radial profile, and f number. For comparison, column 2 lists σ_l for the 32-beam system, also with a quadratic profile and near its optimal focus. The single beam factor has tuned out the $l=10$ mode and the geometrical factor has eliminated the lower modes to produce the total, $\sigma_{rms} = 0.3\%$. However, the tuning depends on beam profile in addition to focus, as seen in column 3, for the $l=10$ nonuniformity is sharply increased when the quadratic profile is replaced by a flat top. The effect of energy imbalance between beams (last column) is discussed below.

Realistic radial beam profiles might not be as smooth as the quadratic form used here due to, for example, diffraction effects. The effect of small-scale variations on the radial

TABLE IV. The magnitude of the nonuniformity σ_l [Eq. (7)] for different spherical harmonic modes l. The value of σ_{rms} is obtained from the first 40 modes [Eq. (6)].

			σ_l(%)	
Beam number:	24	32	32	32
Radial profile:	Quadratic	Quadratic	Flat Top	Quadratic
F number:	4	20	20	20
Focus:	$7.5R$	$36R$	$36R$	$36R$
Energy imbalance:	0%	0%	0%	2%
$l=$ 2	0.1%	0.1%	0.1%	$l=1$ 0.1% $l=2$ 0.6 $l=3$ 0.4
4	0.7	0.1	0.0	$l=4$ 0.1
6	0.1	0.1	0.0	0.1
8	0.1	0.0	0.0	0.0
10	0.0	0.1	2.3	0.1
12	0.2	0.0	0.6	0.0
14	0.0	0.0	0.0	0.0
16	0.1	0.0	0.1	0.0
18	0.1	0.1	0.1	0.1
20	0.0	0.1	0.1	0.1
$\sigma_{rms}=$	0.8%	0.3%	2.4%	1.1%

beam shape is examined using a modulated quadratic profile of the form:

$$I = I_0(1 - r^2/r_0^2)\,[1 + \epsilon \cos(\pi N r/r_0)]\,,$$

where ϵ and N are parameters controlling the magnitude and wavelength of the modualations. Physically, $N/2$ corresponds to the number of diffraction rings. For the 32-beam system at $36R$ focus (which is near the optimum in Fig. 5), Fig. 6 shows σ_{rms} as a function of N for $\epsilon = 0.1$ (i.e., $\Delta I/I = 20\%$). Note the resonance effect when the profile modulations enhance the normal modes of nonuniformity from the overlapping beams. The dominant mode of nonuniformity is indicated on the graph. (Part of the drop in nonuniformity for large N occurs because only the first 40 modes are included in the calculation of σ_{rms}.) Beams with more than ~ 4 rings ($N > 8$) create relatively short wavelength nonuniformities, $l > 20$, which can be smoothed over small separation distances between the critical and ablation surfaces. To demonstrate the effect of only a small amount of smoothing, we multiply each σ_l by the factor $\exp(-l/20)$, corresponding to $\Delta R/R = 0.05$ in Sec. II. Note the rapid drop in nonuniformity in Fig. 6, for $N > 8$. From this smoothing model, the results suggest that laser systems for future fusion reactors should be designed with not less than ~ 4 diffraction rings and/or an intensity variation $\Delta I/I$ considerably less than the 20% used here, both of which are within the limits of present-day technology.

B. Plasma density profile

The uniformity of energy deposition on target is affected by the plasma density profile, which determines the refraction of laser rays through the target atmosphere. An exponential profile with a 10-μm scale length between critical and 1/3 critical density was used above. The effect of changing the density scale length is shown in Fig. 7 for the 24-beam system. The curves are for 5- and 25-μm scale lengths in exponential profiles; the scale length beyond 1/3 critical density is 50 μm as above. Higher uniformity over a larger focal region is obtained with the longer scale length (in addition to more absorption). The difference between the two curves illustrates the sensitivity of uniformity results to target conditions when the level of nonuniformity σ_{rms} is on the order of 1%. In particular, it points out the importance of refraction in determining uniformity.

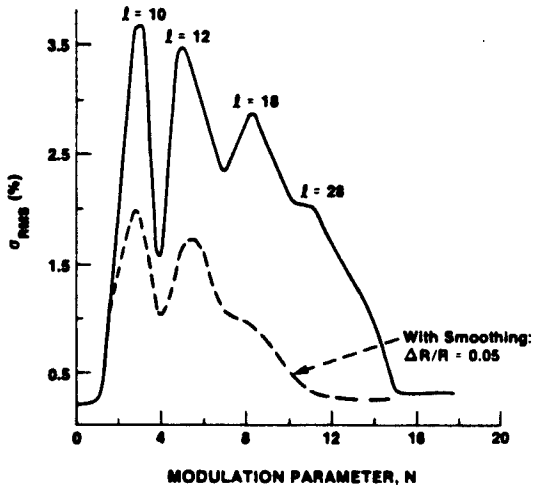

FIG. 6. Effect of diffraction fringes are modelled by superposing intensity variations ($\Delta I/I = 20\%$) on a quadratic beam profile. Nonuniformity σ_{rms} is plotted for the 32-beam system (at $36R$ focus) in terms of the number of peak-to-valley variations, N. Physically, $N/2$ can represent the number of diffraction rings. The indicated mode numbers show the dominant mode of nonuniformity contributing to σ_{rms}. Only a small amount of thermal smoothing (corresponding to $\Delta R/R \sim 0.05$) is required to smooth the nonuniformities from beams with more than about 4 rings ($N > 8$), due to the small spatial wavelength of the nonuniformities.

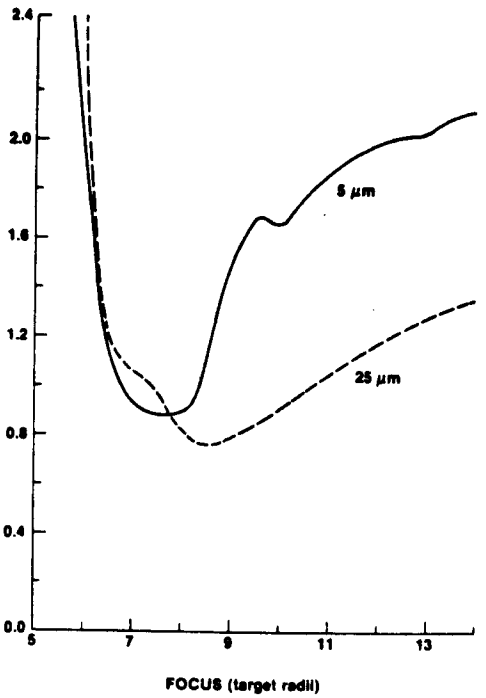

FIG. 7. Dependence of uniformity on target plasma scale length. The two scale lengths 5 and 25 μm are between the critical and 1/3 critical densities.

C. Beam balance

The symmetry results in Sec. III A and the uniformity results above have assumed that each of the laser beams has the same energy, i.e., the factor W_k in Eq. (7) is constant. In practice, there can be energy variations between beams. This will modify the results; in particular, odd-order modes will be introduced. This effect is illustrated in the last column of Table IV, using the 32-beam system near optimal conditions. The beam energies were chosen randomly over a range of 4%, producing a 2% rms variation in this example. Comparing with column 2, we see that the main effect is to modify the modes $l = 1$–3, leaving the remainder effectively unchanged. The total nonuniformity in these modes is roughly proportional to the rms energy imbalance. Reducing the rms imbalance to 0.5%, reduces the σ_{rms} for nonuniformity to $\sim 0.4\%$ for these laser-target conditions. Such beam balance is not far from that presently achievable.[20]

D. Alignment

When all beam axes do not pass through the center of the target due to either misalignment of the target or errors

in pointing the beam, there will be two effects: (1) the center of energy deposition per beam on the target surface will be shifted, and (2) the pattern of energy deposition will no longer be azimuthally symmetric. Only the first effect is estimated here by moving the positions of the lenses (but with the axes still passing through the target center).

As an example, the position of each beam was randomly placed within 1° from its correct orientation, as measured from the target center, for the 32-beam system. The effect was to modify the energy distribution on target. It created a result similar the 3% rms energy variation between beams in Table IV, modifying only the first 3 modes. A more exact treatment of this effect is presently in progress.

V. SUMMARY

The subject of uniformity for laser driven fusion requires the understanding of four aspects of the problem: (1) the trajectories of laser rays through the target atmosphere; (2) the distribution and mechanism of laser energy deposition; (3) the transport of energy to the ablation surface and the resulting pressure distribution there; and (4) the dynamic response of the target to the irradiation pattern. The first three topics were examined here using static, spherically symmetric density profiles in the target as a first step in identifying some of the dominant laser-target parameters contributing to nonuniformity. Future work requires the analysis of the dynamic response of the target to irradiation nonuniformities, including feedback on the ray trajectories from the plasma response.

The analysis of uniformity was facilitated by separating out the geometric contribution of beam orientation from the details of ray trajectories and energy deposition. It was illustrated how the geometrical symmetry of the beam configuration effectively eliminates the longer wavelength nonuniformities (for perfect beam balance) and how the shorter wavelength nonuniformities can be "tuned out" by varying the focus of the beam and its radial intensity profile. For an rms variation of 1% between beam energies, examples were found such that $\sigma_{\rm rms}$ for the nonuniformity in laser deposition was less than 1% for the high f-number lenses required for fusion reactors, but over a limtied focal region. The focal range could be significantly extended if there was a moderate amount of thermal smoothing in the target. The level of $\sigma_{\rm rms} \sim 2\%$ was achieved, with a variety of laser radial intensity profiles, by defocusing the beam beyond tangential focus (with a small loss in energy absorption). Energy imbalance between beams and laser target misalignment were found to create the longest wavelength nonuniformities ($l<3$) which would not be significantly attenuated by thermal conduction.

Adequate thermal smoothing of nonuniformities (for good beam balance) was found to occur for fractional separation distance ($\Delta R/R$) between the critical and ablation surfaces that are factors of 2 to 3 smaller than previously estimated. This is particularly important for laser fusion experiments using short wavelength irradiation (e.g., $\lambda_L = 0.35\,\mu$m) which are expected to produce small values of $\Delta R/R$ at moderate laser intensities. Small separation distances ($\Delta R/R \sim 0.05$ in Fig. 6) can be adequate because, to a large degree, the characteristic spatial wavelengths of nonuniformities were found to be small ($\lambda \sim R/3$). This result is a consequence of the geometrical symmetry of the laser system and is relatively insensitive to the ray-trace details of overlapping beams.

ACKNOWLEDGMENTS

We wish to thank R. Hopkins, R. McCrory, and J. Soures for valuable discussions, and J. Boles for bringing the 32-beam configuration to our attention. This work is supported by the U. S. Department of Energy Inertial Fusion Project under contract No. DE-AC-08-80DP40124.

APPENDIX

The equations used to obtain the deposited energy-density ϵ_k [Eq. (1)] for a single beam are described below.

The trajectory for a laser ray in a spherically symmetric plasma is written in terms of five variables, r, θ, s, γ, and n: r and θ are the radius and polar angle measured from the target center to a point on the ray trajectory; s is the distance along the trajectory; γ is the angle between the direction of ray propagation $\hat{s}$ at that point and the radius vector $\hat{r}$, i.e., $\cos\gamma = \hat{r}\cdot\hat{s}$; and n is the index of refraction which, for a plasma, is determined by the electron density n_e and the critical density n_c according to $n = (1 - n_e/n_c)^{1/2}$. The equations are[21]

$$rn\sin\gamma = \text{constant},$$

$$d\theta/ds = r^{-1}\sin\gamma,$$

$$dr/ds = -\cos\gamma.$$

These equations were solved by a fourth-order Runge–Kutta method, and the algorithms where checked by reproducing the analytic results for: (1) linear and exponential profiles in planar geometry[22] and (2) a $1/r^2$ profile in spherical geometry. Any rays that reached 0.1% of critical density were then reflected with γ replaced by $\pi - \gamma$.

Energy was deposited along the ray trajectory by inverse bremsstrahlung, using the absorption coefficient[23]

$$\kappa = 3.1\times10^{-7} Z n_e^2 \ln\Lambda/[\omega^2 T^{3/2}(1 - n_e/n_c)^{1/2}]\ \text{cm}^{-1},$$

where T is the electron temperature (eV), Z is the average ionic charge, and ω is the laser angular frequency. The energy deposited was distributed over the region between rays to obtain the energy density ϵ.

Typically the uniformity calculations were performed by dividing one laser beam into 200 rays. Some cases were rerun with 1000 rays to check the accuracy, and they showed no significant difference.

[1] J. H. Nuckolls, L. Wood, A. Thiessen, and G. Zimmerman, Nature 239, 139 (1972).

[2] W. C. Mead and J. D. Lindle, "Symmetry and Illumination Uniformity Requirements for High Density Laser-Driven Implosion," UCRL-78459 (1976) (unpublished).

[3] J. H. Nuckolls, Phys. Today 35, 24 (1982).

[4]Lawrence Livermore Laboratory Laser Program Annual Report: (1974) UCRL-50021-74, p. 219; (1975) UCRL-50021:75, p. 98.
[5]J. E. Howard, Appl. Opt. **16**, 2764 (1977).
[6]K. Lee, R. L. McCrory, and R. Hopkins, Laboratory for Laser Energetics Report No. 88 (1981) (unpublished), and Laboratory for Laser Energetics Quarterly Report (LLE Rev.) **4**, 6 (1980).
[7]A. R. Bell and D. J. Nicholas, Rutherford Laboratory Annual Report, RL-82-039 (1982), p. 1.16.
[8]M. H. Emery, J. H. Orens, J. H. Gardner, and J. P. Boris, Phys. Rev. Lett. **25**, 253 (1982).
[9]R. G. Evans, A. J. Bennett and G. J. Pert, J. Phys. D: **15**, 1673 (1982).
[10]S. E. Bodner, J. Fusion Energy **1**, 221 (1981).
[11]A perturbation expansion of the expression for saturated (flux-limited) heat flow shows that the asymptotic attenuation of a temperature nonuniformity varies exponentially as the *square* of the wavenumber k, i.e., $\exp(-Lk^2\Delta R)$, where L is the unperturbed temperature scale-length $T_0/|dT_0/dr|^{-1}$; S. Skupsky, Laboratory for Laser Energetics Report No. 131 (1982) (unpublished), and Laboratory for Laser Energetics Quarterly Report (LLE Rev.) **10**, 18 (1982).
[12]J. H. Gardner and S. E. Bodner, Phys. Rev. Lett. **47**, 1137 (1981).
[13]R. L. McCrory and R. L. Morse, Phys. Rev. Lett. **38**, 544 (1977).
[14]R. G. Evans, A. J. Bennett, and G. J. Pert, Phys. Rev. Lett. **49**, 1639 (1982). For additional discussion of the Rayleigh–Taylor instability see: C. P. Verdon, R. L. McCrory, R. L. Morse, G. R. Baker, D. I. Meiron, and S. A. Orszag, Phys. Fluids **25**, 1653 (1982).
[15]J. Bunkenberg, J. Boles, D. Brown, J. Eastman, J. Hoose, R. Hopkins, L. Iwan, S. Jacobs, J. Kelly, S. Kumpan, S. Letzring, D. Lonobile, L. Lund, G. Mourou, S. Refermat, W. Seka, J. Soures, and K. Walsh, IEEE J. Quantum Electron. **QE-17**, 1620 (1981), and Laboratory for Laser Energetics Quarterly Report (LLE Rev.) **2**, 1 (1980).
[16]M. J. Monsler, J. Hovingh, D. L. Cook, T. G. Frank, and G. A. Moses, Nucl. Technol./Fusion **1**, 302 (1981).
[17]R. Kidder, Nucl. Fusion **16**, 1 (1976).
[18]W. Seka, R. S. Craxton, J. Delettrez, L. Goldman, R. Keck, R. L. McCrory, D. Shvarts, J. M. Soures, and R. Boni, Opt. Commun. **40**, 437 (1982).
[19]C. E. Max, C. F. McKee, and W. C. Mead, Phys. Fluids **23**, 1620 (1980).
[20]J. Soures (private communication); J. Hoose, L. Iwan, J. Kelly, K. Lee, L. Lund, R. L. McCrory, M. C. Richardson, S. Skupsky, J. M. Soures, D. M. Villeneuve, and C. Verdon, Bull. Am. Phys. Soc. **27**, 940 (1982).
[21]M. Born and E. Wolf, *Principal of Optics* (Pergamon, New York, 1975), p. 123.
[22]J. W. Shearer, Phys. Fluids **14**, 183 (1971).
[23]T. W. Johnston and J. M. Dawson, Phys. Fluids **16**, 722 (1973).

APPENDIX II

SIRIUS Beam Geometry Coordinates

(Angles are in degrees)

Beam Number	20 Beam		32 Beam		60 Beam		96 Beam	
	θ	Φ	θ	Φ	θ	Φ	θ	Φ
1	0.00	0.00	0.00	0.00	0.00	0.00	0.00	0.00
2	41.82	0.00	37.38	0.00	27.40	-88.47	21.13	-72.40
3	41.82	120.00	37.38	72.00	124.26	99.31	140.50	82.34
4	41.82	240.00	37.38	144.00	146.27	34.22	178.06	79.71
5	70.53	37.76	37.38	216.00	53.49	-84.87	25.47	-127.56
6	70.53	82.24	37.38	288.00	99.69	166.36	120.05	-157.08
7	70.53	157.76	63.44	36.00	88.27	-149.82	62.55	-144.04
8	70.53	202.24	63.44	108.00	150.98	-73.77	120.23	-86.16
9	70.53	277.76	63.44	180.00	44.22	12.85	60.77	4.87
10	70.53	322.24	63.44	252.00	55.53	-117.92	48.76	-122.28
11	109.47	22.24	63.44	324.00	74.9	155.59	80.36	177.30
12	138.18	60.00	79.19	0.00	27.17	-24.38	38.80	-48.94
13	109.47	97.76	79.19	72.00	151.09	94.56	158.42	165.91
14	109.47	142.24	79.19	144.00	28.44	48.90	43.06	49.11
15	138.18	180.00	79.19	216.00	83.37	-124.20	70.54	-119.67
16	109.47	217.76	79.19	288.00	102.44	-52.79	70.38	-57.99
17	109.47	262.24	180.00	180.00	86.64	34.97	120.54	11.07
18	138.18	300.00	142.62	180.00	83.96	-11.78	102.80	-40.31
19	109.47	337.76	142.62	252.00	128.74	131.57	137.52	162.20
20	180.00	0.00	142.62	324.00	149.45	-17.54	157.56	-1.20
21			142.62	36.00	57.13	-18.12	69.57	-17.57
22			142.62	108.00	107.17	-24.05	124.48	-42.20
23			116.57	216.00	133.32	-114.05	121.83	-112.06
24			116.57	288.00	128.88	65.39	155.02	111.68
25			116.57	0.00	33.60	-142.05	41.93	-152.45
26			116.57	72.00	77.88	64.96	94.10	40.31
27			116.57	144.00	78.68	-38.59	80.89	-38.39

Beam Number	20 Beam θ	20 Beam Φ	32 Beam θ	32 Beam Φ	60 Beam θ	60 Beam Φ	96 Beam θ	96 Beam Φ
28			100.81	180.00	102.72	139.84	118.34	150.52
29			100.81	252.00	103.56	54.89	131.31	54.32
30			100.81	324.00	100.06	112.01	106.51	101.35
31			100.81	36.00	77.48	127.24	98.70	141.75
32			100.81	108.00	49.98	-50.55	46.08	-16.04
33					52.63	179.29	61.19	163.49
34					158.09	-136.96	141.89	-100.89
35					59.12	42.77	72.07	46.68
36					106.21	-106.98	103.50	-101.21
37					112.16	-135.76	83.15	-137.81
38					124.35	-79.01	97.42	-80.40
39					100.06	9.79	134.68	-8.67
40					77.86	94.11	83.79	99.15
41					118.74	30.85	139.24	25.20
42					102.00	82.29	98.19	80.60
43					128.42	-43.83	112.97	-63.01
44					98.35	-79.93	75.76	-79.41
45					78.10	-97.51	82.39	-100.45
46					70.98	12.67	78.23	23.45
47					55.90	109.43	68.17	114.71
48					174.85	32.08	159.92	-72.14
49					51.74	75.49	38.96	81.82
50					61.30	-149.23	61.07	-169.92
51					79.08	-175.37	80.24	-160.27
52					125.42	-1.60	145.00	-37.41
53					75.19	-65.98	60.69	-97.46
54					26.85	166.07	37.39	144.24
55					108.82	-167.25	111.81	-132.83
56					152.91	155.59	157.32	-134.09
57					29.22	106.43	21.64	48.18
58					134.38	-157.45	134.68	-134.39

Beam Number	20 Beam		32 Beam		60 Beam		96 Beam	
	θ	Φ	θ	Φ	θ	Φ	θ	Φ
59					126.54	166.27	140.56	-165.35
60					50.50	142.64	80.79	155.34
61							76.52	78.79
62							91.46	-59.49
63							155.68	54.02
64							136.51	131.50
65							59.46	65.63
66							21.20	177.51
67							136.15	-68.37
68							119.26	79.72
69							127.72	105.43
70							58.09	138.83
71							119.67	177.55
72							100.07	-172.43
73							93.06	118.78
74							59.59	92.48
75							109.20	58.34
76							99.25	19.29
77							103.39	-2.04
78							78.41	134.08
79							57.83	29.73
80							87.70	60.99
81							94.30	-120.26
82							100.50	165.07
83							22.36	111.03
84							115.40	-20.12
85							53.19	-71.36
86							116.23	35.33
87							42.65	175.94
88							99.73	-150.58
89							91.89	-20.08
90							58.45	-38.71
91							39.34	-93.61
92							23.40	-13.87

Beam Number	20 Beam θ	20 Beam Φ	32 Beam θ	32 Beam Φ	60 Beam θ	60 Beam Φ	96 Beam θ	96 Beam Φ
93							45.70	113.94
94							38.87	15.21
95							114.23	125.45
96							82.27	1.55

APPENDIX III

SIRIUS Final Optic Merit Function

The transformation from a uniform intensity distribution to a quadratic intensity distribution at the target may be calculated in the following manner.

The following intensity distributions are assumed:

$$(\text{entrance})\ i(R) = I_o \tag{1}$$

$$(\text{target})\ i(r) = I\left(1 - \frac{r^2}{r_o^2}\right) \tag{2}$$

where:

R = radial position in the entrance aperture

R_o = entrance aperture radius

r = radial position in a plane tangent to the target

r_o = target radius

These intensity distributions lead to the following energy relationships:

$$E_R = \int_o^R 2\pi I_o R dR = \pi I_o R^2 \tag{3}$$

$$E_r = \int_o^r 2\pi I\left(1 - \frac{r^2}{r_o^2}\right) r\,dr = 2\pi I\left[\frac{r^2}{2} - \frac{r^4}{4r_o^2}\right] \qquad (4)$$

If the total energy at the entrance and target planes are calculated and set equal, the maximum intensity in the target plane may be found.

$$\text{Max } E_R = \pi I_o R_o^2$$

$$\text{Max } E_r = \pi I\left[r_o^2 - \frac{r_o^2}{2}\right] = \frac{\pi I r_o^2}{2}$$

$$\text{then} \qquad I_o R_o^2 = \frac{I r_o^2}{2}$$

$$\text{So} \qquad I = 2I_o \cdot \left(\frac{R_o}{r_o}\right)^2 . \qquad (5)$$

Then for a general value of R

$$I_o R^2 = 2I_o \left(\frac{R_o}{r_o}\right)^2 \cdot \left[r^2 - \frac{r^4}{2r_o^2}\right]$$

$$R^2 = 2\left(\frac{R_o}{r_o}\right)^2 \left[r^2 - \frac{r^4}{2r_o^2}\right]$$

$$\frac{R^2}{2}\left(\frac{r_o}{R_o}\right)^2 = \left[r^2 - \frac{r^4}{2r_o^2}\right]$$

Then

$$\frac{r^4}{2r_o^2} - r^2 + \frac{R^2}{2}\left(\frac{r_o}{R_o}\right)^2 = \frac{r^4}{2r_o^2} - r^2 + \left(\frac{R}{R_o}\right)^2 \cdot \frac{r_o^2}{2}$$

Then

$$r^2 = \frac{1 \pm \sqrt{1 - \frac{4}{2r_o^2} \cdot \frac{r_o^2}{2} \left(\frac{R}{R_o}\right)^2}}{\frac{2 \cdot 1}{2r_o^2}}$$

Finally

$$\left(\frac{r}{r_o}\right)^2 = 1 \pm \sqrt{1 - \left(\frac{R}{R_o}\right)^2} \qquad (6)$$

let:

$$\rho_R = \left(\frac{R}{R_o}\right)$$

$$\rho_r = \left(\frac{r}{r_o}\right)$$

$$\rho_r^2 = 1 \pm \sqrt{1 - \rho_R^2} \qquad (7)$$

Example:

Relative radius in Entrance Aperture	Relative radius in Target Plane
ρ_R	ρ_r
0.2	0.1421
0.4	0.2889
0.6	0.4472
0.8	0.6325
1.0	1.0.

The figure of merit used in the optimization is defined as:

$$\text{Figure of merit} = \sum_{A=1}^{20} (\text{ray departure})^2 \qquad (8)$$

where the ray departure is defined as:

$$\text{ray departure} = \frac{\text{calculated ray position - ray position from equation 7}}{\text{ray position tolerance}}$$

The ray position tolerances were specified to evenly weigh all rays in the figure of merit.